INFORMATION TO USERS

This manuscript has been reproduced from the microfilm master. UMI films the text directly from the original or copy submitted. Thus, some thesis and dissertation copies are in typewriter face, while others may be from any type of computer printer.

The quality of this reproduction is dependent upon the quality of the copy submitted. Broken or indistinct print, colored or poor quality illustrations and photographs, print bleedthrough, substandard margins, and improper alignment can adversely affect reproduction.

In the unlikely event that the author did not send UMI a complete manuscript and there are missing pages, these will be noted. Also, if unauthorized copyright material had to be removed, a note will indicate the deletion.

Oversize materials (e.g., maps, drawings, charts) are reproduced by sectioning the original, beginning at the upper left-hand corner and continuing from left to right in equal sections with small overlaps.

Photographs included in the original manuscript have been reproduced xerographically in this copy. Higher quality 6" x 9" black and white photographic prints are available for any photographs or illustrations appearing in this copy for an additional charge. Contact UMI directly to order.

Bell & Howell Information and Learning
300 North Zeeb Road, Ann Arbor, MI 48106-1346 USA
800-521-0600

UMI®

HARVARD UNIVERSITY
Graduate School of Arts and Sciences

THESIS ACCEPTANCE CERTIFICATE

The undersigned, appointed by the

Division

Department of Physics

Committee

have examined a thesis entitled "Mesoscopic Electron Transport in Semiconductor Nanostructures"

presented by David Scott Duncan

candidate for the degree of Doctor of Philosophy and hereby certify that it is worthy of acceptance.

Signature ....

Typed name Robert M. Westervelt, Chair

Signature M. Tinkham

Typed name Michael Tinkham

Signature ....

Typed name Efthimios Kaxiras

Date May 22, 2000

Mesoscopic Electron Transport in Semiconductor Nanostructures

A thesis presented

by

David Scott Duncan

to

The Department of Physics

in partial fulfillment of the requirements

for the degree of

Doctor of Philosophy

in the subject of

Physics

Harvard University

Cambridge, Massachusetts

May, 2000

UMI Number: 9972303

Bell & Howell Information and Learning Company
300 North Zeeb Road
P.O. Box 1346
Ann Arbor, MI 48106-1346

Mesoscopic Electron Transport in Semiconductor Nanostructures

Robert M. Westervelt David Scott Duncan

Abstract

This thesis presents experiments investigating mesoscopic electron transport in semiconductor nanostructures. The devices studied were fabricated in GaAs/AlGaAs heterostructures containing two-dimensional electron gases. The first experiment studies the breakdown of charge quantization in a quantum dot functioning as a single-electron box. The charge in the box is measured directly using a second. capacitively coupled quantum dot functioning as a single-electron transistor electrometer. The electrometer is demonstrated to be superior to conductance measurements for studying charge quantization in quantum dots, and is used to directly measure the breakdown of charge quantization in the box as the box-to-lead tunnel-coupling is increased. Charge quantization is shown to be destroyed at a tunnel-coupling of $2e^2/h$ in agreement with theory.

Two other experiments on quantum dots are also presented. The first uses Coulomb blockade spectroscopy to study manifestations of spin in the addition spectrum of a small quantum dot. The motion of Coulomb blockade peaks is studied in a parallel magnetic field. The peak motion at low field is interpreted as due to the electron spin and is consistent with that expected from Zeeman coupling, but at higher field orbital effects are found to be important. The final quantum dot experiment studies the magnetic field behavior of two quantum dots in an artifical molecule. Mesoscopic fluctuations are observed in the double dot ground state energy and other properties which can be explained by the interference of electron wavefunctions on the dots.

Finally, experiments on an electron resonator are presented. The resonator is an open structure in which the effects of quantum interference of electrons are dramatically apparent. Conductance peaks in transport measurements are observed which are explained by the constructive interference of electron waves with a period of a Fermi wavelength. The peak positions are found to shift in a perpendicular magnetic field. These shifts are explained by the combined effects of electron trajectory bending and the Aharanov-Bohm phase shift.

Table of Contents

Acknowledgements

The process of obtaining a Ph.D. has been a rewarding one, and many people deserve thanks for helping to make this experience both possible and enjoyable.

I would first like to thank my thesis advisor, Bob Westervelt. Bob has created a terrific environment for studying science on the second floor of Gordon McKay, full of interesting research projects and friendly, fun people. I have always appreciated Bob's unwavering faith in his graduate students and his genuine concern for their well-being. I am grateful for the support and encouragement he gave me as I pursued my research projects and made career decisions. I would also like to thank the other two members of my committee, Professor Michael Tinkham and Professor Tim Kaxiras, for their support and for their interest in my work.

I have been very fortunate to work with a great group of friends and colleagues in the Westervelt lab. In my first year, I had the pleasure of collaborating with Carol Livermore, whose ability to communicate complicated physics issues in simple terms has remained an example to me. Mark Topinka has taught me much about the art of experimentation, and I have enjoyed our many late night physics discussions. Marija Drndic has been with me from the beginning, and I have always appreciated her sense of humor and ongoing discourse on Yugoslav politics. Lester Chen has been a wonderful co-conspirator in various plots over the years, and an indispensable logistics pointman. This past year I have had the pleasure of working with David Goldhaber-Gordon, and I have learned much from our many discussions about physics and finance. I have enjoyed getting to know the more recent additions to the Westervelt group, including Chungsok Lee, Ian Chan, and Brian Leroy, and I wish them the best of luck in the future.

Other residents of Gordon McKay have contributed much to my graduate school experience. Over the years I have enjoyed and benefited from discussions and collaborations with members of the Tinkham group, including Jack Hergenrother, Dolores Bozovic, Sarah Pohlen, Marc Bockrath, Jeanie Lau, and Drago Davidovic. Steve Shepard does a terrific job of running the clean room, and has been a perenially cheerful presence on the floor.

Two professors at the University of Idaho were particularly influential in my development and in my decision to pursue graduate study. Mike Browne in the physics department was a great source of inspiration with his infectious enthusiasm for teaching and discussing physics. Roy Goetschel in the math department is equally gifted in his ability to generate enthusiasm in his students with his genuine love for the subject of calculus.

Of course no one deserves more heartfelt thanks than my friends and family, who have supported me from both near and far during these many years. My fondest memories of Harvard are times spent with the many friends I have made or re-encountered during this time. My former Beacon Street roommates Marc de Croisset and Mike Dieffenbach deserve much credit for making my first few years fun. I was fortunate to find a kindred spirit in Marc during my first year at Harvard, and Mike's appearance in Boston was a great stroke of luck. Greg Smith has been a great friend and salsa instructor, and I look forward to our eventual tandem debut at Ryles. I am happy that my last year at Harvard overlapped Bob Rosin's time at the business school, as we have had the opportunity to renew our ambulatory Parisian conversations. Elisa Dugundji has been a great friend, providing wisdom, perspective, and many fond memories. My cohorts from my physics class, Chip Coldwell and Luca Marinelli, have shared many laughs over the years.

From the other coast, I have received consistent support and positive, energizing, transcontinental vibes from my friends Ben Schwartzman, his wife Nimi, and Randy Milanowski. Ben and Nimi have always been willing to drop their real-world responsibilities to chat about the vicissitudes of graduate school, and I look forward to more frequent visits now that the fridge no longer dominates my agenda. Randy and I have been in constant communication over the years, and as always our friendship has been a great source of enjoyment and sustenance.

Valérie has walked this path with me for the past few years, as we wandered through le Plat Pays, le Port d'Amsterdam, and other locales, and as we both pursued graduate studies in our respective countries. Her presence, both physical and virtual, has been a source of inspiration, comfort, and happiness.

My brother, Brian, has given me valuable encouragement over the years. None of this would ever have been possible without the lifelong love, support, and encouragement of my parents. Everything I have accomplished in my life is thanks to them.

Chapter 1

Introduction

1.1 Motivation

In the late 1980s, the convergence of advanced microfabrication and cryogenic measurement techniques opened the way to the in-depth study of a new field of solid state physics hitherto only accessible on the pages of textbooks: reduced dimensionality systems. The canonical quantum mechanical behaviour of electrons confined in one or more dimensions has been dramatically illustrated in myriad experiments, and many new, unanticipated phenomena have been observed as well. These experiments have provided new insight into the fundamental physics of electron transport in solids, especially in the mesoscopic length scale regime where the wave-particle duality of electrons is strikingly manifested. This research has in turn had repercussions for solid state applications, including both a clearer understanding of the limitations of current microelectronic technology and proposals for novel electronics based on mesoscopic phenomena. In this thesis, I describe experimental work which illustrates a wide range of effects in mesoscopic electron transport in reduced dimensionality systems, providing new insight into several problems and suggesting directions for further research.

The study of electron confinement in two dimensions was made widely possible with the advent of molecular beam epitaxy and heterostructure superlattices [for a review see Gossard, 1982]. Using MBE, heterostructure materials can be grown one atomic layer at a time, and thus the band structure of solids can be engineered with unprecedented levels of precision. By carefully designing the heterostructure, a thin, highly mobile layer of electrons can be confined to the interface of two materials with differing bandgaps (in this thesis, these materials are GaAs and AlGaAs). At sufficiently low temperatures, these electrons form an effectively metallic gas, the wavefunctions of which are confined in one dimension to the lowest energy mode, resulting in the formation of a two-dimensional electron gas (2DEG). Many interesting phenomena were observed in the 2DEG system, including the quantum Hall effect [von Klitzing *et al.*, 1980] and the fractional quantum Hall effect [Tsui *et al.*, 1982], for which the 1985 and 1998 Nobel Prizes in Physics, respectively, were awarded.

Using the 2DEG as a starting point, electrons can be further confined using modern nanolithography techniques. In particular, electron beam lithography can be used to pattern sub-micron features on the surface of a 2DEG heterostructure. Such patterning can be followed by chemical etching or "electrostatic etching" of select portions of the 2DEG material to form one-dimensional channels in the 2DEG layer. In the mesoscopic regime, for very short channel lengths, these channels are called quantum point contacts; electron wavefunctions are quantized in two dimensions as they travel through the contact. The now classic experiment performed on such a system was the measurement of the point contact conductance, which was demonstrated to be quantized as a simple consequence of one-dimensional transport [van Wees *et al.*, 1988; Wharam *et al.*, 1988]. This is similar to the quantization of conductance in the quantum Hall effect, where transport also occurs via one-dimensional edge channels at the boundaries of the sample [Sohn *et al.*, 1996].

The natural extension of this work was the zero-dimensional confinement of electrons in the 2DEG. This can again be achieved via nanolithography and the etching away of 2DEG regions in order to isolate small pools of electrons. Such systems are called quantum dots, and are the realization of the textbook particle-in-a-box system. Quantum dots are often referred to as "artifical atoms" because of their resemblance to real atoms, in which electrons are also confined in three dimensions [Kastner, 1993]. In a typical setup, the quantum dot is coupled to leads via tunnel junctions, enabling the spectroscopic study of the quantum dot energetics via transport measurements. Experiments on quantum dots comprise an extremely rich and fascinating field [Grabert and

Devoret, 1992; Kastner, 1992; Sohn *et al.*, 1996], and they are one of the principal subjects of this thesis. Quantum dots provide a remarkably versatile system for exploring an array of phenomena that illustrate fundamental features of quantum mechanics. The wave-particle duality that lies at the heart of quantum theory is strikingly manifested in these systems. This thesis describes experiments in which both sides of this duality are explored.

In addition to shedding new light on the fundamental nature of electron transport in solids, the study of reduced dimensionality systems has proven relevant to technology, both in its current form and in proposed, novel paradigms for future electronics. Historically, the primary driver behind enhanced computer performance has been exponential advances in device miniaturization. This trend can not continue indefinitely, and is already running into fundamental obstacles. As device dimensions shrink, the fundamentally discrete nature of the electron charge and quantum interference of electron waves are increasingly manifested, effects which can lead to unacceptable degradation of device properties. The study of such mesoscopic phenomena is therefore important for future generations of microelectronic circuits. In addition, some researchers have attempted to exploit such phenomena by making them the basis for new computing and electronics paradigms. For example, quantum coherence forms the basis for proposals for quantum computers [Loss and DiVincenzo, 1998; Bukard *et al.*, 1999; Imamoglu *et al.*, 1999; DiVincenzo and Loss, 1999], and the discrete nature of the electron charge forms the basis for the field of single-electron devices or single electronics [Likharev and Averin, 1992].

1.2 Overview of the Thesis

In this thesis, experiments are presented which elucidate various aspects of mesoscopic electron transport, primarily in quantum dot systems. Chapter II provides an overview of the theory of 2DEGs, quantum point contacts, and quantum dots to lay the groundwork for the chapters that follow. A description of the properties of 2DEGs and quantum point contacts is first given, as these are the building blocks for quantum dot structures. Quantum dots and Coulomb blockade are then discussed, along with simple models upon which to build an understanding of quantum dot physics. Representative data illustrating key features of these models are also presented.

In Chapter III, the experimental methods used for this work are described. The techniques for fabricating quantum dot devices are discussed in detail, both to provide a basis for understanding the experiments that follow and to serve as a reference for other students interested in fabricating similar structures. The fabrication section focuses on electron-beam lithography and metallization. Cryogenic and electronic measurement techniques used in the experiments of this thesis are also described.

Chapter IV presents measurements which study the breakdown of charge quantization in a quantum dot functioning as a single-electron box. Charge quantization in a quantum dot is one of its signature properties, and thus it is important to understand the conditions under which it takes place. The measurement is done with a second, adjacent quantum dot functioning as a single-electron transistor (SET) electrometer. This SET electrometer is demonstrated to have sub-single electron sensitivity and to be superior to transport measurements for studying charge quantization in quantum dots. The work described in this chapter is the first to directly study the breakdown of charge quantization in a quantum dot over the full range of dot-to-lead conductance values, and is shown to agree with recent theory.

Chapter V presents experiments which investigate the role of the electron spin in the energy spectra of a very small quantum dot. Previously, the electron spin has generally only been indirectly manifested in this type of quantum dot. Transport measurements are made on the quantum dot in a parallel magnetic field with the aim of observing a Zeeman contribution to the dot ground state energy, a consequence of the electron spin. Results are presented which show an evolution of the dot ground state energy consistent with such a Zeeman contribution. Possible orbital effects of the magnetic field are discussed as well.

Chapter VI presents measurements on a double quantum dot system which study the interactions between two quantum dots. Understanding such interactions is important for proposed applications which involve multiple dot systems. In particular, mesoscopic fluctuations in the interactions between quantum dots are studied. These fluctuations are a consequence of quantum interference of phase coherent electron waves, and are ubiquitous in mesoscopic systems. The fluctuations are shown to be manifested in the magnetic field dependence of the interdot interactions and ground state energy. The findings are discussed in the context of proposed applications for multiple quantum dot structures.

Chapter VII also describes experiments which study the effects of electron interference, but in a rather different system: an electron resonator. This system consists of a single quantum point contact connected to an open cavity. Electrons enter the cavity through the point contact and set up interference patterns which can be probed by transport measurements. Conductance resonances in the transport signal are observed, and their evolution with magnetic field and the number of transmitting modes in the quantum point contact is studied. The magnetic field data are explained by a model incorporating the effects of trajectory bending and the Aharonov-Bohm phase shift. The latter is shown to be essential to explain the data, and thus these experiments constitute an unusual observation of the Aharonov-Bohm phase shift in an open system.

Finally, chapter VIII concludes the thesis with a synopsis of the key results. Several directions for further research suggested by these results are also discussed.

Chapter 2

Theoretical Background

2.1 Introduction

In the last chapter, I introduced the idea of reduced dimensionality systems, including the two-dimensional electron gas (2DEG), the one-dimensional quantum point contact, and zero-dimensional quantum dots. In this chapter, I describe the physical properties and modeling of these systems in order to lay the groundwork for the experiments presented in subsequent chapters. Data illustrating fundamental phenomena in these systems is also presented. The basic properties of the 2DEG are first described, and its use in the fabrication of lower-dimensional structures is explained. The physics of quantum point contacts is then discussed, primarily in the context of their use as building blocks for quantum dots. Finally, the basic phenomena observed in quantum dots are described, and models for understanding them outlined.

2.2 Two-dimensional electron gas

The starting point for all of the devices described in this thesis is the two-dimensional electron gas, or 2DEG. The 2DEG is typically formed in a semiconductor heterostructure, the band structure of which is engineered to confine a thin layer of highly mobile electrons in a quantum well a few hundred angstroms beneath the surface. At sufficiently low temperatures, the electrons remain in the lowest transverse mode of the quantum well but move freely in the other two dimensions, resulting in an effectively metallic, two-dimensional sheet of electrons. The precise structure of the GaAs/AlGaAs heterostructures used in our experiments is discussed in Chapter 3 of this thesis. Here I will simply detail some important properties of a 2DEG which will be used in subsequent chapters.

A key parameter of a 2DEG which determines many other important energy and length scales is the sheet density, n_s. For our heterostructures, n_s is typically on the order of 3-4 x $10^{11}/\mathrm{cm}^2$, a very low density relative to metals. From n_s and the two-dimensional density of states the Fermi energy can be calculated. The density of states for free electrons in two dimensions is constant and given by:

$$\rho(E) = \frac{dn}{dE} = \frac{m^*}{\pi\hbar^2}$$

where $m^* = 0.067m_e$ is the effective mass of an electron in GaAs. The Fermi energy is then given by:

$$Ef = \frac{n_s \pi\hbar^2}{m^*}$$

For a typical sheet density of 3.5 x $10^{11}/\mathrm{cm}^2$, E_f = 12.5 meV. This corresponds to a temperature of 145 K, which, along with the 2DEG subband spacing, determines the temperature necessary to maintain electron confinement in the lowest subband. This criterion is clearly met in our low temperature measurements.

Also derivable from the sheet density is the average inter-electron spacing, usually defined in units of the Bohr radius and given the symble r_s. This quantity, known as the free electron gas parameter, is equivalent to the ratio between the interaction energy and kinetic energy of electrons in the system and thus determines the relative importance of electron-electron interactions in the 2DEG. This ratio is the Coulomb interaction between two particles at an average distance r over the energy of a free electron:

$$\frac{E_{\mathrm{int}}}{E_k} = \frac{e^2 mr^2}{r\hbar^2} = \frac{r}{a} \equiv r_s$$

where a is the Bohr radius in GaAs. For $r_s \gg 1$, electron-electron interactions dominate and the system can be described as a Wigner crystal. For $r_s \ll 1$, interactions can be treated perturbatively. For the intermediate regime, $r_s \sim 1$, theoretical treatments are much more challenging. Unfortunately, this is precisely the regime of our semiconductor quantum dots, where $r_s \sim 1$. As we will see in subsequent chapters, this fact makes understanding the energy spectra of quantum dots in terms of simple non-interacting particle models difficult. This difficulty has been the inspiration behind a recent experiment which aims at understanding electron-electron interactions in this regime (Zhitenev *et al.*, 1999).

The sheet density can also be used to calculate the typical spacing between energy levels in the 2DEG quantum well. An analytical estimate of the eigenstates of a triangular heterostructure well similar to that described in chapter 3 was obtained by Harris [1989] using Airy function solutions to the Schrodinger equation. This expression is:

$$E_i \cong 26\left[(i+.75)n_s \times 10^{-11} cm^2\right]^{2/3} meV$$

Inserting in this expression a sheet density of 3.5 x $10^{11}/\mathrm{cm}^2$, we find $E_o = 49$ meV, $E_1 =$ 87 meV, and $E_1 - E_o = 38$ meV. Comparing this difference with the Fermi energy, we conclude that electrons are confined to the lowest subband in the quantum well at temperatures used in our experiments.

The Fermi wavelength λ_f can also be calculated from n_s. For our typical sheet densities, $\lambda_f \sim 40$ nm. The Fermi wavelength of electrons in the 2DEG defines the meaning of one-dimensional and zero-dimensional systems. For example, quantum point contacts typically have widths on the order of a Fermi wavelength, meaning transport through them is truly one-dimensional. Similarly, the lateral dimensions of quantum dots described in this thesis are typically on the order of a few hundred nanometers, and thus they are good approximations to true zero-dimensional systems.

2.3 Quantum point contacts

The 2DEG heterostructure is used as the starting point for fabricating lower-dimensional devices. The technique for doing so used in our lab is the split-gate technique [Thornton *et al.*, 1986; Zheng *et al.*, 1986], illustrated in Fig. 2.1. The first step is to fabricate ohmic contacts on the surface of the heterostructure which contact the 2DEG layer below, as shown in Fig. 2.1 (a). This enables transport measurements to be made on the 2DEG. The second step is to deposit metal gates on the surface of the chip in the shape of the desired device, typically a quantum point contact or quantum dot, using electron-beam lithography. Multiple, separate gates are usually deposited to define a device; thus the term "split-gate." Negative voltages applied to the gates electrostatically "etch" out the contours of the device in the 2DEG layer. These electrostatic boundaries can define one-dimensional channels (quantum point contacts) or zero-dimensional "puddles" of electrons (quantum dots). Both of these devices are illustrated in Fig. 2.1 (b) which shows a quantum dot defined in this manner. The dot is coupled to the 2DEG leads by quantum point contacts, the widths of which can be electrostatically adjusted to determine the strength of the dot-to-lead coupling. Transport measurements can be carried out by passing current through the reduced-dimension structures. The steps for fabricating these structures are described in Chapter 3.

The quantum point contact is the classic one-dimensional system. It is simply a narrow constriction with width on the order of the electron Fermi wavelength through which electrons can flow. The constriction is defined by two closely spaced metal gates, and its width can be adjusted by varying the gate voltages. Electrons can be induced to traverse the point contact by applying a bias across the channel. In our measurements, this bias is typically quite small, on the order of 10 μeV, so all transport occurs at the Fermi level. Because of this, the effects of the individual transverse modes in the quantum point contact mediating transport can be observed in these conductance measure-

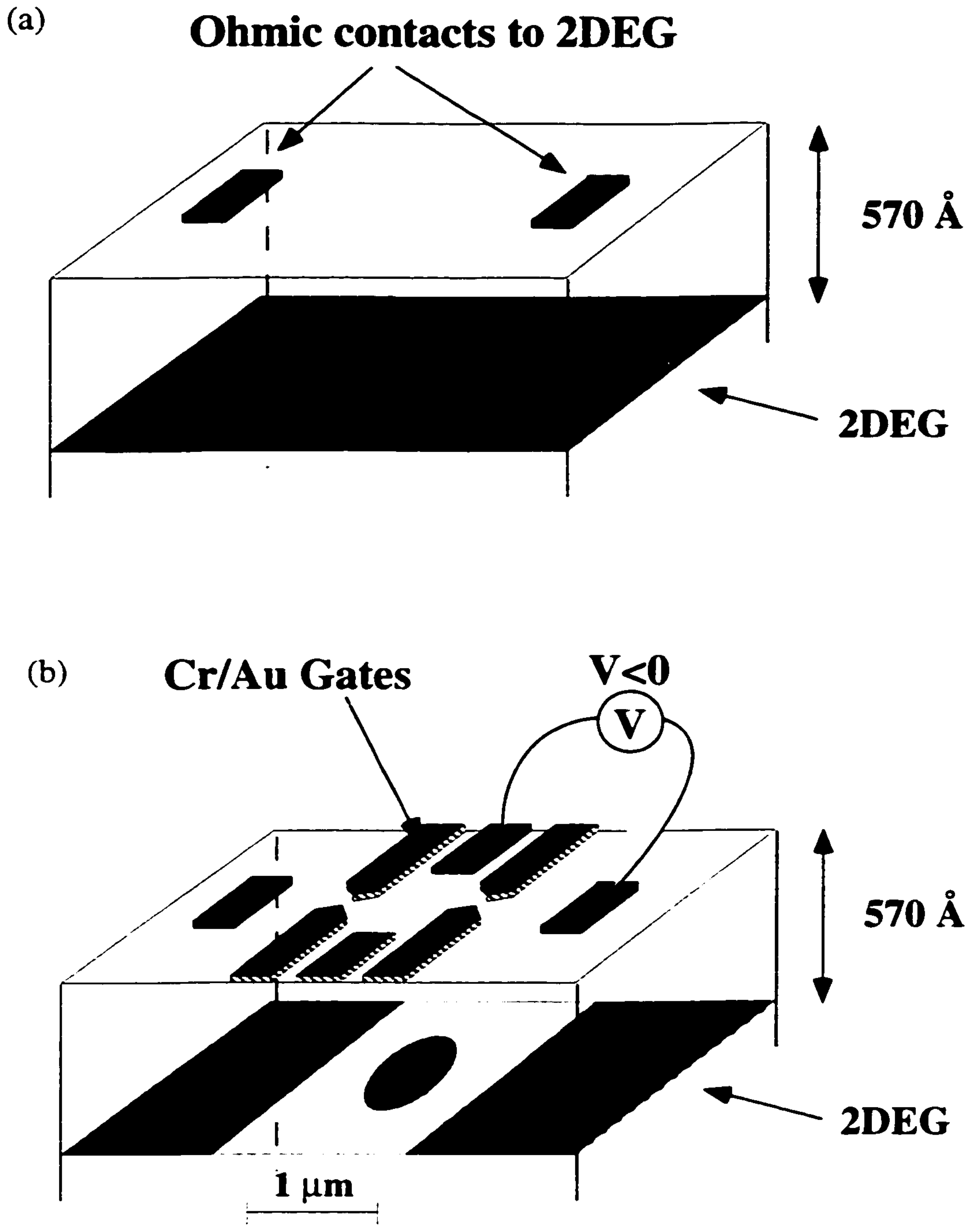

Figure 2.1 Illustration of split-gate fabrication technique. (a) Ohmic contacts are deposited on the surface of the GaAs/AlGaAs heterostructure, enabling current to be passed through the 2DEG layer. (b) Cr-Au gates are deposited on the surface of the heterostructure. When negative voltages are applied, the contours of the quantum dot are electrostatically defined in the 2DEG layer.

ments.

Fig. 2.2 shows a characteristic trace from such a measurement. This is a plot of the differential conductance through the point contact as a function of the voltage V_{qpc} on the two metal gates defining the point contact. As the bias is made more negative, the width of the point contact narrows. Thus, we would expect the conductance to decrease and eventually go to zero when the point contact channel is completely pinched off. This is indeed the case. However, the remarkable feature of this measurement is the manner in which it goes to zero. It does not do so smoothly and linearly, as we would expect if electrons were point particles behaving according to the simple Drude model of transport. Rather, the conductance decreases in a series of steps, each with a height of $G_Q \equiv 2e^2/h$, a quantity known as the conductance quantum. This behaviour is due to the "squeezing out" of one-dimensional subbands available for transport as the channel is narrowed. Narrowing the channel raises the energies of each of the one-dimensional subbands, which become inaccessible as each is raised through the Fermi level. Remarkably, each of these subbands contributes equally to the conductance, resulting in the evenly spaced steps observed in experiments [Van Wees *et al.*, 1988; Wharam *et al.*, 1988].

The theory developed to explain this behaviour is known as the Landauer-Buttiker formalism [Landauer, 1957; Buttiker, 1986; Buttiker, 1988]. This theory was developed to define the concept of conductance in the ballistic transport regime, in which device dimensions are much less than the mean free path for impurity scattering. If such scattering does not occur as an electron traverses a ballistic device, why is the conductance not infinite? The answer, of course, lies in the wave nature of electrons. Transport in the ballistic regime can be understood as the transmission of electron waves through a waveguide. In the case of a quantum point contact, this waveguide is one-dimensional. The fundamental expression derived by Landauer and Buttiker for the conductance G through a quantum point contact with N transmitting channels each with transmission probability T_i is:

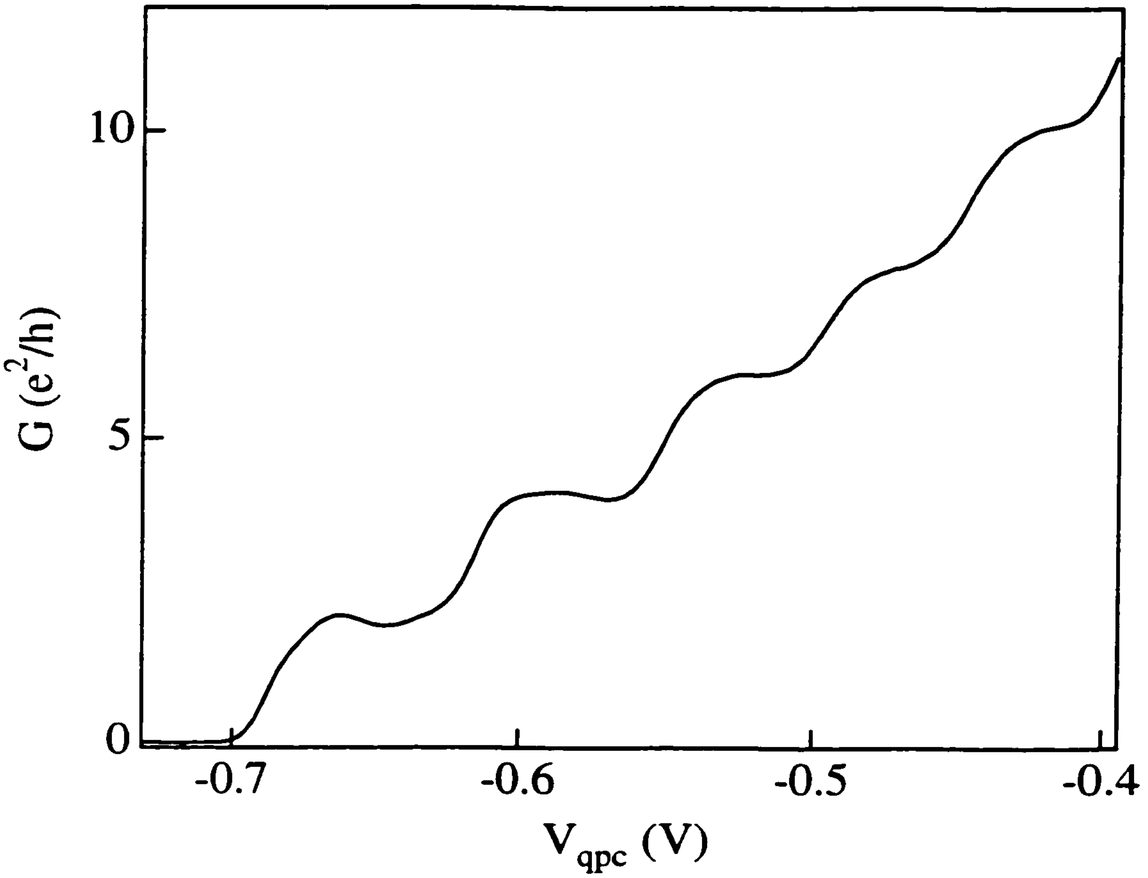

Figure 2.2 Measured zero-bias differential conductance G through a quantum point contact as a function of the voltage V_{qpc} on the point contact gate. Conductance increases stepwise as the point contact width is increased by increasing V_{qpc}. Step heights are multiples of $2e^2/h$, modulated by additional structure due to quantum interference of electron waves.

$$G = \frac{2e^2}{h}\sum_{i=1}^{N} T_i$$

For an ideal point contact at T = 0 K, $T_i = 0$ for channels with energies above the Fermi energy, and $T_i = 1$ for channels with energies below the Fermi energy. The resulting point contact conductance is simply the number of transmitting modes times the conductance quantum G_Q. This simple result is due to a fortuitous cancellation of the energy dependence of the conductance, which involves the product of the density of states in one dimension $\rho(E)$ and the electron kinetic energy E_k. Because $\rho(E)$ scales inversely as the square root of the energy, and E_k scales as the square root of the energy, the energy dependence cancels in the product. Consequently, each channel contributes equally to the total point contact conductance.

The experimental situation can differ somewhat from the ideal situation described above, as is clear from a close examination of Fig. 2.2. The sides of the conductance steps are never perfectly vertical, as the above equation would imply, due to thermal smearing. In addition, the steps in the conductance at multiples of G_Q are often not perfectly flat but are modulated by additional structure. This structure is reproducible as the contact voltage is ramped. This common occurrence in quantum point contact traces is due to interference of electron waves passing through the point contact. Obstructions near the contact, such as additional gates or impurities, can cause backscattering of electron waves resulting in transmission probabilities $T_i < 1$, causing deviations from the theoretical prediction.

In the experiments of this thesis, quantum point contacts are not studied in their own right, but are used as building blocks for more complicated structures. In a quantum dot, point contacts serve as tunnel junctions coupling the dot to its leads through which electrons tunnel on and off the dot. Tunnel junctions formed in this way have a distinct advantage over those formed in metal systems. In our systems, the junction conductance can be adjusted *in situ* by adjusting V_{qpc}, whereas in metal systems the junction conductance is fixed in fabrication. This facilitates the study of phenomena in quantum dots which depend strongly on this coupling, such as charge quantization, which is the focus of the experiments described in Chapter 4.

2.4 Quantum dots

As described above, the split-gate fabrication technique can be used to form small, isolated puddles of electrons in the two-dimensional electron gas: quantum dots. Quantum dots formed in this manner are typically coupled to 2DEG leads via adjustable quantum point contacts, enabling transport spectroscopy measurements to be carried out and a wide variety of phenomena investigated. For weak coupling, the number of electrons on the dot is an integer. For the dots described in this thesis, the number of electrons ranges from ~ 30 in the smallest dots to ~ 700 in the largest. The initial investigations into such systems as well as the underlying theory are documented in several review articles [Beenaker and van Houten, 1991; Kastner, 1992; Grabert and Devoret. 1992] which also contain extensive references. A good review of the experimental literature can be found in [Sohn *et al.*, 1996].

The fundamental phenomenon which dominates the behaviour of a quantum dot is the Coulomb blockade of tunneling: under certain conditions, a fixed integer number of electrons on the dot will be stable against electrons tunneling on or off the dot due to the electrostatic energy cost associated with such an event [see for example Grabert and Devoret, 1992]. In order to observe the Coulomb blockade, two conditions must be satisfied. Firstly, the coupling of the dot to its leads must be weak. Formally,

$$G_{qpc} << \frac{2e^2}{h}$$

where G_{qpc} is the conductance of the tunnel junctions coupling the dot to its leads, e is the electron charge, and h is Planck's constant. This condition is derived from the uncertainty principle by requiring that the charging energy $U = e^2/C$, where C is the total capacitance of the dot, be greater than the energy uncertainty corresponding to the RC lifetime of the electron on the dot [see for example Tinkham, 1996]. This condition ensures that the number of electrons on the dot is a well-defined integer. The second condition is that the charging energy be much greater than the temperature, or

$$U \equiv \frac{e^2}{C} >> kT$$

This ensures that charge quantization on the dot is not washed out by thermal fluctuations. A typical dot capacitance is on the order of a few hundred attofarads. For C = 500 aF, U ~ 3.7 K. In experiments, it is desirable to have U >> 4kT due to the Fermi-Dirac distribution of electrons in the leads. For this reason, dilution refrigerator temperatures are usually necessary to observe very robust Coulomb blockade effects.

The Coulomb blockade, as well as many phenomena in quantum dots, can be visualized in an energy diagram such as that shown in Fig. 2.3. In Fig. 2.3 (a), three regions are shown, the two leads and the quantum dot. The vertical axis of Fig. 2.3 (a) is the energy of electrons in each region. The dot is separated from the leads by vertical bars representing the tunnel junction energy barriers. The chemical potentials of the left and right leads are labeled μ_L and μ_R, respectively. In each lead there is a continuum of energy states filled up to the Fermi energy E_f. In the dot, there is an integer number of electrons, which, if the quantized level spacing in the dot is sufficiently small, can also be thought of as filling a continuum of states. However, because of electron interactions in the dot, there is a gap between the energy of the highest filled state and the energy of the dot with one more electron; this gap is the charging energy U. In this case, electrons are "blockaded" from tunneling on to the dot, because the energy cost is too great. The situation changes if the energy of the electrons in the dot is lowered sufficiently, which can be accomplished by varying the voltage on an electrode capacitively coupled to the dot. This is illustrated in Fig. 2.3 (b), where the Fermi level of the leads now lines up with the energy of the next available state in the dot. In this case, an electron can tunnel

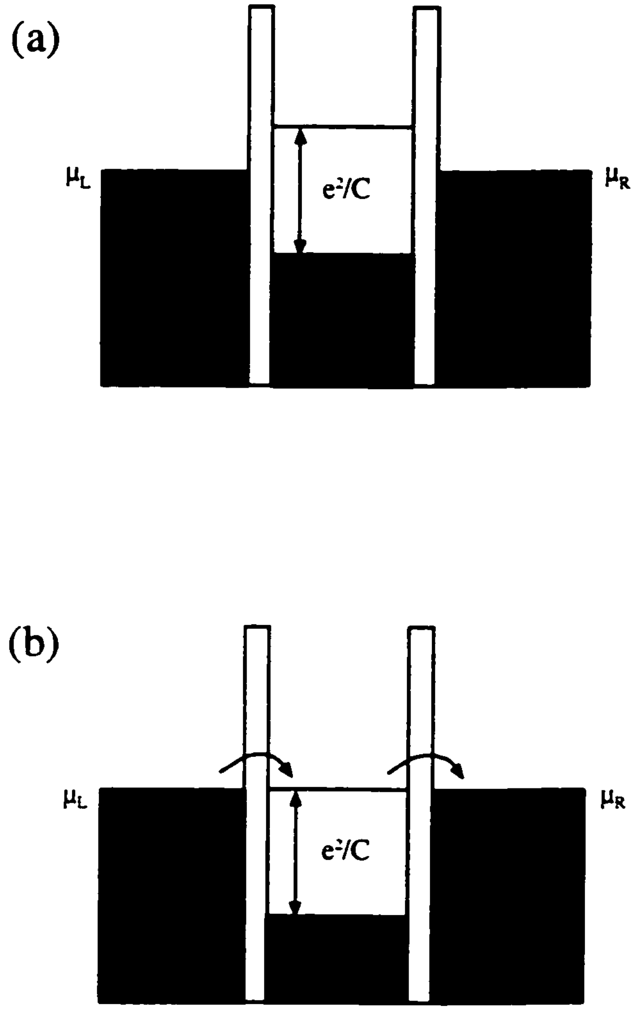

Figure 2.3 Energy diagrams illustrating Coulomb blockade of tunneling through a quantum dot. In (a), the the energy gap between the highest filled state in the dot and the next available state is too high for an electron to tunnel on to the dot, resulting in the Coulomb blockade of transport. In (b), the energies in the dot have been tuned using a gate electrode such that the next available state for transport aligns with the electrochemical potentials of the electrons in the leads. In this case, electrons can tunnel on and off of the dot one at a time.

on and current can flow through the dot one electron at a time. Such an effect is responsible for the canonical experimental signature of Coulomb blockade in quantum dots: the appearance of quasi-periodic peaks in the dot conductance which occur as the voltage on a capacitively coupled gate electrode is varied.

In order to understand this and other effects, a model for the quantum dot system is needed. The simplest candidate is the capacitive charging model [Kulik and Shekhter, 1973; Van Houten and Beenakker, 1989; Averin and Likharev, 1990; Tinkham, 1996]. In this model, we ignore the quantization of energy in the dot and treat the system as a metal island connected to voltage sources via capacitors and to leads via tunnel junctions. The variables in this approach are the voltages of the voltage sources and the number of electrons N on the dot. Given these quantities, we calculate the total system electrostatic energy by adding up the energy in the capacitors and subtracting the work done by the voltage sources to charge them up. Minimizing this expression with respect to N gives the number of electrons on the dot which is stable. I will outline this procedure and explain how the Coulomb blockade peak behaviour follows.

The approach followed is that of Tinkham [1996]. Fig. 2.4 shows a circuit diagram which models the dot as an island on which there is an integer number of electrons N connected to a drain and a source via tunnel junctions. The junctions are depicted as hatched boxes, and are characterized by a tunnel resistance R and a capacitance to the leads C_L. Also shown is a battery capacitively coupled to the dot via a capacitance C_g. The remainder of the dot capacitance to the outside world is C_o; thus, the total capacitance of the dot is $C_\Sigma = C_g + 2C_L + C_o$. The bias across the dot is V_{ds}.

The first step is to calculate the potential ϕ of the dot island; this is given by:

$$\phi = \frac{C_g V_g + V_{ds} C_L - Ne}{C_\Sigma}$$

Once this potential is known, the energy stored in the capacitors can be calculated:

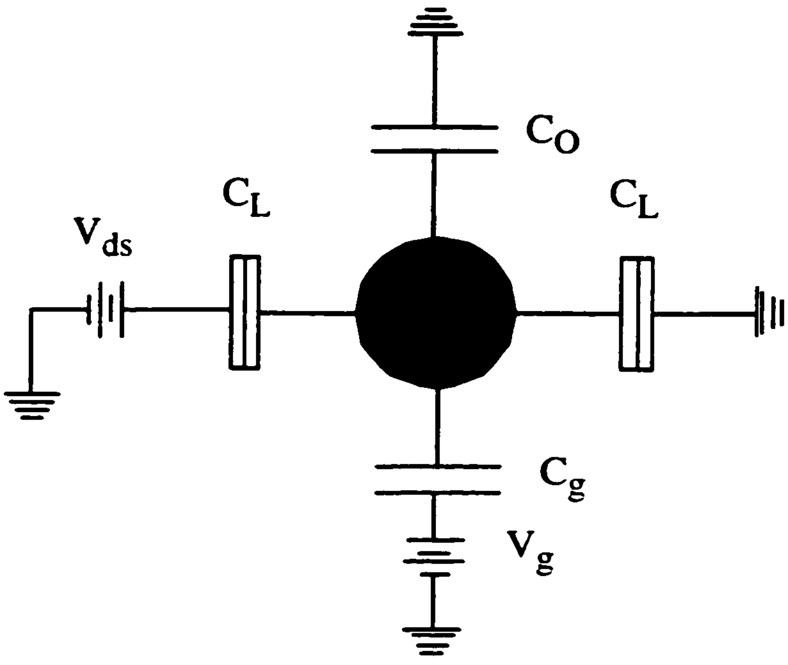

Figure 2.4 Circuit diagram of a quantum dot for formulating the capacitive charging model. The dot is modeled as a metal island with an integer number of electrons N, capacitively coupled to a voltage source V_g. The dot is coupled to two leads via tunnel junctions, depicted as hatched boxes in the diagram. A drain-source voltage V_{ds} can be applied across the dot.

$$U = \frac{1}{2}\sum_i C_i(\Delta V_i)^2$$

where ΔV_i is the voltage across the i^{th} capacitor. We subtract from this expression the work done by the batteries:

$$W = \sum_i C_i V_i(V_i - \varphi)$$

Because we are first interested in understanding zero-bias measurements, we will for the moment assume that $V_{ds} = 0$. Substituting in the above expressions, re-arranging, and dropping terms independent of N, we arrive at the following expression for the electrostatic energy $E(V_g, N)$:

$$E(V_g.N) = \frac{(C_g V_g - Ne)^2}{2C_\Sigma}$$

Terms independent of N can be ignored because transport through the dot is governed by differences in $E(V_g, N)$ between dot states with differing numbers of electrons N; when calculating such differences, all terms independent of N drop out. The expression for $E(V_g, N)$ has a simple interpretation as the energy cost to maintain a disparity between the actual dot charge Ne and the induced dot charge $C_g V_g$. The actual dot charge increases stepwise as V_g is ramped, whereas the induced dot charge increases linearly. This is illustrated in Fig. 2.5 (a).

In Fig. 2.5 (b), $E(V_g, N)$ is plotted vs. gate voltage V_g for different values of dot charge N. For fixed N, the curve is parabolic in V_g; each parabola corresponds to a different value of total dot charge N. For a given value of V_g at zero temperature the number of electrons corresponding to the lowest energy parabola is stable. For most values of V_g this number will be well-defined, as the energy cost to add an additional electron will be too high. However, at certain values of V_g, the lowest energy state occurs where two parabolas intersect. At such a point, the energies for the states with N and N+1 electrons are equal, and the dot charge can fluctuate without energy cost between these two values. Thus, electrons can flow through the dot one at a time, and a peak in

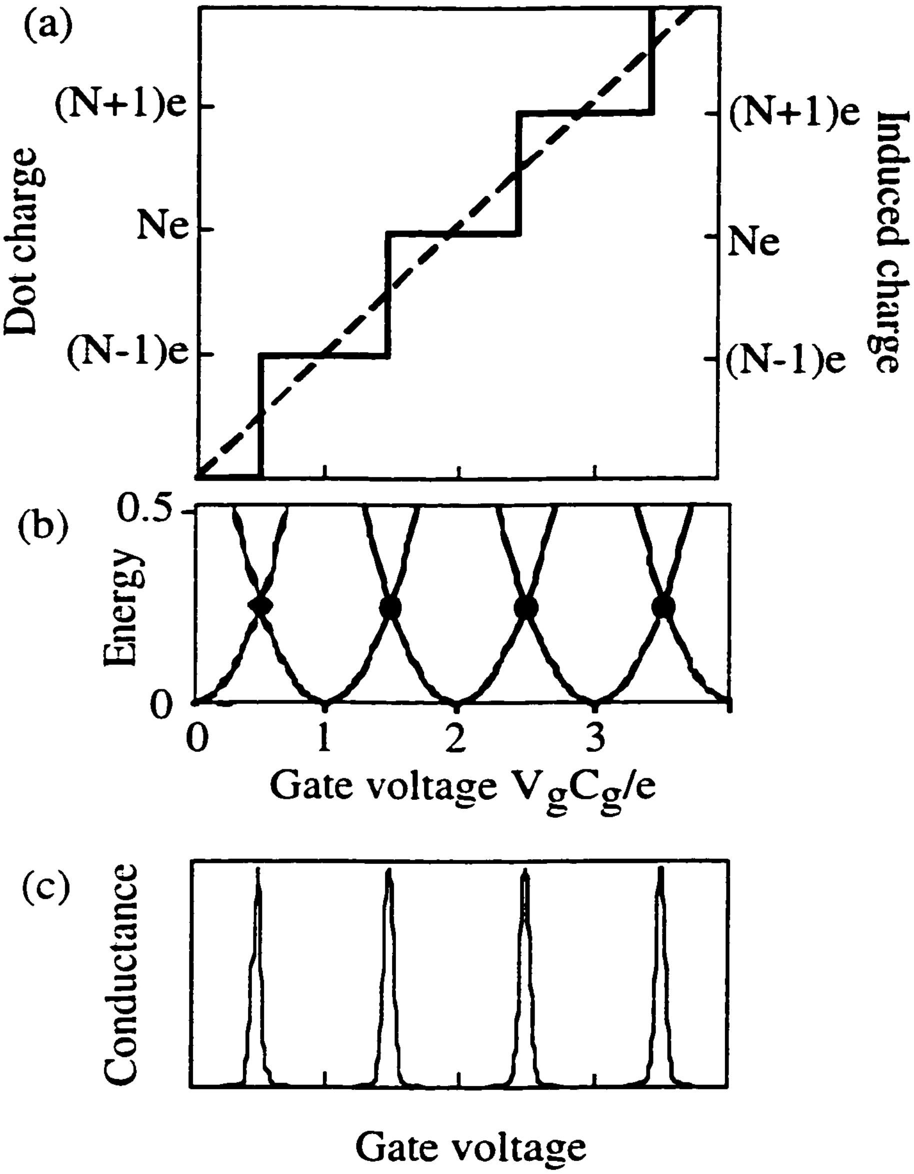

Figure 2.5 Schematic illustrating Coulomb blockade. (a) Induced dot charge (dashed line) and actual dot charge (solid line) on the quantum dot. Induced charge rises linearly with gate voltage V_g; actual charge rises in steps, due to the constraint that the charge on the dot be an integer number of electrons. (b) Electrostatic energy of the dot. For fixed N, energy dependence on V_g is parabolic. Current can flow at points where two parabolas intersect, shown as black dots. (c) Conductance through the dot vs. V_g. Peaks in the conductance occur at V_g values where two parabolas intersect in (b). Figure adapted from Livermore [1998].

the measured dot conductance will occur. This is the origin of the Coulomb blockade conductance peaks, which occur as V_g is tuned through these charge degeneracy points. These peaks are depicted in Fig. 2.5 (c) and align precisely with the points where the parabolas intersect in Fig. 2.5 (b). The spacing between peaks is given by:

$$\Delta V_g = \frac{e}{C_g} = \frac{E_C}{\alpha e}$$

where $\alpha = C_g/C_\Sigma$ is the capacitive lever-arm between the change in gate voltage and the charge induced on the quantum dot, useful for converting from gate voltage to energy.

Fig. 2.6 is data illustrating the Coulomb blockade peak behaviour. This data depicts the zero-bias differential conductance through a quantum dot as a function of the sidegate voltage V_g, measured at a dilution refrigerator base temperature of 25 mK. Coulomb blockade peaks in the conductance are clearly visible. However, several features in the data point out the limitations of the capacitive charging model. Firstly, this model predicts a strict, constant periodicity of the Coulomb blockade peaks. The data show that the spacings between Coulomb blockade peaks are roughly equal, but not strictly so. Also, although the model makes no explicit prediction about the heights of the Coulomb blockade peaks, we can infer they should be constant and dependent on the conductances of the tunnel junctions. In fact, the peak heights vary from one peak to the next. In order to explain these discrepancies, our model will have to be refined to incorporate the effects of a discrete level spectrum in the quantum dot.

The degree to which the discrete level spectrum is manifested in a quantum dot depends on the dot size, the number of electrons it contains, and the temperature. A dot with area A_{dot} will contain $N = n_s A_{dot}$ electrons, where n_s is the electron sheet density. We can obtain a rough estimate of the discrete level spacing $\Delta\varepsilon$ by assuming that the electrons fill spin-degenerate discrete states up to the Fermi level; the level spacing is then:

$$\Delta\varepsilon = \frac{2\varepsilon_f}{N}$$

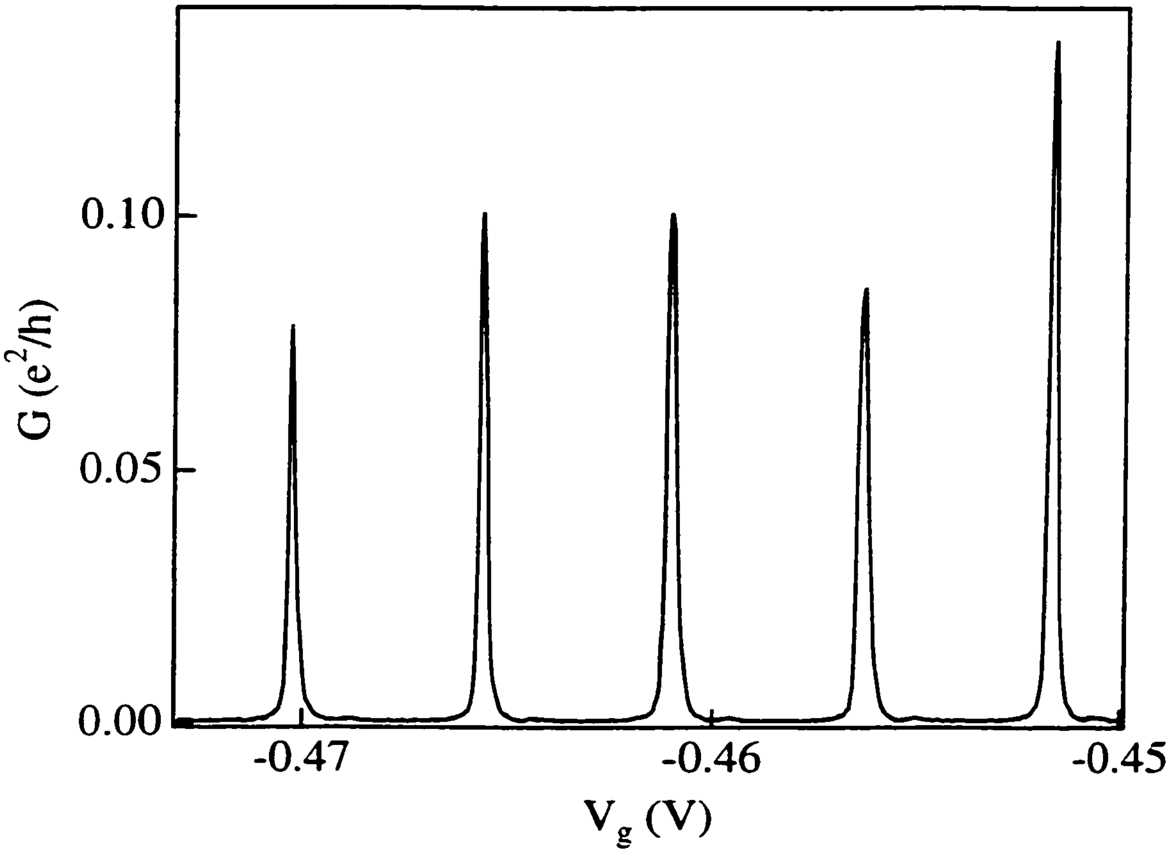

Figure 2.6 Measured differential conductance through a quantum dot vs. sidegate voltage V_g. Coulomb blockade peaks in the conductance are appear as V_g is swept. The spacing between peaks corresponds to the energy to add a single additional electron to the dot. These spacings enable the determination of the gate capacitance C_g. Peak heights vary due to the tunneling of electrons in to discrete quantum levels.

For these levels to be resolvable, the level spacing must be less than the energy width of the Fermi-Dirac distribution:

$$\Delta\varepsilon << 3.5kT$$

A 300 x 300 nm^2 dot with a sheet density of $3.5 \times 10^{11}/cm^2$ contains approximately 315 electrons, and the corresponding level spacing is 80 μeV. This corresponds to a temperature of approximately 1 K, and thus the effects of the discrete spectrum will be observable at dilution refrigerator temperatures.

The simplest model incorporating quantum confinement effects is the constant interaction model [Meir *et al.*, 1991; Beenakker, 1991]. In this picture, all electron-electron interactions are lumped into one parameter $U = e^2/C$, the charging energy, which is assumed to remain constant as electrons are added to the dot. Thus, each time an electron is added, the same energy cost U must be paid. In addition, this model decouples the discrete spectrum of energy levels in the dot from the electron-electron interactions, i.e. the quantum confinement and interaction energy terms in the Hamiltonian are assumed to be separable. This is again a big assumption, since in reality the two are interdependent, especially in the regime $r_s \sim 1$. A further assumption is that each discrete level holds two electrons of opposite spin, an assumption that also turns out to be inaccurate, as will be explored further in Chapter 5 of this thesis. However, the model is a good first step towards understanding the energy spectra of quantum dots, and it explains surprisingly well the results of some experiments [Chang *et al.*, 1996; Folk *et al.*, 1996].

Fig. 2.7 shows energy diagrams that illustrate the constant interaction model. In this figure, the continuum of energy states in the dot has been replaced by a series of discrete states, each of which can hold two electrons. The average level spacing between electrons is $\Delta\varepsilon$. Fig. 2.7 (a) illustrates the Coulomb blockade in the case where the dot contains an even number of electrons. In this case, the energy barrier to add an additional electron to the dot is the charging energy U plus the level spacing $\Delta\varepsilon$. In the case of an odd number of electrons, only the charging energy U needs to be provided, as in

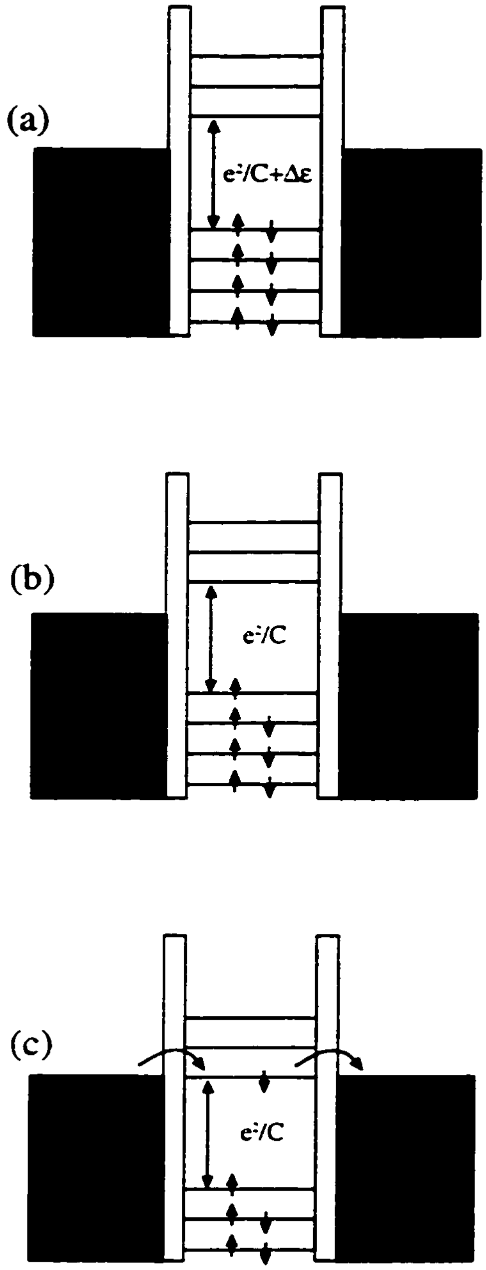

Figure 2.7 (a) Energy diagram illustrating constant interaction model. (a) For an even number of electrons in the dot, the energy barrier to add an additional electron is the charging energy plus the level spacing Δε. (b) For an odd number of electrons in the dot, the energy barrier to add an electron is simply the charging energy; in this model, discrete levels in the dot are spin degenerate. (c) An electron can be transported through the dot when an available level is aligned with the leads.

Fig. 2.7 (b). The levels in the dot can again be raised and lowered by varying the voltage of the sidegate, V_g. When an available level is aligned with the chemical potentials of the leads, as in Fig. 2.7 (c), transport can occur through the dot one electron at a time.

This model implies that, due to the electron spin and the corresponding twofold degeneracy of discrete levels in the dot, the spacings between Coulomb blockade peaks will alternate, depending on whether the dot contains an even or odd number of electrons. This is due to the additional energy cost $\Delta\varepsilon$ that must be paid to add an odd electron. Observation of such an alternation would be strong evidence that electrons fill spin-degenerate levels in quantum dots. In fact, the alternation should not be precise because the level spacing is not constant as electrons are added to the dot. However, the peak spacings might still be expected to alternate on average, with a bimodal distribution of spacings. Experiments, however, have shown otherwise. In extensive measurements on Coulomb blockade peak spacings, Patel *et al.* [1997] did not observe such an alternation in peak spacings, or even a bimodal distribution of spacings. Some evidence of such alternation was observed by Goldhaber-Gordon [1999] for a very small dot in a strong parallel magnetic field over a small range of Coulomb blockade peaks. The conditions under which the electron spin is manifested in semiconductor quantum dots is the subject of Chapter 5 of this thesis.

The discrete energy spectrum of quantum dots is also manifested in other properties of Coulomb blockade peaks, in particular peak heights and lineshapes. The height of a Coulomb blockade peak depends on the degree of overlap between the wavefunction of an electron on the dot and the wavefunctions of electrons at the Fermi level in the leads; this overlap varies from one quantum level to the next. Several experiments have studied statistics of Coulomb blockade peak heights in order to understand the nature of the discrete spectrum in a quantum dot [Chang *et al.*, 1996; Folk *et al.*, 1996]. In particular, Coulomb blockade peak heights have been shown to be distributed according to the predictions of random matrix theory, which describes the statistics of energy level distributions in a wide variety of quantum chaotic systems [Beenakker, 1997].

The lineshapes of Coulomb blockade peaks also depend on the relative importance of the discrete energy spectrum for transport, i.e. on whether transport occurs in the "classical Coulomb blockade" regime ($\Delta\varepsilon << kT << E_C$) or in the "quantum Coulomb blockade" regime ($kT << \Delta\varepsilon << E_C$). In the classical Coulomb blockade regime, transport occurs via many quantum states [Kulik and Shekhter, 1975; Glazman and Shekhter, 1989] and the lineshape is given by:

$$G = G_p \frac{(\phi_{dot} - \phi_o)/kT}{\sinh((\phi_{dot} - \phi_o)/kT)} \approx G_p \cosh^{-2}\left(\frac{\phi_{dot} - \phi_o}{2.5kT}\right)$$

where G_p is the peak height, which is constant and given by:

$$G_p = \frac{e^2 \Gamma_L \Gamma_R}{2\Delta\varepsilon(\Gamma_L + \Gamma_R)}$$

and

$$\phi_{dot} - \phi_o = \frac{e^2}{C_\Sigma}\left(\frac{C_g}{e}(V_g - V_o)\right)$$

is the distance between the potential of the dot and the peak position. Γ_L and Γ_R are the tunneling rates through the left and right point contacts, respectively, C_Σ is the total capacitance of the dot, and V_o is the gate voltage position of the peak center. In the quantum Coulomb blockade regime, transport occurs via a single discrete quantum level [Beenakker, 1991; Meir *et al.*, 1991], and the lineshape is given by:

$$G = \frac{\pi e^2 kT \Gamma_L \Gamma_R}{2h(\Gamma_L + \Gamma_R)} \cosh^{-2}\left(\frac{\phi_{dot} - \phi_o}{2kT}\right)$$

In this case, the peak heights are not constant but depend on the two tunneling rates, which vary from one quantum level to the next depending on the degree of wavefunction overlap.

The properties of quantum dots which have been described thusfar are observable in zero-bias transport measurements. However, much useful information can be obtained by making finite-bias measurements. To predict what should occur in such a situation, the capacitive charging model can be extended to include a finite drain-source bias V_{ds}. For the moment, the effects of a finite level spacing will again be ignored. We again refer to the circuit diagram of Fig. 2.4 and follow a similar procedure to that outlined above to compute the electrostatic energy E(N, V_{ds}, V_g), following the treament of Crouch [1996]. In this case, the work done by the batteries depends on through which junction the electron has tunneled on to the dot. The work term becomes:

$$W = V_{ds}C_L(V_{ds} - \phi) + V_gC_g(V_g - \phi) - eN_tV_{ds}$$

where N_t is the number of electrons which have tunneled on to the dot through the *left* junction in Fig. 2.4. Using this expression, we compute the electrostatic energy to be:

$$E(n) = \frac{e^2}{2C_\Sigma}\left(N - \frac{C_gV_g}{e} - \frac{C_LV_{ds}}{e}\right)^2 - N_tV_{ds}$$

again dropping terms independent of N.

The Coulomb blockade conditions for finite V_{ds} can be determined by considering a dot containing N electrons. We calculate the change in the energy ΔE for each of the four possible tunneling events: a single electron tunneling on or off through either the left or right junction. For example, a single electron tunneling on through the left junction is described by:

$$\Delta E_L(N \to N+1) \equiv E(N+1) - E(N)$$

which means a single electron tunneling on to the dot through the left junction. For any of these events to occur, ΔE must be ≤ 0. The four resulting inequalities describe the regions of gate voltage V_g and drain-source voltage V_{ds} for which the number of electrons N on the dot is stable, i.e. the Coulomb blockade regions:

$$N + \frac{1}{2} > \frac{C_gV_g}{e} - \frac{(C_\Sigma - C_L)V_{ds}}{e} > N - \frac{1}{2}$$

$$N + \frac{1}{2} > \frac{C_gV_g}{e} + \frac{C_LV_{ds}}{e} > N - \frac{1}{2}$$

These equations describe rhombic-shaped regions of Coulomb blockade in the V_g-V_{ds} plane, or "Coulomb diamonds." The exact shape of the measured Coulomb diamonds determines important energy scales in the quantum dot.

This is illustrated in Fig. 2.8 (a), which is a schematic of a single Coulomb diamond. The slopes of diamond boundaries, as well as the height and width of the diamond, can be used to extract the gate capacitance C_g, the capacitance to the leads C_L, and the total capacitance of the dot C_Σ. This information can be used to compute the charging energy of the dot. Fig. 2.8 (b) is data measured on one of the quantum dots I studied, showing the clear diamond regions of Coulomb blockade. The dark regions correspond to low conductance, light regions to high conductance. This dot has lithographic dimensions of 0.5 x 0.6 μm^2 and was fabricated from a heterostructure with a 2DEG sheet density of 3 x $10^{11}/cm^2$. Also evident in Fig. 2.8 (b) are several stripes parallel to the left upper edges of the Coulomb diamonds which occur as V_{ds} is increased. These are again due to the discrete energy levels in the dot, and correspond to excited states which become accessible as V_{ds} is increased. These additional peaks enable the measurement of the energy scale for the discrete levels in the dot, and will be discussed in more detail in Chapter 5.

Tunneling through excited states is illustrated in another set of energy diagrams in Fig. 2.9. In Fig. 2.9 (a), electrons are prevented from tunneling on to the dot by the Coulomb blockade. In Fig. 2.9 (b), a finite drain-source bias eV_{ds} has been placed across the dot, elevating the chemical potential in the left lead and providing electrons with sufficient energy to overcome the Coulomb blockade. In Fig. 2.9 (c), V_{ds} has been raised still further, enabling electrons to tunnel through the first excited state in the dot as well. This additional tunneling path is manifested as an additional peak in the differential conductance at this value of V_{ds}.

2.5 Conclusion

In this chapter theories have been described which provide a basis for understanding the properties of quantum point contacts and quantum dots. These theories, in

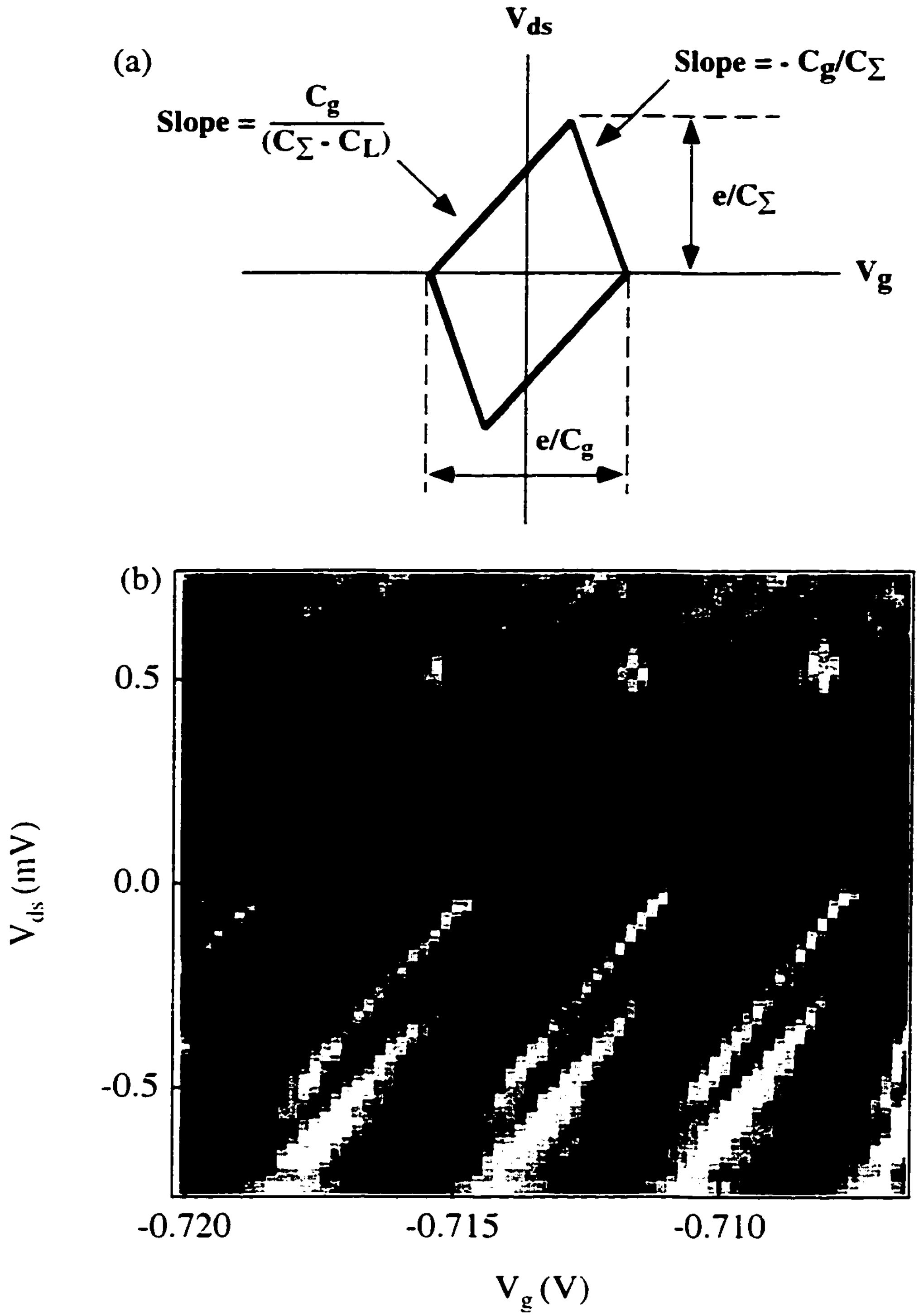

Figure 2.8 (a) The shape of a Coulomb diamond in the V_g-V_{ds} plane. The slopes of this diamond yield key capacitance values and energy scales of the quantum dot. (b) Measured differential conductance through the quantum dot vs. V_g and V_{ds} showing Coulomb diamond behaviour. Stripes parallel to left upper edges of diamonds are due to electron tunneling through excited states.

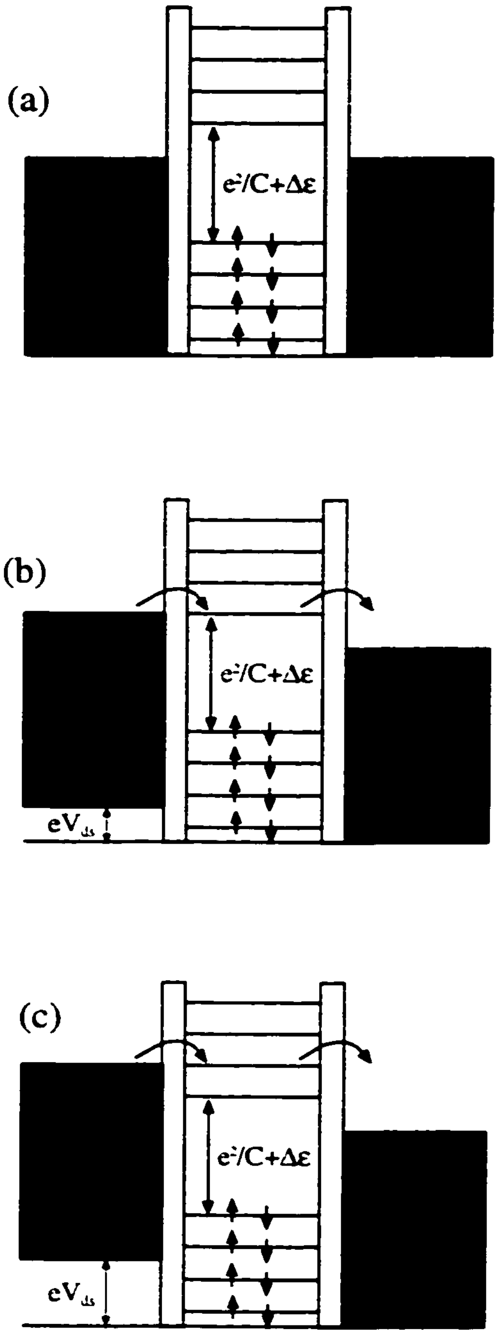

Figure 2.9 Tunneling through excited states in a quantum dot. In (a) no current can flow due to the Coulomb blockade of tunneling. In (b) a finite drain-source bias V_{ds} allows electrons to overcome the energy barrier and tunnel through. In (c) a larger drain-source bias allows electrons to tunnel through the first excited state of the dot.

particular the theory of Coulomb blockade, will be referenced frequently in the remainder of this thesis as individual experiments are discussed. These experiments illustrate both the applicability and the limitations of these theories. Additional theoretical background will be discussed in the context of the individual experiments.

Chapter 3

Experimental Methods

3.1 Introduction

This chapter describes the experimental methods used to fabricate and make measurements on two-dimensional electron gas nanostructures. The purpose of this chapter is twofold: to provide the basis for understanding the experiments described in subsequent chapters, and to serve as a reference for future generations of students who will undertake similar experiments. For the latter reason, some procedures are described in detail, and notes on equipment safety are included. Many of these techniques have been developed and used by other Westervelt group members or by other research groups, and are well described in previous student theses. Thus, to avoid redundancy, I will merely give an overview of such techniques, along with appropriate references, and focus on supplementing it with insights derived from my own experience.

This chapter contains three sections: the first covers the properties of our GaAs/AlGaAs heterostructure wafers and the formation of the 2DEG in these heterostructures. The second section covers the procedures for fabricating split-gate devices and describes in detail the numerous steps including wafer processing, electron beam lithography, metal deposition, and wirebonding. The final section describes measurement techniques for quantum dot nanostructures, including cryogenic and low-noise methods. In particular, I discuss the use of our Kelvinox dilution refrigerators and the lambda fridge component of our Kelvinox 400. I also describe the procedures used for tuning and for making linear and nonlinear conductance measurements on quantum dots in magnetic fields.

3.2 2DEG Heterostructures

The starting point for our work is a GaAs/AlGaAs heterostructure grown using molecular beam epitaxy by our collaborators at UCSB or Lucent Technologies. The technique of molecular beam epitaxy enables the precise growth of a heterostructure one atomic layer at a time, resulting in exceptionally clean interfaces between layers. This enables the growing of alloys with precisely engineered band structures. An overview of the molecular beam epitaxy technique can be found in Herman and Sitter [1989]. All of the wafers used for the devices described in this thesis were grown by Kevin Maranowski, working in the laboratory of Art Gossard at UC Santa Barbara. A description of the procedures and equipment used at UCSB can be found in previous Westervelt student theses [Hopkins, 1990; Baskey, 1994].

The technique used for forming the 2DEG in our heterostructures is the modulation doping technique [Stormer *et al.*, 1978; Dingle *et al.*, 1978], illustrated in Fig. 3.1. This figure depicts a cross-section of a typical wafer used in our experiments, which consists of several layers grown on top of a GaAs substrate. These layers are 100 nm AlGaAs, a 25 period smoothing lattice consisting of alternating layers of GaAs and AlGaAs, a one micron layer of GaAs, 22 nm of AlGaAs, a single atomic donor layer of Si (termed a "delta-doping" layer) with concentration $8\times10^{12}/\mathrm{cm}^2$, another 30 nm of AlGaAs, and a 5 nm GaAs cap. The AlGaAs is more accurately notated $\mathrm{Al_xGa_{1-x}As}$; the mole fraction $x = 0.3$ in our case. This quantity can be varied to tune the conduction band offset between the GaAs and the AlGaAs. I will omit these subscripts for the sake of clarity.

Below this diagram is a graph depicting the conduction band structure of the wafer, illustrating the 2DEG formation. Each Si atom in the donor layer replaces a Ga atom in the GaAs lattice, and thus each Si atom is left with one unbonded donor electron. Some fraction of these electrons will migrate to the interface of the GaAs/AlGaAs, where there is a conduction band offset between the two materials. The positively ionized Si donor atoms left behind create an attractive potential which bends these bands, forming an accumulation layer at the interface, as depicted in the inset. If the concentration of Si

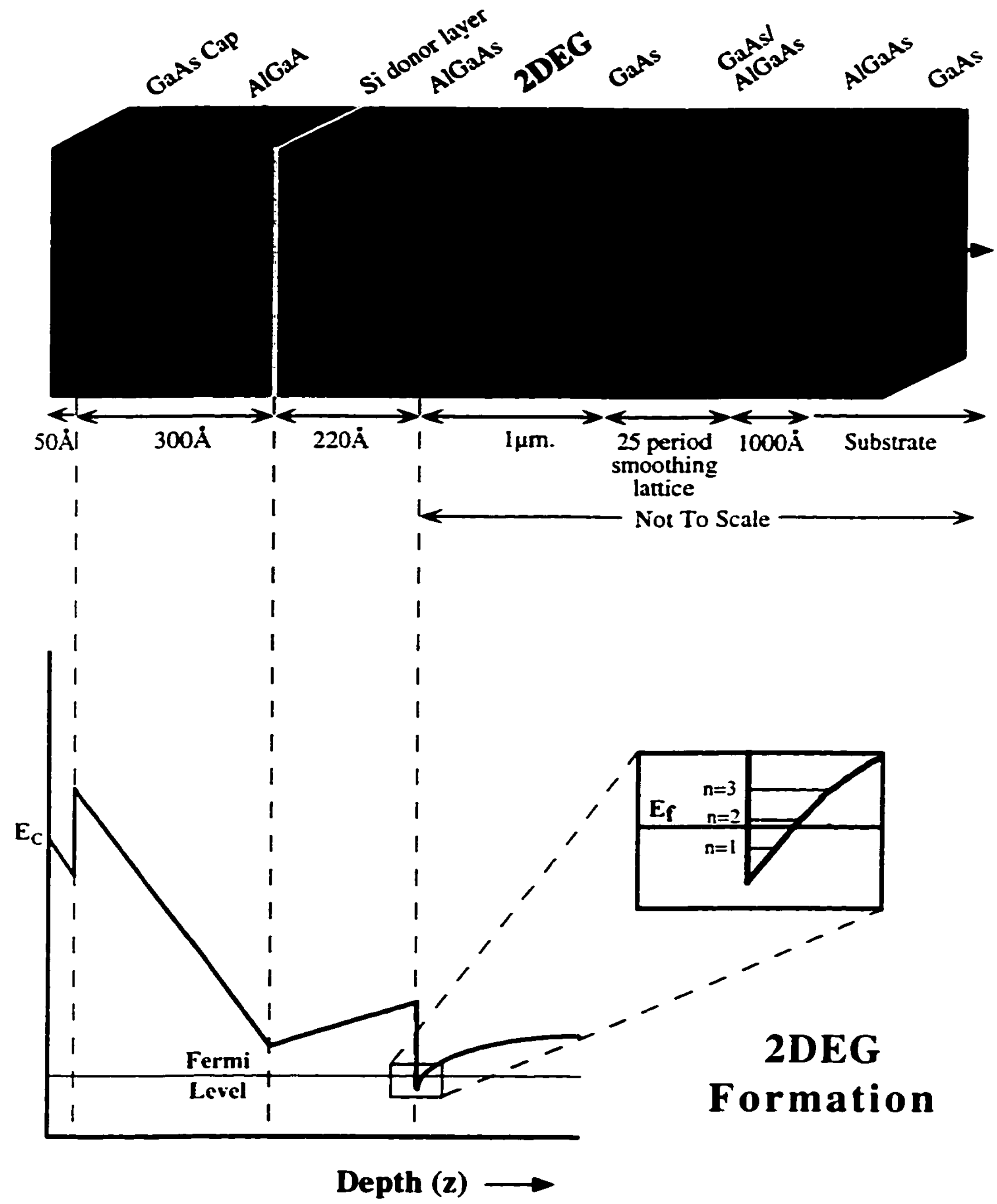

Figure 3.1 Cross-section of GaAs/AlGaAs heterostructure and corresponding band structure illustrating the formation of the two-dimensional electron gas (2DEG). Electrons from a Si delta-doping layer migrate to the interface of the GaAs and AlGaAs layers, where they are trapped in a triangular potential well formed by the conduction band offset between these two materials and the band bending induced by the ionized donor potential. For appropriate dimensions and dopant concentrations the resulting Fermi level lies between the two lowest quantized energy levels in the well, forming a 2DEG.

donors and the layer thicknesses are chosen correctly, only the first quantized level in the accumulation layer dips below the Fermi level of the system, as shown in the inset, forming a two-dimensional electron gas at the interface. The thickness of this layer is approximately 5 nm. The sheet density of electrons in the 2DEG depends on the dopant layer density and depth, and on the thicknesses of the heterostructure layers, and can be determined using a self-consistent electrostatics calculation, as described in Katine [1996].

The material properties of the modulation doped GaAs/AlGaAs heterostructures are particularly well-suited to studying mesoscopic systems such as quantum dots. The delta-doping layer is removed from the 2DEG interface, which reduces scattering of electrons from the ionized donors. The lattices of GaAs and AlGaAs are well matched (the lattice constants are 5.65 Å for GaAs and 5.66 Å for AlGaAs), which minimizes scattering due to interface defects, enabling high mobilities to be attained. Mobility is also enhanced by the low effective mass of electrons in GaAs (0.067 m_e). This high mobility corresponds to mean free paths for scattering > 4 μm, enabling our experiments to be carried out in the ballistic transport regime. However, a tradeoff must be made between high mobility and 2DEG depth. A near-surface 2DEG is desirable in order to precisely define the contours of the devices using the split-gate method. On the other hand, the shallower the 2DEG depth, the stronger electron scattering from the surface is, which reduces mobility. In the wafers used in this thesis, 2DEG depths ranged from 47 nm to 57 nm, and mobilities ranged from 450,000 to 560,000 cm^2/Vs.

One particularly insidious problem with our heterostructure materials is termed switching noise. Electrons can switch on and off trapping sites in proximity to the 2DEG layer with a characteristic low frequency. This has been studied systematically in other groups [Dekker *et al.*, 1991; Timp *et al.*, 1990]. If switching events occur near a device fabricated in the 2DEG, such as a quantum dot, the abrupt changes in the electrostatic potential can affect the conductance properties of the device. Switching noise appears to be worse for some heterostructure wafers than for others, and even seems to depend on which section of a particular wafer is used. The Marcus group at Stanford found that switching noise could be reduced by cooling down their samples very slowly, for example by cooling down the dilution refrigerator without exchange gas. Another technique used was cooling the samples with small (~0.5V) positive voltages on the device gates. These tricks aim at achieving a dopant layer at base temperature in the lowest energy equilibrium state to minimize the possibility of switching [Stewart, 1999]. But some switching noise is a fact of life and must be dealt with through fast measurement techniques.

3.3 Device Fabrication

The fabrication of quantum dots using the split-gate technique involves many steps, and is both a science and an art. Many seemingly minor procedural details have been discovered through painful trial and error to be very important, so the reader interested in fabrication is advised to take note of them. As described in Chapter 2, two types of structures are made for the devices described in this thesis: ohmic contacts and Cr/Au gates. For both of these many of the fabrication steps are the same. An overview of the fabrication process for gates is depicted in Fig. 3.2. First, a polymethylmethacrylate (PMMA) is spun on the sample surface (1). Then, the desired patterns for gates are written in the PMMA layers using electron beam lithography (2). The exposed regions are developed away (3), resulting in an undercut in the PMMA layer. Metals are evaporated on the surface (4), and the unexposed regions are lifted off (5), resulting in metallic gates on the surface forming the nanostructure. At this point wirebonds are attached to the sample, and it is ready for measurement. The procedure for ohmic contact lithography is basically the same, with minor differences as discussed below. Each of these steps will be described in detail.

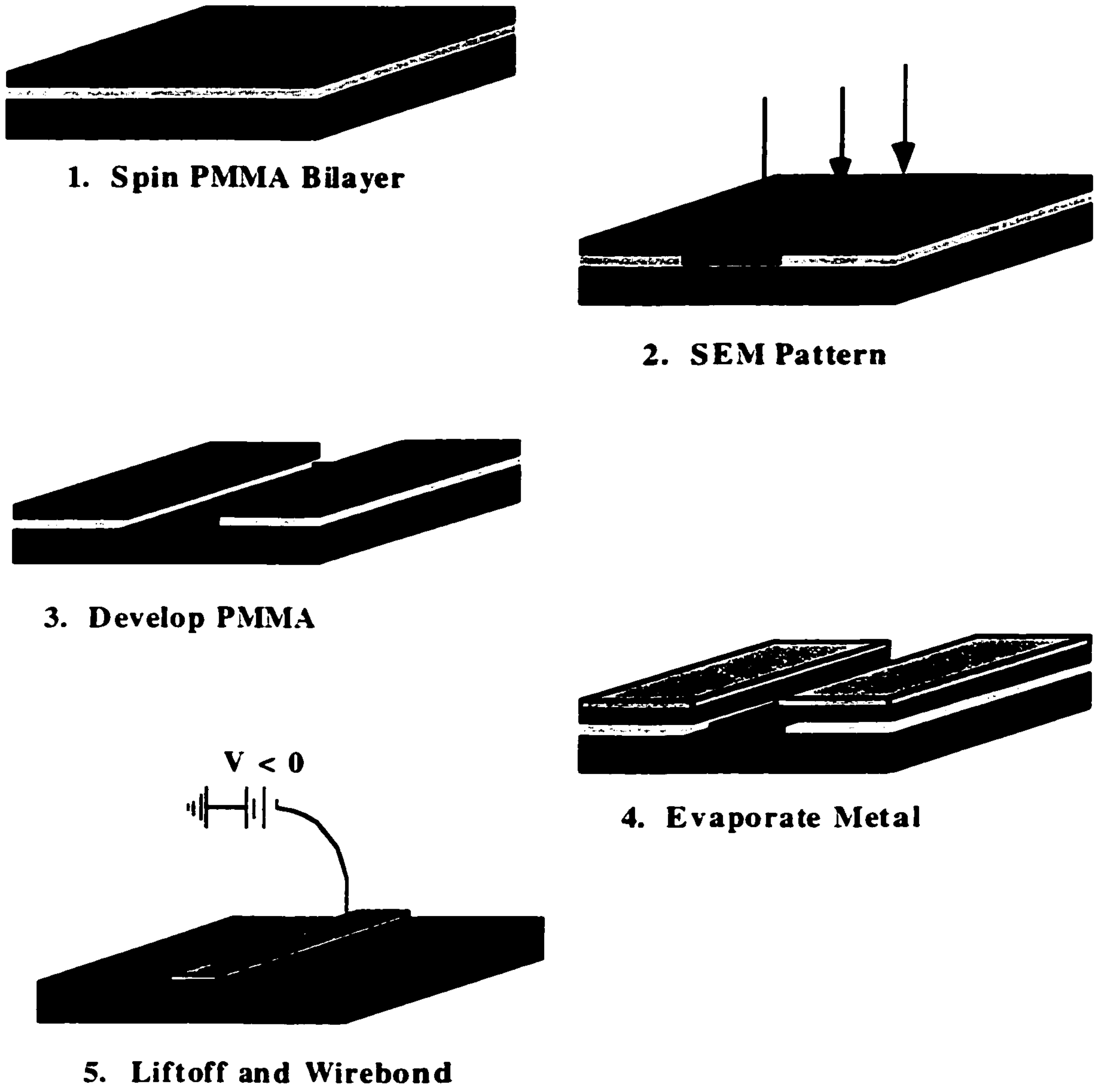

1. Spin PMMA Bilayer

2. SEM Pattern

3. Develop PMMA

4. Evaporate Metal

5. Liftoff and Wirebond

Figure 3.2 Overview of fabrication steps for making quantum dot nanostructures. 1. A bilayer of PMMA is spun on the surface of a chip cleaved from the heterostructure material; the layers differ in molecular weight. 2. The desired pattern is written in the PMMA bilayer using an electron beam microscope; the bottom layer of PMMA is exposed more easily. 3. The exposed PMMA is developed away, resulting in an undercut. 4. The desired metals are evaporated on the surface. 5. The unexposed regions are lifted off, leaving metal in the desired pattern on the surface. Wires are attached to the metal gates to apply voltages.

3.3.1 Wafer Processing

Microfabrication begins with a bare, uncleaved heterostructure wafer supplied to us by our collaborators at UCSB. All of the experiments described in this thesis were done with wafers KM1, KM2, and KM3, manufactured by Kevin Marañowski under the direction of Art Gossard. The first step is cleaving a chip off the wafer, as described in Katine [1996]. The size of the chip is determined by the tradeoff between conserving 2DEG material and the difficulty of handling a very small chip. My typical chip size was 3 X 4 mm. It is advisable to cleave and process several chips in one batch, as the marginal effort required to process one additional chip at each stage is low.

A safety note: GaAs dust is dangerous to inhale, as might be guessed from the presence of arsenic in this compound. When cleaving and blowing dust off of the wafer, a particle mask should be worn to prevent inhalation. Take great care to clean the cleaving area and wash hands after cleaving.

After cleaving, it is essential that the chips be well cleaned before proceeding with spinning and lithography. Any particles left on the surface before spinning will become embedded in the PMMA layer and can cause two types of problems: 1) particles located in areas where small features are written can result in defects in the metal gates on the surface, and 2) even more insidious, if the particles appear before ohmic contacts are fabricated, pinholes through the PMMA layers and consequently inadvertent pinhole-size ohmic contacts to the 2DEG can result. Such contacts can short out Cr/Au gates deposited over them in subsequent steps, and render a device unusable. The chip should be inspected under the optical microscope after cleaning and spinning to ensure that such contamination has not taken place.

Throughout the cleaning process, direct manipulation of the chips should be minimized. To ensure this, the chips are transported and cleaned in the small, perforated, teflon beakers found in the sample preparation room. If the chips are handled, plastic or teflon coated tweezers should be used, as metal tweezers can chip the edges of samples.

All solvents used for cleaning should be poured in, and, when open to air, stored in the fume hood. Trichloroethylene (TCE) is particularly dangerous, as it is a potent carcinogen, and should be handled with the utmost care. Each of the three chemicals used in the cleaning process – TCE, acetone, and methanol – should be poured in a beaker dedicated to that chemical, to minimize contamination.

The chips are cleaned according to the following recipe:

1) 15 minutes in boiling trichloroethylene (TCE). This is the principal cleaning step for the chip surfaces.
2) 15 minutes in acetone, while applying ultrasound. This step removes the TCE residue from the chip surfaces.
3) At least 5 minutes in methanol, while applying ultrasound. This step removes the acetone residue from the chip surfaces.

Steps 2 and 3, if not all three, should be performed in the class 100 inner clean room to minimize contamination from the air. Remove the chips from the methanol and from the teflon beakers one at a time, and immediately blow them dry with the high purity nitrogen gas found in the inner clean room. At this stage the samples are ready for spinning.

3.3.2 Spinning

In preparation for spinning, first lay 2 to 3 tekwipes out on the perforated metal surface in the fume hood in front of the spinner in the inner clean room. This will provide a clean surface on which to place the chips and PMMA droppers. Lay the tekwipes over a path from the spinner to the hotplate on which the PMMA layers will be baked; this seemingly minor detail is a useful precaution against dropping the chips in transport from spinner to hotplate, where they will immediately fall through the holes in the perforated metal surface and into the graveyard of lost chips haunted by the frustrations of previous generations of graduate students.

The PMMA droppers must also be cleaned prior to spinning. This is accomplished by spraying both the glass cylinders and the rubber bulbs with methanol, and blowing them dry with nitrogen. A careful examination of the bulbs will reveal that they are covered with particulates which can quickly be transferred to the surface of the chips and undo the careful chip cleaning. A separate dropper should be used for each layer of PMMA to avoid contaminating the PMMA in the source bottles. The spinner chuck should be cleaned with acetone before mounting it on the spinner.

A safety note: chlorobenzene, used as a solvent for PMMA, is a dangerous carcinogen. It is very easy to inhale, even when using it in the fume hood, especially when cleaning the spinner insert and chuck after spinning. We also have PMMA in a solvent of anisol rather than chlorobenzene, which is slightly less dangerous. Nevertheless, an organic particle mask should be worn when spinning. This also provides for maximum dramatic effect, as the combination of clean room bunny suit and organic particle mask is reminiscent of creatures present in the Tatouine bar in Star Wars.

At this point the chip is placed on the spinner chuck and the spinner speed set. Then PMMA is spun using the appropriate recipe for Cr-Au gates or ohmic contacts. For Cr-Au gates, a PMMA bilayer is spun. The composition of the two layers is chosen such that after e-beam lithography and developing an undercut in the bilayer will result. This undercut facilitates liftoff after metal deposition. The recipe for Cr-Au gates is as follows:

1) One layer of 2% 496K PMMA. One drop is placed on the chip, which is immediately spun at 4000 rpm for 1 minute, then placed on a hotplate and baked for 15 minutes at 180°.
2) One layer of 2% 950K PMMA. For this layer, the spinner control should be in two-speed mode. One drop is placed on the chip *while* it is rotating slowly at 50 rpm; then the spinner should accelerate to 4000 rpm and spin for one minute. The drop is applied in this manner to prevent the second layer from

dissolving the first. The sample is then baked for 15 minutes at 180°.

For ohmic contacts, a PMMA trilayer is spun. The trilayer design also results in an undercut, but contains an additional layer as a precaution against pinholes in the PMMA [Eriksson, 1997]. The recipe for ohmics is as follows:

1) One layer of 2% 496K PMMA. One drop is placed on the chip, which is immediately spun at 4000 rpm for 1 minute, then placed on the hotplate and baked for 15 minutes at 180°.
2) A second layer of 2% 496K PMMA, deposited and treated as in step 1)
3) One layer of 2% 950K PMMA, spun at 4000 rpm for one minute and baked for 15 minutes at 180°.

3.3.3 Electron Beam Lithography

At this stage, the chips are ready for electron beam writing. In this step, portions of the PMMA layer are exposed to a beam of electrons which sweeps across the surface in the desired pattern. The electron beam provides energy to break chemical bonds in the PMMA, rendering it soluble in a developing solution. The devices described in the thesis were all written using the JEOL 6400 scanning electron microscope (SEM) in the Gordon McKay building. The electron beam is controlled by computer software which determines the beam position and beam blanking to selectively expose the PMMA. The PMMA is exposed as a series of closely spaced dots, and the dose is determined by controlling the dot spacing and exposure time.

The controlling software is called the Nanometer Pattern Generation System (NPGS), designed by Nabity Lithography Systems. It requires two types of input files. The first is a DesignCAD file containing the two-dimensional pattern to be written.

DesignCAD is a computer-assisted design program which enables the user to draw two-dimensional structures in a series of "layers," each of which can be assigned a common set of properties. The second file input to the NPGS software is a "runfile," which contains information about the desired dot spacing, the electron beam current, and the desired dosage for each layer. The program uses this information to determine the necessary beam dwell time for each dot.

Here I describe the sequence of steps which I use for e-beam lithography. Other perspectives can be found in previous Westervelt theses [Katine, 1996; Adourian, 1996; Crouch, 1996; Livermore, 1997].

1) The chip is affixed to an aluminum sample mount using one drop of carbon paint at each side, applied in quick succession. (Brass mounts are available but should not be used as the copper in the brass can easily diffuse in the GaAs, resulting in unwanted impurities). It is critical to mount the chip flat on the sample mount to facilitate focusing on the surface.
2) For Cr-Au gate writing, silver paint is deposited on the surface for focusing. Apply a drop of silver paint to a piece of filter paper and let it dry. Then, dip a fine-tipped wooden applicator in the paint and tap lightly on the sample surface while observing through a low power magnifying lens. The aim is to achieve a dusting of very fine silver paint specks on each end of the chip, without obliterating too much of the PMMA layer in the process or contaminating regions of the chip where fine features will be written.
3) Place the sample mount in the SEM chuck, and tighten the fastening screw very gently; if it is overtightened, the sample mount will tilt and the chip will be loaded in the SEM at an angle. Load the assembly in the vaccuum chamber and adjust the working distance to 15.
4) Set the SEM in linescan and SEM1 mode, and load the initial beam conditions using the screen menus. For writing, these conditions are an acceleration

voltage of 35 keV and a working distance of 15. The brightness on the two monitors should be turned up all the way, resulting in a white horizontal line across across the lefthand screen, corresponding to linescan mode.

5) Move the sample out of the beam path and turn on the electron beam by pressing the "accel" button. The filament current is then raised slowly to the saturation point, which is the second current maximum; the current level can be viewed by observing the screen linescan signal.
6) Adjust the tilt and shift to maximize the beam current. These should be adjusted again after 20 minutes as they drift after the beam is turned on, and the beam currents must stabilize before writing; small drifts in the current can result in dramatic differences in e-beam dosages.
7) Focus on the surface of the sample. Focus on at least two specks of silver paint at each end, and average the results to approximate the necessary focus for the chip center. If the values at each end differ by more than 100 (in unknown units), you may want to remount the sample; less than 50 is acceptable.
8) Measure the beam currents to be used, which are determined by the parameters entered in the runfile for each layer. The current is controlled by changing the condenser lens between each layer. Because currents can drift from one writing session to the next, they must be remeasured each time immediately before writing. The current is measured by pressing the "PCD" button, which inserts a Faraday cup in the path of the electron beam. The condenser lens should be cycled through each desired setting, and measured values entered in the runfile.
9) Transfer control of the SEM to the computer via the computer control switch and turn on the beam blanking. Move the sample into position beneath the (blanked) beam. Enter the measured focus and set the first condenser lens value. Begin writing by typing "pg filename.dc2." ("Pg" is the main NPGS program and stands for "pattern generation"; ".dc2" defines the file as a

DesignCAD file, rather than a ".rf6," or runfile). The program pauses between each layer to enable the user to set the appropriate condenser lens value.

10) After writing and removing the sample, the exposed PMMA is developed away. The developer solution is composed of isopropyl alcohol (IPA) and methyl-isobutyl ketone (MIBK) in a 3:1 volume ratio with 1.3% (by weight) methyl ethyl ketone (MEK). Immerse the sample in the developer in the fume hood for one minute. Immediately quench the developing process in pure IPA and dry the sample with high-purity nitrogen gas.

11) If evaporation is to follow immediately, the sample should be immersed in an NH_3OH solution (5:1 water:NH_3OH by volume) for a few seconds and then immediately dried. This removes any oxide layer or contaminants that may be on the exposed surface of the sample, thereby facilitating better metal adhesion. Without this step, wirebonding to contact pads may be difficult. An unwanted side effect of NH_3OH immersion is carbon paint debris lodged in the PMMA trenches on the sample, usually at the finest feature scale. If these particles are not removed, they can result in breaks in the metal gates after liftoff. Immersion in isopropyl alcohol with ultrasound will dislodge these particles. The sample should be examined under the optical microscope to ensure all such particles are removed.

3.3.4 Metallization

At this stage, a negative resist mask in the shape of the desired device has been formed on the heterostructure surface. The next step is the evaporation of metals into the resist trenches in order to form gates. Evaporation of metals to form ohmic contacts and gates is carried out in two thermal evaporators located in the outer clean room. For both processes, the procedure is similar. The source metals are placed in metal boats in the evaporator vaccuum chamber; the sample is placed above the boats. High electric currents are passed through the boats which evaporate the source metals onto the sample. The amount of metal evaporated is monitored using a crystal thickness monitor placed adjacent to the sample.

For ohmic contacts, Au, Ni, and Ge are evaporated in several layers, and then annealed in order to contact the 2DEG. The mechanism whereby contact is made is not clearly understood, but it is thought that Ge tendrils extend to the 2DEG during the annealing step [Braslau, 1981; Taylor *et al.*, 1994]. The sample is first mounted on a dedicated ohmic contact evaporation stage using carbon paint and dedicated ohmic evaporation arms are bolted in the evaporator. These dedicated components should be used for ohmic contacts, as Ge can adversely affect the samples of other groups. Each metal should be placed in an appropriate boat. For Au and Ge, the thin tungsten boats can be used. For Ni, it is necessary to use the thicker boats, as Ni has a higher melting point and requires larger currents. When mounting the evaporation arms, do not over-tighten the fastening bolts, or the source metals will vibrate out of the boats due to the bad vibrations of the vacuum pump. Before closing the chamber, tear a small hole in the aluminum foil which lines the inner walls of the chamber to facilitate viewing of the boats during evaporation.

After rough pumping out the chamber, heat each boat in succession to melt the source metals. This prevents them from vibrating out of the boats during the two hour pumpdown and ensures that sufficient contact has been made to enable evaporation. The Ni boat should be heated *very* slowly, as very high currents are required to melt the Ni. Raising the current too fast can destroy the boat and necessitate reloading. After the pre-melting, the chamber is pumped out to a pressure of 2×10^{-7} Torr. The metals are evaporated according to the following recipe: 50 Å Ni, 50 Å Au, 250 Å Ge, 100 Å Au, 100 Å Ni, 400 Å Au. The density setting on the crystal thickness monitor controller should be set appropriately before evaporating each metal.

For ohmics, the next step is to anneal the samples, which takes place on a strip heater originally constructed by Alex Rimberg [Rimberg, 1992]. The procedure for this is described in several theses [Katine, 1996; Adourian, 1996; Livermore, 1998]. It is essential that the sample be mounted flat on the strip heater, or some ohmics will be insufficiently annealed. A forming gas of 20% H_2 and 80% He flows through the strip heater chamber at 3 psi when annealing; a thermocouple affixed to the strip heater monitors the temperature. My recipe for baking ohmics is slightly more aggressive than that outlined in the above theses, and consists of one minute at 110° C, 20 seconds at 260° C, and 40 seconds at 410 ° C. After removing the sample from the strip heater, the contacts should have a "pizza cheese" appearance when viewed under the optical microscope. If this is not the case for all of the contacts, they should be re-annealed.

To evaporate Cr/Au gates, the procedure is very similar. It is not necessary to mount evaporation arms in the dedicated Cr/Au evaporator, as they reside there permanently. The recipe for our quantum dot devices is as follows: 50 Å Cr, followed by 400 Å Au. The Cr is deposited because it adheres to the GaAs surface much more strongly than Au, and the Au adheres well to the Cr. The Cr layer also prevents Au from diffusing in to the GaAs. For Cr/Au gates, baking is not necessary or desirable.

After evaporation, the samples are immersed in acetone for at least two hours in order to liftoff the undesired metal. It is often convenient to immerse the sample in acetone overnight. Acetone dissolves the PMMA remaining on the surface and thus removes the metal evaporated on it. However, some of this metal may adhere to the gates deposited on the heterostructure surface. For this reason, gentle ultrasounding is sometimes necessary, although merely spraying the sample with acetone often provides enough force to remove the unwanted metal.

Figure 3.3 (a) shows an example of a completed sample. The smallest features which I routinely achieved with our electron beam lithography system were on the order of 100 nm. However, by using the line drawing mode in the NPGS software, features of 50 to 75 nm were achieved. The Tinkham group has fabricated samples with 30 nm

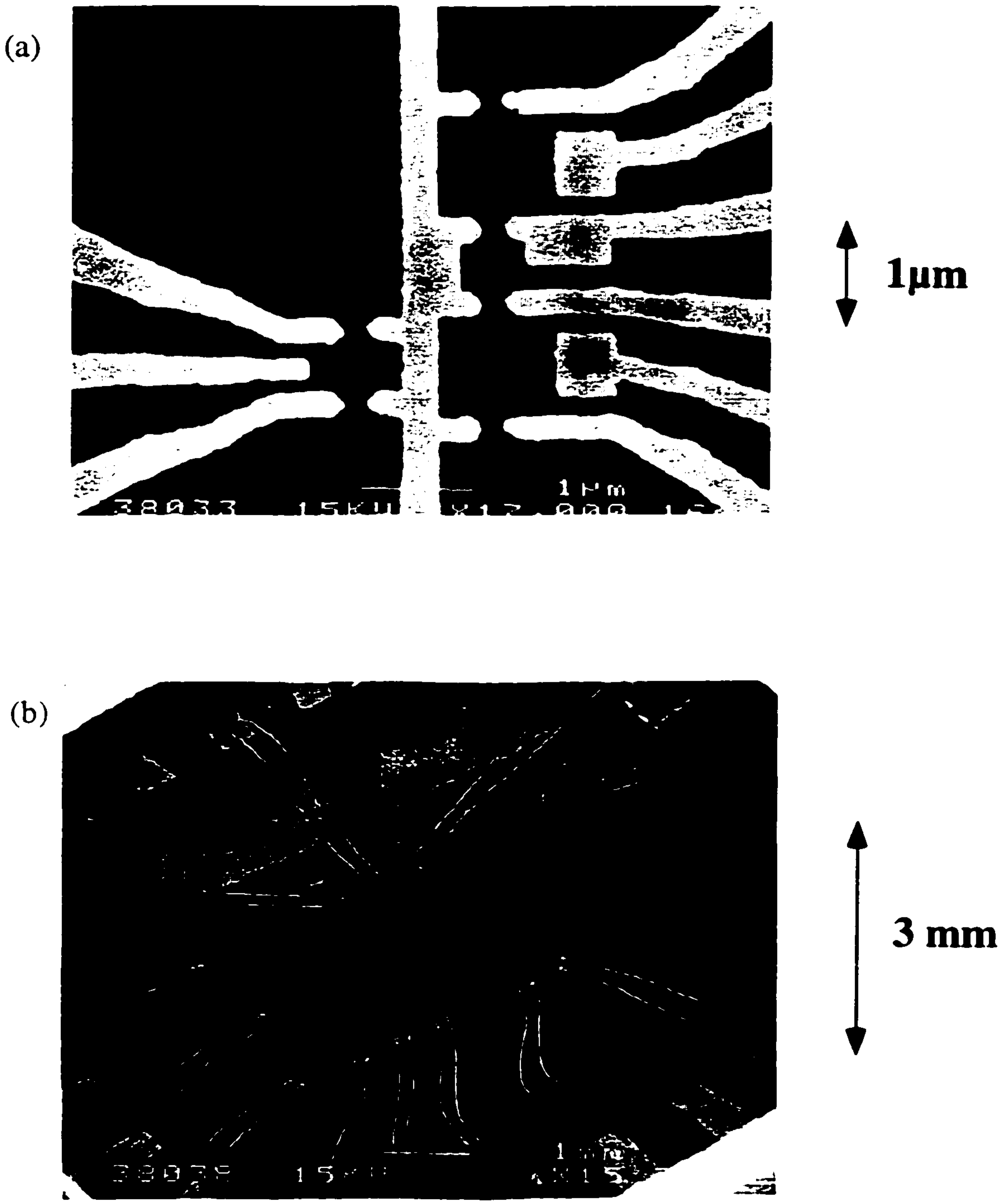

Figure 3.3 Example of completed device. (a) Scanning electron microscope photograph of a single electron trap device, consisting of four quantum dots. (b) Zoomed out view of the same device, showing wirebonds made to contact pads on the chip surface. The pads extend to the center of the chip where the quantum dots are located. Multiple bonds are made to each pad in case of accidental breaks.

linewidths.

Once gates have been evaporated, the last step before wirebonding is to mount the chip in a chip carrier. Chip carriers will be plugged in to the mounting sockets in the cryostats in order to conduct measurements. The best way to affix the sample to a chip carrier is with a small dab of GE varnish. GE varnish, like so many other chemicals we use, is carcinogenic and should only be used in the fume hood. The GE varnish should be allowed 24 hours to dry. If the chip needs to be removed, soaking the chip/chip carrier in acetone will dissolve the GE varnish.

3.3.5 Wirebonding

Wirebonding is the last step in preparing a sample for measurement, and one that unfailingly inspires despair in the novice grad student (or even postdoc). The purpose of this step is to affix gold wires from the contact pads on the chip surface to the pads on the chip carrier. The wirebonder allows the user to precisely position the end of a gold wire over the sample and then contact the sample, at which point a combination of heat and ultrasonic vibration melds the wire with the contact pad. Sounds simple enough. However, there are many failure mechanisms in this process, and, as several days of processing have already been completed and measurements are moments away, the stakes are high. Following is a list of helpful tips for the novice wirebonder:

1) Before wirebonding, be absolutely certain that you understand the grounding paths and interconnections of all metallic wirebonder components. Samples can easily be destroyed at this stage by electrostatic discharge since they are handled more often and an electrical path to the fragile quantum dot gates becomes accessible. Before bonding, ensure the wirebonding head is at the same potential as the sample chip carrier, and that both of these are connected to ground. Because the bonding head contacts and is disconnected from the metal gates, it is crucial that they be at the same potential. The stage on which the chip carrier is set may *appear* to be grounded

because of an attached alligator clip, but it often is NOT, so this should be remedied. A grounding strap should be worn at all times.

2) If threading the wirebonder seems impossible, enlist someone to hold a dentist's mirror (located in the wirebonder accessories cabinet) behind the wirebonder head so you can see what you are doing. Once you have successfully threaded it a few times it becomes very easy. A pair of mint-condition tweezers for this step is essential for successful threading.
3) Use a consistent set of wirebonding parameters. Other users reset these parameters so check them before use. I used a power setting of 1.7, a force setting of 7, a time setting of 8, and a stage heat setting of 80° C. Often, wires do not stick to the metal bonding pads but rather tear off pieces of the metal. If the NH_3OH immersion step was omitted before evaporation, you may be out of luck. However, slight variations in the wirebonding parameters are often the solution. In particular, try reducing the heat and increasing the power.
4) Wirebonds do not last forever, but can break as a function of time or abuse. This often happens when the samples are thermally cycled and is not discovered until the sample is at base temperature in the fridge. Therefore, I bond two to three wires to each pad to provide enough redundancy that the occasional break won't matter. The resulting structure is depicted in Fig. 3.3 (b).

3.3.6 General Sample Handling Procedures

As mentioned in the section on wirebonding, finished samples are very fragile. Besides the obvious vulnerability of chips to breaking, the nanostructures themselves are extremely sensitive to electrostatic discharge. Mishandling them can result in a micro-explosion of sufficient power to completely obliterate your painstakingly crafted quantum dots. Therefore, precautions must be taken. Try to minimize the number of times you pick up and handle a sample. Always ground yourself before picking up a sample.

Before loading and unloading a sample in the fridge or wirebonder, thoroughly understand the path to ground of the metallic components involved, as well as the interconnections. Wear grounding straps to ensure you are at the same potential as both the sample and the socket. If samples are to be saved long-term, store them in the nitrogen box in the outer clean room to prevent degradation in air.

3.4 Cryogenic Techniques

All of the measurements described in this thesis were done at low temperatures, ranging from 4.2 K obtainable in liquid helium storage dewars to 10 mK in our Kelvinox 400 dilution refrigerator. For an overview of low temperature techniques, consult Lounasmaa [1974]. Simple immersion in liquid He is suitable for quick tests of point contacts and quantum dot components, but most measurements on quantum dots require dilution refrigerator temperatures. Although a good dilution refrigerator can obtain temperatures down to 10 mK and even lower, the poor electron-phonon coupling at low temperatures results in electron temperatures in our devices ~ 100 mK. However, this is sufficient for observing Coulomb blockade and quantized level spacing effects in our dots.

General safety note: Cryogens are extremely dangerous materals. They can seriously injure and/or kill you and those around you. They can cause severe burns if they come into contact with the skin. Even more ominous, extremely high pressures can quickly build up in closed containers and cryogenic liquids can evaporate violently when exposed to warmer temperatures. If dewars containing cryogens are left open to the air for even a short time, solid air can form over the cryogenic liquid, resulting in what is effectively a time bomb, as there is no pressure release. It is possible, through daily dealings with such materials, to develop an easy familiarity with cryogens resulting in a blasé attitude and lack of respect for their danger. I have witnessed many examples of carelessness in handling cryogens that could have had disastrous consequences. Don't let this happen to you. You will be endangering your own life and the lives of those around you. It is not necessary to live in fear of liquid helium, but a strong respect for its potential hazards is a must.

3.4.1 Dilution refrigerators

Most of the measurements described in this thesis were carried out using dilution refrigerators. The principle of operation of a dilution refrigerator is described in detail in various texts, in particular Lounasmaa [1974]. In short, when liquid He3 is immersed in liquid He4 and cooled, the solution separates into two phases: a He3 rich phase floating on top of a He3 poor phase of almost pure He4. The He3 in the dilute phase can be thought of as a He3 "gas" underneath the "liquid" He3 rich phase. If a tube is passed through the upper phase to the lower and pumped on, it upsets the equilibrium of the two isotopes in the lower phase. In order to restore the equilibrium, He3 will cross the phase boundary from the upper to the lower layer and in the process draw heat from its surroundings. A dilution refrigerator is arranged such that the source of heat for this can be a quantum dot.

The Westervelt group has access to two dilution refrigerators, a Kelvinox 100 and a Kelvinox 400. The characteristics and the procedures for cooling them have been documented in Adourian [1996] and Pohlen [1999], respectively. The Kelvinox 400 has a higher cooling power (supposedly 400 μW of cooling power at 100 mK, as opposed to 100 μW for the Kelvinox 100). In addition, the Kelvinox 400 has an automated gas handling system, whereas the Kelvinox 100 has a manual system. In principle, once the sample is in the dewar and at 4 K, the fridge will get to base temperature with the single push of a button. The reality is more complicated than this, and in fact the fridge possesses several quirks which require careful monitoring. Thus the automation of the Kelvinox 400 is a mixed blessing: on the one hand, it does make certain steps in a cooldown easier; on the other hand, it can obscure the sequence of steps from the user, and thus makes the cooldown process less intuitive. For this reason, new users are advised to use the Kelvinox 100. The choice of fridge, as well as the pecularities of the Kelvinox 400, are covered in [Pohlen, 1999].

3.4.2 Electrical Filtering

There are two sources of heat leaks within dilution refrigerators that are the primary determinants of obtainable sample temperatures. These are 1) blackbody radiation from warmer sections of the fridge, for example from the He4 bath; and 2) radiofrequency radiation traveling through the sample leads, which necessarily extend from the room to the sample [Cleland *et al.*, 1992; Martinis and Nahum, 1993]. To shield the sample from the ambient blackbody radiation, the sample is encased in several layers of Faraday boxes, including the inner vacuum can (IVC), the 100 mK shield, and the final enclosure of the sample holder. To shield radiofrequency radiation, more elaborate techniques are required. In particular, RF filters must be inserted in the conduction path of the sample leads. Ian Chan and I manufactured several sets of RF filters for this purpose. Two sets have been installed in the Kelvinox 400; two more sets are available for the Kelvinox 100.

These filters consist of copper boxes filled with copper powder through which the sample leads pass. The copper powder filters attenuate RF noise via the skin effect [Martinis *et al.*, Zorin, 1995; Vion *et al.*, 1995; Huibers, 1998]. The sample leads within the filter boxes are segments of high-resistance wire; the wire is embedded in a mixture of copper powder and stycast. Resistive wire is used to reflect incoming RF signals and to provide a degree of RC filtering; the capacitance of these RC filters is that of the leads, about 20 pF/foot. The wires and copper powder mixture are encased in machined filter boxes, made from gold-plated copper. The shop designs for these boxes are currently located in the Oxford dilution refrigerator manuals.

Several considerations dictate the choice of wire for the filters. The resistive wire we used was manufactured by California Fine Wire Company. Many varieties of wire are available, with varying combinations of metals, insulators, diameters, and resistances. For our filters, we used 0.003 inch diameter Stable-Ohm 800 B twisted pair, an alloy of Cu, Ni, and Mn. Non-magnetic metals are preferrable to minimize stray magnetic fields. Larger diameter wire is much easier to handle and solder, but smaller wire is higher in resistance. The choice of insulator is also key: some insulators are more likely to crack, creating the possibility of wires shorting together. If twisted pair is desired, let the company do it; they do a far better job and it will save you many headaches.

For each pair of leads, we used six feet of twisted pair. Each twisted pair was fashioned into a small coil and placed in the filter box. Two twisted pairs were threaded through each of the six holes on either side of the box, for a total of 24 leads. To provide mechanical stability at these holes, small (0.25") segments of teflon tubing were used to sheath the wires at the entrances of the box. After loading all of the wires in the boxes, the remaining space was filled with a copper powder-Stycast mixture in a 1:1 volume ratio. Stycast must be pumped on to remove air bubbles. Because mixing in the copper powder introduces a large amount of air in the stycast/powder mixture, pumping should be done subsequent to mixing and in a container large enough to prevent the mixture from expanding over the sides.

3.4.3 Lambda Point Refrigerator

The Kelvinox 400 contains a lambda point refrigerator which enables the user to ramp the superconducting magnet to higher magnetic field values than otherwise obtainable. The lambda point refrigerator is simply a metal plate thermally sunk to the top of the superconducting magnet. The plate can be pumped on to evaporatively cool the plate, the liquid helium in the bath immediately above it, and the magnet to ~ 2K. Consequently, more current can be passed through the magnet and higher magnetic fields obtained. Without using the lambda plate, the maximum field is 9 T; with the plate, the maximum field is 11 T. The components for operating the lambda plate were obtained and assembled by me, and the procedure for using the lambda plate has not been documented in a thesis, so I will describe it here. I will include the procedure for operating the new Oxford magnet power supply, as they are interrelated. The Oxford manuals on the lambda fridge and power supply should also be read before use.

The required helium level in the bath is > 40% of the full bath volume if ramping to 9 T, and > 60% if ramping to 11 T. To ramp to a field value ≤ 9 T:

1) The power supply should be set in sweep limiting mode. If this is the case, this indicator light will be lit when you press "go to set." This should be the default mode for the power supply when it is turned on.
2) Put in "slow" mode by pressing "hold" and "lower" (vs. "fast" mode which is attained by pressing "hold" and "raise"). The first time the magnet is run when it is cooled down, it should be ramped up and down in slow mode. After that, during the same cooldown, it can be ramped in fast mode.
3) Set the "point" to ramp to and the ramp rate. The maximum rates allowed in sweep limiting mode are 6 A/min up to a current value of 80 A, and 10 A/min thereafter.
4) Turn on the switch heater by pressing the "heater" button and holding for 5 seconds. Wait for one minute before proceeding to make sure the heater is activated.
5) Press "go to set" to ramp the magnet to the desired value.

If the magnet is to be ramped to 11 T, it should first be ramped up to 9 T following the above procedure, and then:

6) Place the magnet in persistent current mode by switching off the heater. Again, hold the heater button for several seconds, and let the system sit for one minute before proceeding.
7) Ramp the power supply current to zero by pressing "go to zero." You now have about 100 A of current coursing around in the superconducting magnet in the fridge.
8) Open the needle valve to the lambda plate reservoir all the way, and monitor the

temperature of the magnet via the resistor attached to it. At 4.2 K, we measured a resistance of R = 1.04 kΩ; after three hours of pumping, we measured R = 4.1 kΩ.

9) Progressively close the needle valve as the magnet cools down. The objective is to have the minimum amount of gas flow through the line when the fridge is at 2.2 K.
10) When the magnet resistance has reached its maximum value, ramp the current in the power supply back to the current corresponding to 9 T.
11) Turn on the heater, again holding the heater button for several seconds, and pause for one minute. The magnet resistor value will fall again as it heats up, in the case of our run back to a value of 3.62 kΩ.
12) The magnet can now be ramped safely up to 11 T. The magnet resistance should be monitored closely in case there is undue heating. If this occurs, the magnet current should be ramped down to safer levels (< 9 T).

3.5 Electronic Measurement Techniques

In this section, setups for making low-noise measurements on quantum point contacts and quantum dots are described. Most of the measurements described in this thesis were of the differential conductance through a quantum dot, with either zero drain-source bias (linear conductance) or finite-bias (nonlinear conductance). I will also describe the methods for making magnetic field measurements on our dots.

3.5.1 Low-noise Measurements on Quantum Dots

Currents involved in quantum dot measurements are on the order of a few nA, and therefore low-noise techniques are essential. In the Westervelt lab, the most common technique is to use a lock-in amplifier to amplify these low signals above the noise level. The principle behind the lock-in amplifier is explained in chapter 10 of Horowitz and Hill [1989]. The setup for my measurements is depicted in Fig. 3.4. In this steup, a 10 μV ac signal is placed across the quantum point contact or quantum dot, usually a divided down

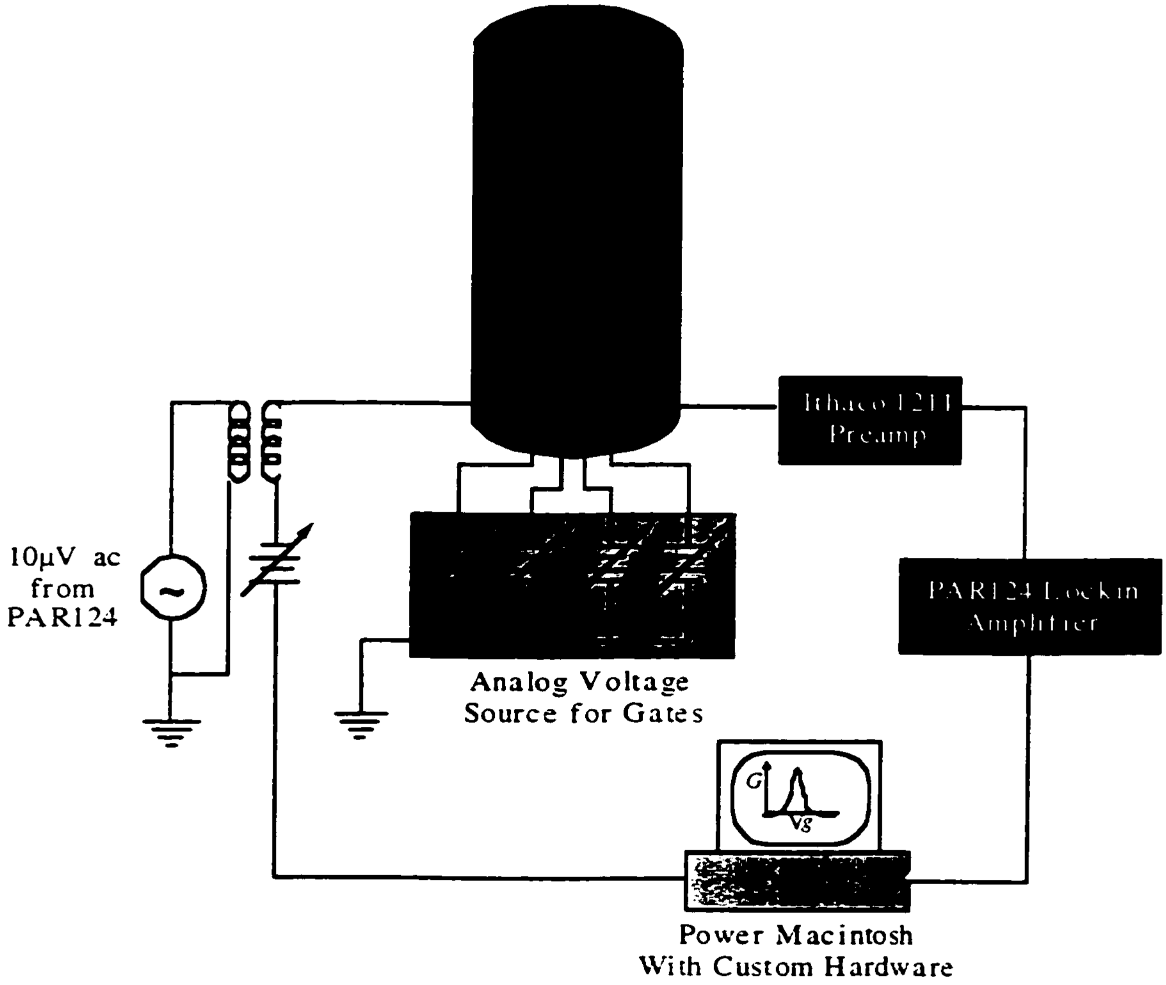

Figure 3.4 Low noise measurement circuit for quantum point contacts and quantum dots. An AC voltage is placed across the device, and measured with a lockin amplifier. Fixed voltages are placed on the device gates using an analog voltage source. Figure adapted from Waugh [1994].

signal drawn from the signal generator in the PAR 124 lockin. The size of this voltage is chosen so that eV $<<$ $e^2/2C$ (hence the name "zero-bias.") The resulting current through the sample is amplified by an Ithaco 1211 current amplifier. The output of the Ithaco is fed back in to the lockin, where it is amplified by a PAR 117 amplifier and filtered by the lockin. The output of the lockin signal can then be read by a computer. In a typical measurement, the conductance is measured while some other parameter, such as sidegate voltage or magnetic field, is varied.

For nonlinear measurements, the setup is similar and is also shown in Fig. 3.4. The principal difference is that the 10 μV ac signal is added to a variable dc voltage placed across the dot. This dc voltage allows us to probe the excited states of a quantum dot. The differential conductance through the dot is again measured by amplifying and measuring the small ac current resulting from the small ac voltage, but at a finite-bias. The transformer couples the ac signal to the dc bias, which is usually provided by a computer digital-to-analog card.

Voltages placed on the metal gates forming the dot are controlled by an electrostatic gate voltage box. The circuit design for these boxes is described in Katine [1996]. These boxes possess up to seven fixed voltage outputs, which can be manually varied, and one ramped voltage output, which can be set to ramp automatically at a given rate. For relatively short measurements, such as tuning a quantum dot (characterizing quantum point contacts and locating the Coulomb blockade regime), this ramp output is sufficiently fast. However, for 2-dimensional scans and more time-critical measurements, a computer-controlled ramped output is preferable. Resistor-capacitor (RC) low-pass filters (typically 10 Hz) were placed on all cables emanating from these battery boxes and from the lockin and computer to filter out ambient high-frequency noise.

There are several choices for measurement software. The Labview VI "Read N DMMs" uses a GPIB connection to read the voltage values simultaneously on up to three Fluke or HP multimeters at intervals specified by the user [Mar, 1994]. This setup is very simple and is recommended for tuning quantum dots. However, it is too slow for elaborate measurements such as two-dimensional scans, and does not provide a great deal of control over data processing. For two-dimensional scans, I used one of two setups. The "fast-data-taker" setup and Labview VI, designed and constructed by Carol Livermore and described in Livermore [1997] worked very well for this purpose, and was used to obtain the data in chapters 4 and 5. For the double dot measurements described in chapter 6, I used a program written by Mark Topinka originally for his AFM experiments. Because the program outputs two voltages to control the x and y sweeps of an AFM and reads in three channels, we adapted it for double dot conductance measurements. The principal advantages of this program are its easy user interface and the capability to view 2D data in real time.

The first step in studying quantum dots is to find a good operating regime for Coulomb blockade measurements; this is referred to as "tuning" a quantum dot. Because our tunnel junctions are quantum point contacts, we can continuously vary their conductance. This additional control necessitates preliminary measurements to find a tunnel conductance regime where Coulomb blockade effects can be observed. This is complicated by the cross-capacitance which exists between metal gates. For example, changing the voltage on a dot sidegate will also change the conductance through the dot point contacts due to the capacitance between the sidegate and the point contact channel.

To deal with this problem, we have developed an algorithm for dot tuning, illustrated in Fig. 3.5. The first step is to measure the conductance through a point contact G_{qpc} as a function of the voltage on the point contact gate V_{qpc}, as in the solid trace of Fig. 3.5. Then, voltages V_g are placed on both of the dot sidegates in the regime at which the dot will be operated, typically ~ -0.4 V. The conductance G_{qpc} is again measured as a function of V_{qpc}. Because of the cross capacitance between the sidegates and the point contact, the point contact trace will be shifted to slightly higher voltage values, as in the dashed trace of Fig. 3.5. Similar measurements can be made at several different values of

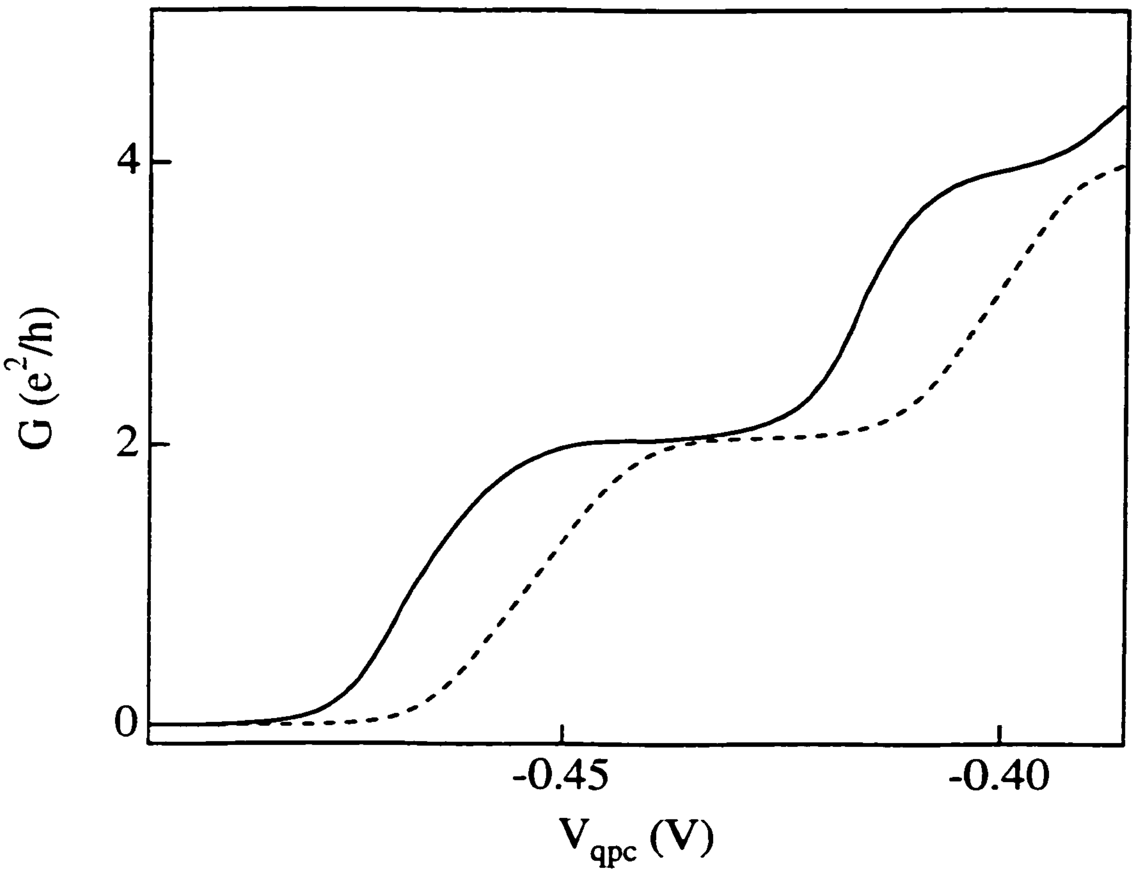

Figure 3.5 Data illustrating cross-capacitance between point contact gate and dot sidegate. Solid trace is the measured differential conductance G through a quantum point contact vs. point contact voltage V_{qpc}; the last two conductance plateaus are visible. Dashed trace was taken with dot sidegates energized to –350 mV. The point contact trace shifts due to the sidegate's effect on its conductance. Such shifts must be measured when tuning a quantum dot to the Coulomb blockade regime.

V_g to determine the effect of V_g on G_{qpc}. This procedure is also used to determine the sensitivity of G_{qpc1} for one point contact to the voltage on the other point contact V_{qpc2}. In this case, G_{qpc1} can not be measured when the other contact is tuned in the operating regime (typically $G_{qpc} \approx 0.2G_Q$). However, G_{qpc1} can be measured at several values of V_{qpc2}, from which the effect on G_{qpc1} of V_{qpc2} in the operating regime can be extrapolated. Once these dependencies are understood, the contacts are both set in the operating regime and the dot sidegates are energized, forming the complete dot. The conductance through the dot is then measured as V_g is ramped down further to study Coulomb blockade peaks.

Many of the Coulomb blockade spectroscopy measurements described in this thesis were made as a function of magnetic field. Each of our dilution refrigerators is equipped with a superconducting solenoid magnet. There are two power supplies available for powering them. The old Oxford power supply is neither bipolar nor computer controllable. To make measurements as a function of changing magnetic field, the field must therefore be ramped very slowly as other system parameters are varied. The magnetic field is monitored by measuring the voltage across a 0.097 Ω power resistor placed in series with the power supply. The new Oxford IPS120-10 power supply allows much more flexibility. It is bipolar, outputs +/-120 A, and can be computer controlled via GPIB or RS232 connections. The output current can also be monitored by computer via a voltage output on the back of the supply expressly for this purpose.

3.6 Conclusion

In this chapter, techniques used for fabricating and making measurements on semiconductor nanostructures were described. These techniques were used to carry out the experiments described in the remainder of this thesis. Additional measurement methods were used in certain experiments, and will be described in the corresponding chapters.

Chapter 4

Charge Quantization in a Single-Electron Box

4.1 Introduction

This chapter presents experiments which study the breakdown of charge quantization in a quantum dot functioning as a single-electron box. This process is studied in the most direct way by measuring the charge in the box with an external electrometer. The quantization of the electron charge plays a fundamental role in the behavior of quantum dots. For a dot weakly coupled to its environment ($G << G_Q = 2e^2/h$) the number of electrons in the dot is a well-defined integer, and the electron wavefunctions leak minimally across the tunnel junctions coupling the dot to its leads. In the opposite limit of strong coupling, the charge in the dot can vary continously. This is similar to the continuous variation of charge on a capacitor plate, which is possible despite the fundamentally discrete nature of the electronic charge. Between these two limits lies a regime in which the quantization of dot charge is progressively destroyed by quantum fluctuations. This behaviour is illustrated in Fig. 4.1, adapted from Matveev [1995]. This graph plots the charge in a dot vs. the charge induced on the dot by a capacitively coupled gate electrode, for a range of values of the dot-to-lead coupling g, where g is in units of G_Q. For $g \approx 0$, the number of electrons on the dot changes periodically in sharp, vertical steps at gate voltages corresponding to the points of energy degeneracy at which Coulomb blockade conductance peaks occur in transport measurements. If the tunnel-coupling of the dot to the lead is raised, quantum fluctuations of the dot charge start to smear the steps and the

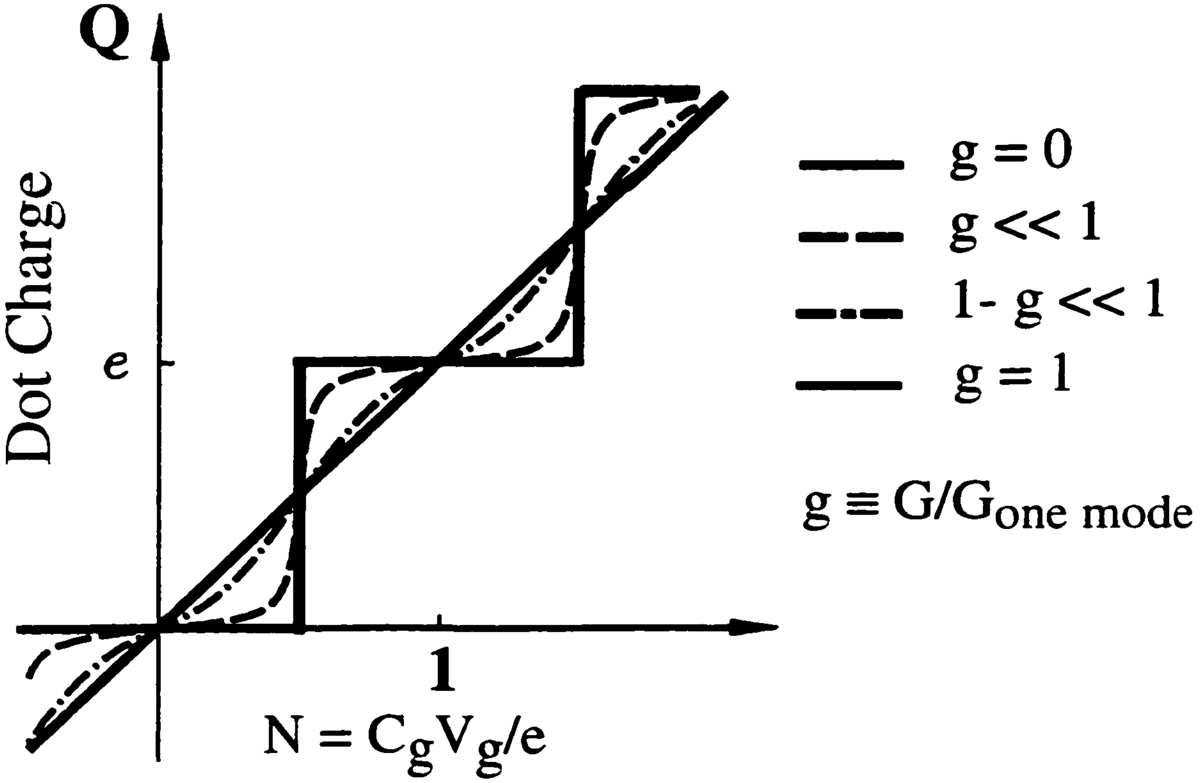

Figure 4.1 Charge on a quantum dot Q as a function of the number of electrons induced on the quantum dot N and the normalized conductance g of the dot-to-lead conductance. N is proportional to the voltage on a capacitively coupled gate electrode. For g = 0, electrons are added stepwise. As g is increased steps are smeared due to quantum fluctuations of the dot charge. For g = 1, dot charge increases linearly with N as for a classical capacitor.

number of electrons on the dot is no longer a good quantum number. This is depicted in the dashed lines in Fig. 4.1 for the intermediate regimes $g << 1$ and $1 - g << 1$. At $g = 1$ the dot is sufficiently open to its environment that the dot charge varies linearly with gate voltage, as on a capacitor plate.

The conditions under which charge quantization is manifested in nanostructures have been studied experimentally in both metal and semiconductor systems, primarily in two types of devices: quantum dots and single-electron boxes. In semiconductor dots, charging effects were first studied indirectly via transport measurements on single and double quantum dots. In single dot experiments, the predominant manifestation of charge quantization is the appearance of Coulomb blockade peaks in transport measurements; these peaks were shown to disappear as the tunnel conductance of the dot to a lead G was raised above G_Q [Kouwenhoven *et al.*, 1991a]. Similarly, two coupled quantum dots were shown to merge into one dot as the tunnel-coupling between them was raised to a value of G_Q [Waugh *et al.*, 1995; Livermore *et al.*, 1996; Crouch *et al.*, 1997]. This transition corresponds to the breakdown of charge quantization on the individual dots, while the charge on the combined double dot structure remains quantized. Other recent experiments have used external electrometers to study charging effects. One such experiment measured the charging energy of a dot using a second dot as an electrometer; the charging energy was shown to scale as a power law at a few values of low $G < G_Q$ [Molenkamp *et al.*, 1995]. Concurrently with the work described in this chapter, a metal single-electron transistor (SET) electrometer was fabricated adjacent to a semiconductor quantum dot and used to measure capacitance between the dot and a nearby metal gate as G was varied [Berman *et al.*, 1997; Berman *et al.*, 1999]. This experiment also found what appeared to be a complete breakdown of charge quantization on the dot at a value $G = G_Q$.

In metal systems, charge quantization has been studied in the single-electron box system. A single-electron box is a quantum dot connected to only a single lead; thus, transport measurements are not possible. Consequently, the study of charging effects in boxes requires an external measurement device, typically an SET electrometer. Such a setup has been realized in several "single-electronic" devices, including the single-electron pump [Martinis and Nahum, 1994], the single-electron turnstile [Geerligs *et al.*, 1990; Kouwenhoven *et al.*, 1991b], the single-electron trap [Dresselhaus *et al.*, 1994; Lukens *et al.*, 1994], and the single-electron box [Lafarge *et al.*, 1991; Devoret *et al.*, 1992]. The latter system, fabricated with aluminum islands and aluminum oxide tunnel junctions, is similar in design to the device described in this chapter. However, there are two key differences: 1) the tunnel conductance of the tunnel junctions is fixed during the fabrication process, and can not be tuned *in situ*, making it impossible to study charge quantization as a function of island-to-lead conductance on one device, and 2) the conductance through the tunnel junctions in metal systems occurs via many weakly transmitting channels, whereas in the semiconductor systems only a single one-dimensional channel contributes. Because of 1), only the effects of thermal fluctuations on charge quantization in a single-electron box were studied [Lafarge *et al.*, 1991]. However, thermal fluctuations alone were not sufficient to explain the breakdown of charge quantization at the lowest temperatures, indicating that quantum fluctuations of charge begin to dominate the device behaviour at these temperatures.

This chapter describes experiments in which the loss of charge quantization by quantum tunneling is studied in the most direct way: by measuring the charge on the dot using a sensitive single-electron transistor (SET) electrometer. We first describe the devices, one quantum dot functioning as an SET electrometer, and a second, capacitively coupled quantum dot functioning as a single-electron box. The electrometer is demonstrated to have sub-single-electron sensitivity and to be superior to conductance measurements for investigating charging effects in quantum dots. We then present data demonstrating the destruction of charge quantization in a single-electron box by tunneling through a single one-dimensional channel with variable tunnel conductance. We find that as the rate of quantum mechanical tunneling from the box to its lead is increased, the quantization of charge is destroyed, disappearing entirely at $G = G_Q$, in agreement with theory. These measurements are the first which examine this effect over the full range of box-to-lead conductance values from $G \cong 0$ to the conductance quantum G_Q. These experiments also illustrate two of the many applications of quantum dots, by presenting two examples of single-electron devices – the SET and the single-electron box.

4.2 Devices and Device Characterization

The devices used for these experiments demonstrate the versatility and applicability of the quantum dot structure. Two quantum dots were used for these measurements; one functions as an SET electrometer, the other as a single-electron box. In order for the electrometer to sense the charge on the box, they had to be fabricated in close proximity to ensure sufficiently strong capacitive coupling. At the same time, it was necessary to pass current independently through each device in order to make measurements on them simultaneously. The combined structure was designed with these constraints in mind. Figure 4.2 shows a scanning electron microscope photograph (a) and a schematic diagram (b) of the structure, consisting of the (SET) electrometer on the left, capacitively coupled to the single-electron box on the right. The devices were defined in a heterostructure containing a 2DEG located 57 nm beneath the surface with sheet density $3.7\times10^{11}/\mathrm{cm}^2$ and a mobility of $5\times10^5\ \mathrm{cm}^2/\mathrm{Vs}$. Only the gates shown and labeled in Fig. 4.2 (b) were used for these experiments. The other gates visible in the SEM micrograph are present for historical reasons, part of an attempt to construct and measure a multi-junction single-electron trap. All of the gates labeled in the schematic are independently tunable. The central gate, labeled V_c in Fig. 4.2 (b), extends across the entire heterostructure chip from top to bottom. When V_c is energized, the chip is separated into two distinct 2DEG regions, one on each half of the center gate. On each of these halves, two ohmic contacts were fabricated, depicted as hatched boxes in

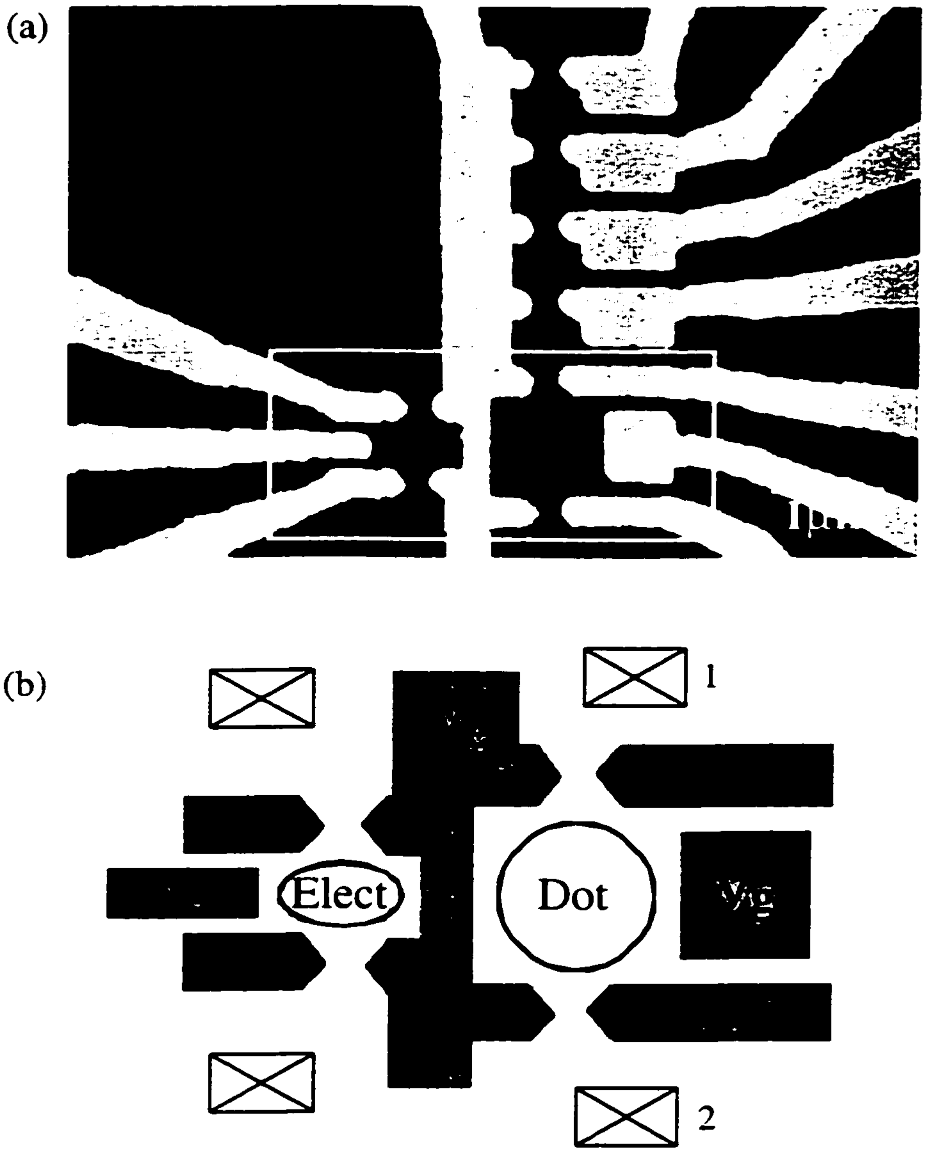

Figure 4.2 (a) Scanning electron microscope photograph of electrometer and single-electron box. Bright areas are metal surface gates; dark area is the GaAs heterostructure surface. Rectangular box encloses gates used for this experiment. Scale bar is 1µm. (b) Wiring schematic of the device, consisting of four quantum point contacts and two confining side walls which act as capacitively coupled gates labeled V_e and V_g. When these gates are energized, the electrometer and box are formed in the two-dimensional electron gas (2DEG) located 57 nm beneath the surface.

Fig. 4.2 (b). Thus, when all gates are energized, it is possible to independently pass current through each of the devices on the chip. All of the measurements described in this chapter were made in a dilution refrigerator at a base temperature of 25 mK.

Figure 4.3 depicts the Coulomb blockade characteristics of each dot. Fig. 4.3 (a) is a plot of the zero-bias differential conductance G_{dot} through the electrometer dot as a function of the voltage on the capacitively coupled sidegate V_e. Periodic Coulomb blockade peaks are evident in this figure. Fig. 4.3 (b) is a similar measurement for the box dot; here the conductance is measured as a function of the gate V_g. The peaks in (a) have a larger period than those in (b) due to the larger size of the box dot and its correspondingly larger capacitance to its sidegate. In the "classical Coulomb blockade" regime, where we can ignore the effects of quantized levels in the dot, the period of Coulomb blockade peaks is simply e/C_g, where C_g is the capacitance of the dot to its sidegate. For the electrometer dot, this capacitance is measured from the spacing of the Coulomb blockade peaks in Fig. 4.3 (a) to be 20 aF; for the box dot, this capacitance is measured to be 80 aF. The background of the peaks in (b) is also much higher, again due to the larger size of this dot with its larger total capacitance C. This results in a lower charging energy barrier e^2/C for electrons to pass through this dot.

4.3 Single-Electron Transistor Electrometer

The Coulomb blockade peak measurements in Fig 4.3 suggest how a quantum dot can function as a single-electron transistor. The two regions of 2DEG comprising the dot leads can be thought of as the source and drain; the sidegate V_e as the gate of the transistor. Clearly the I_{ds} vs. V_e characteristics are highly nonlinear, as can be seen from the presense of the quasi-periodic Coulomb blockade peaks. In contrast to a conventional transistor, the SET turns on and off every time a single electron is added to the dot, i.e. at each Coulomb blockade peak in the conductance. The SET is so named because elec-

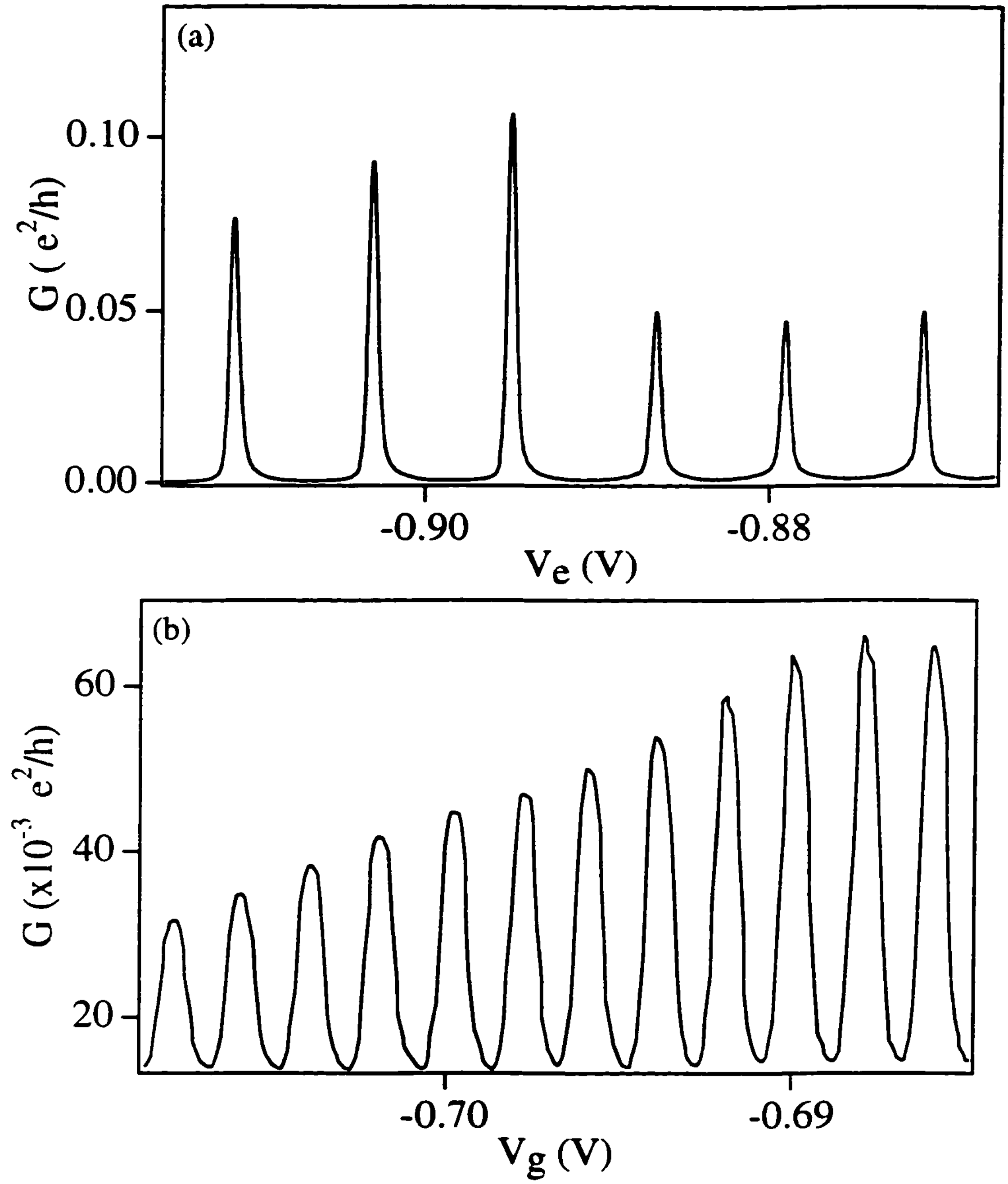

Figure 4.3 Coulomb blockade characteristics of the two dots used in these measurements. (a) Zero-bias differential conductance measured through the left dot, the electrometer dot. (b) Zero-bias differential conductance measured through the right dot, the box dot. In both cases, Coulomb blockade peaks in the conductance are observed. In (b), the peaks have a shorter period and a higher background due to the larger size of the dot.

trons flow through the transistor one at a time due to the Coulomb interaction which prevents, at low bias, more than one electron from entering the dot at a time. An overview of the discovery and research into the properties of SET's can be found in Kastner [1992].

The nonlinearity of the quantum dot I-V characteristics can be exploited to develop a highly sensitive charge detector. This can be seen by considering the relationship between the change in the dot conductance at a Coulomb blockade peak and the corresponding charge induced by the gate electrode V_e. The change in the induced charge over the range of V_e corresponding to the half-width of a Coulomb blockade peak is estimated to be e/12. Thus, a change in the induced charge by this amount is sufficient to cause a full swing in the conductance signal. This signal will also be extremely sensitive to changes of nearby charge. For the SET to function as an electrometer, the conductance through it must first be tuned to the maximally sensitive regime using V_e. The electrometer has a nonlinear response, owing to the nonlinear lineshape of Coulomb blockade peaks. However, at the midpoint of the peaks, the response of the electrometer is approximately linear.

A quantum dot provides an ideal system with which to test the functioning of the electrometer, as we can independently monitor the number of electrons added to the dot via conductance measurements. Fig. 4.4 shows such a measurement using the adjacent quantum dot to test the electrometer's behavior. The upper trace is the zero-bias differential conductance G_{elect} measured through the left, electrometer dot in Fig. 4.1 (b); the lower trace is the zero-bias differential conductance G_{dot} measured simultaneously through the right dot. Both of these measurements are made as the right dot sidegate V_g is swept. The electrometer sidegate V_e was tuned before the sweep such that G_{elect} was at the base of a Coulomb blockade peak. In the lower trace G_{dot}, Coulomb blockade conductance oscillations are observed as V_g is swept. At each peak, the number of electrons on the right dot changes by one. The electrometer has a much weaker capacitive cou-

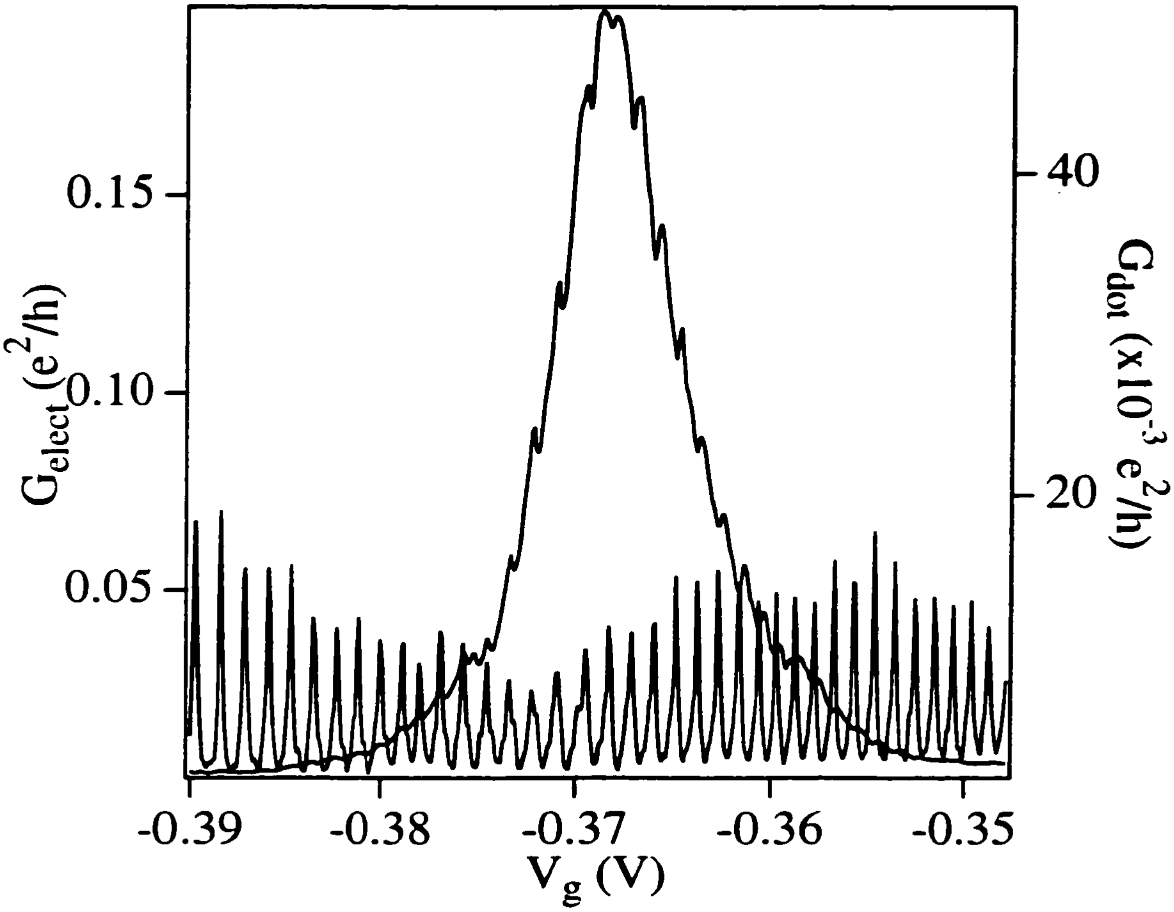

Figure 4.4 Simultaneous measurement of differential conductance in electrometer and box dots as a function of the voltage V_g on the box dot's sidegate. The lower trace shows Coulomb blockade conductance oscillations of the box dot; at each peak the number of electrons on the dot changes by one. The upper trace shows a single Coulomb blockade peak of the electrometer; the much wider peak is due to the much weaker coupling of the electrometer to V_g. Periodic modulations of the electrometer peak align with the Coulomb blockade peaks of the other dot, and are due to the electrometer's response to the single electron changes in the box dot charge.

pling to V_g. Thus, G_{elect} displays one large Coulomb blockade peak in the same span of V_g as for ~ 30 Coulomb blockade peaks in G_{dot}. The interesting feature to note is that the G_{elect} signal has periodic modulations with exactly the same periodicity as the Coulomb Blockade peaks observed in G_{dot}; these modulations are precisely aligned with the peaks. Moreover, the valleys of the modulations align with the G_{dot} peaks on the right, and the peaks of the modulations align with the G_{dot} peaks on the left. These features can be explained by the electrometer's response to single electron changes in the adjacent dot's charge. Each time these single electron changes occur, they partially counteract the effect that ramping V_g has on G_{elect}, resulting in modulations of the evolving electrometer Coulomb blockade peak. Exactly the same electrometer signal is measured as a function of V_g if one of the point contacts of the adjacent dot is completely pinched off so that no current flows through it.

In the data of Fig. 4.4, it is difficult to decouple the effect on the electrometer of single electrons entering the adjacent dot from the effect of ramping V_g, as these influences simultaneously push G_{elect} in different directions. To remedy this, a circuit with a simple feedback mechanism was set up to cancel out the effect of V_g on the electrometer signal. The signal applied to V_g is divided down, inverted, and added to V_e to provide a compensating signal. The divider contains a variable resistor which can be tuned to compensate for the effect of V_g as precisely as possible. When this circuit is properly tuned, the electrometer only responds to the single electron changes in the dot charge.

Figure 4.5 illustrates the effectiveness of this compensation circuit. The solid curves in (a) through (c) are the conductance through the electrometer dot G_{elect}; the dashed curves are the differential conductance through the adjacent dot G_{dot}, measured simultaneously. The cancellation circuit was adjusted to give horizontal plateaus in the electrometer signal at $G \approx 0$, where G is the conductance through the quantum point contact defined by gates V_c and V_{q1} (hereafter labeled qpc_1). The dashed curve in Fig. 4.5 (a) shows a series of Coulomb blockade peaks. At each peak the average charge

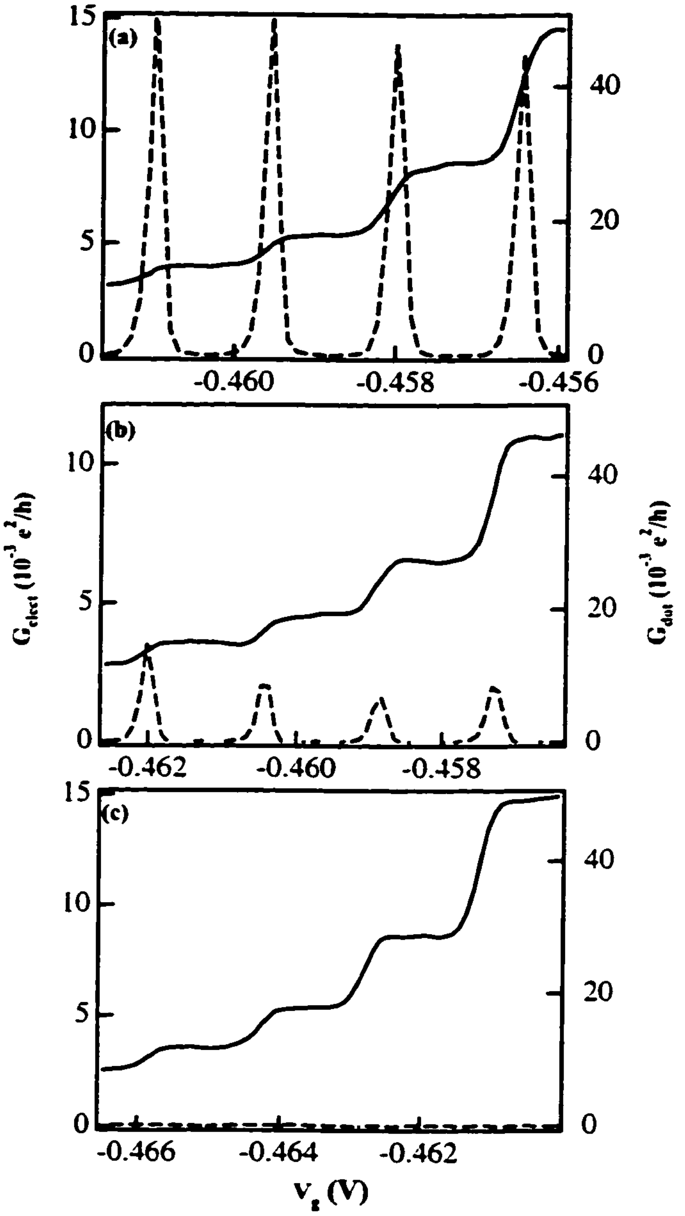

Figure 4.5 Differential conductance G_{elect} (solid curves) of electrometer and G_{dot} (dashed curves) of the dot measured simultaneously vs. gate voltage V_g. The number of electrons on the dot changes by one at each peak in G_{dot} causing G_{elect} to rise in steps. Plateaus in G_{elect} between peaks indicate the dot charge is constant in these regions. In (a) the conductance G of qpc_l is most open ($G = 0.14G_Q$, where $G_Q = 2e^2/h$) resulting in relatively high conductance peaks for the dot. In (b) the point contact is slightly more pinched off ($G = 0.04G_Q$), and in (c) the point contact is completely pinched off with $G \sim 0$; here conductance peaks are no longer perceptible. In all three cases the electrometer signal is equally strong.

on the dot changes by one electron; between peaks, the number of electrons on the dot remains constant. The solid traces in Figs. 4.5 (a) through (c) show clear, stepwise changes in the electrometer conductance G_{elect} corresponding to single electron changes in the charge on the dot. The vertical jumps in G_{elect} align precisely with the G_{dot} conductance peaks. These vertical jumps are in marked contrast to the periodic modulations in the electrometer conductance in Fig. 4.4; here, the electrometer signal is responding only to changes in the charge on the adjacent dot, and not to changes of V_g. The steps are of different heights because of the nonlinear response of the electrometer, i.e. the nonlinear shape of a Coulomb blockade peak.

Figure 4.5 also demonstrates the superiority of electrometer measurements of the dot charge over transport measurements. Each of the dashed traces in Fig. 4.5 (a) to (c) corresponds to progressively lower values of the conductance G through qpc_1. Consequently, the heights of the Coulomb blockade peaks in Fig. 4.5 (a) to (c) become progressively lower. In Fig. 4.5 (c) the transport signal G_{dot} decreases to values below the amplifier noise limit. The electrometer signal G_{elect}, however, remains as strong as before. Thus changes in dot charge in Fig. 4.5 (c) which would be undetectable in conductance measurements on the box dot are clearly evident in the signal from the separate electrometer. It is for this reason that the electrometer is an effective probe of the charge in a single-electron box, on which transport measurements are not possible.

Figure 4.6 is data taken in a similar way, only in this case the contact defined by gates V_c and V_{q2} (qpc_2) was completely pinched off in order to form a single electron box. The x-axis in this case is an ohmic contact coupled to the box, and the y-axis is again the conductance through the electrometer. Again, very clear step changes in the electrometer signal are observed at periodic intervals corresponding to single electrons entering the dot through qpc_1. The sensitivity of the electrometer referenced to the single electron box was found for our device by comparing the noise in G_{elect} with the size of single electron steps, i.e. with the change in electrometer conductance resulting from a single electron

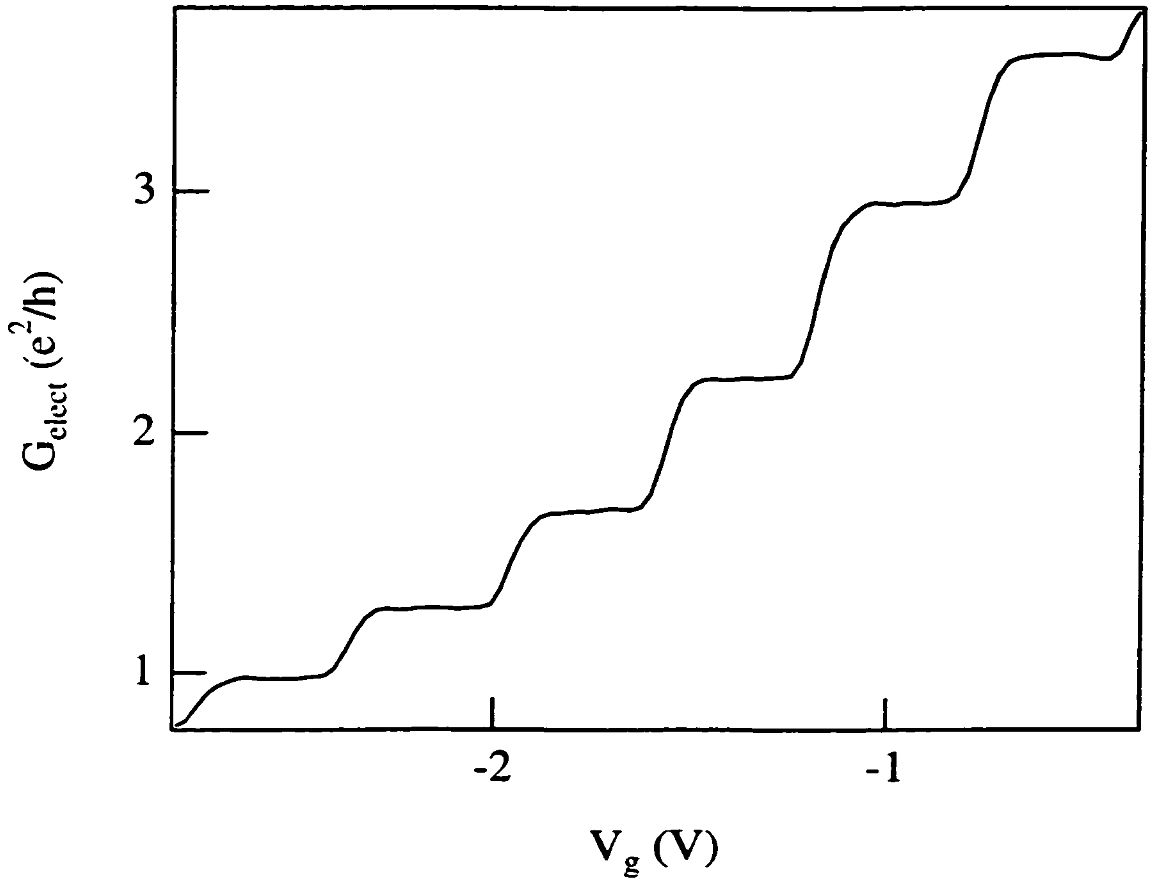

Figure 4.6 Differential conductance G_{elect} of the electrometer dot, measured vs. voltage V_L applied to an ohmic contact coupled to the box dot. For this measurement, the lower dot point contact was completely pinched off to form a single electron box. The electrometer signal shows clear step changes at regular intervals corresponding to single electron changes in the charge in the box. The sensitivity of the electrometer referenced to V_e was measured to be 8×10^{-5} e/Hz. The sensitivity referenced to the charge on the box was measured to be 3×10^{-3} e/$\sqrt{\text{Hz}}$. This gives a coupling efficiency of 2.7%.

change in the charge on the box, giving $\delta q \approx 4 \times 10^{-3}$ e/$\sqrt{\text{Hz}}$. Single electron transistor sensitivities are usually referenced to changes in the charge on the SET gate; for our device, this sensitivity is $\delta q \approx 6 \times 10^{-5}$ e/$\sqrt{\text{Hz}}$, which compares well with previous SET devices [Grabert and Devoret, 1992]. The latter sensitivity is lower than the sensitivity to the charge on the box by a factor of the coupling efficiency, which is therefore ≈ 2.7%.

4.4 Destruction of Charge Quantization

Figure 4.7 shows the direct measurement of the destruction of charge quantization in a single electron box. For these measurements point contact qpc_2 is again completely pinched off by applying a large negative voltage, forming a single-electron box. Electrons enter or leave through a channel defined by the upper point contact qpc_1 Under these circumstances no current flows through the box, but charge can be capacitively induced on the box by applying a voltage V_L to the upper lead.

Figures 4.7 (a) through (f) plot the electrometer signal G_{elect} as a function of V_L for values of tunnel conductance in the upper point contact increasing from $G = 0.08G_Q$ in (a) to $G = 1.04G_Q$ in (f). In Fig. 4.7 (a) clear plateaus in electrometer conductance are observed when the number of electrons on the dot is stable. In Fig. 4.7 (b). the point contact is slightly more open ($G = 0.27\ G_Q$), and the steps are slightly more sloped, indicating that fluctuations in the dot's charge are occurring more frequently as the ohmic contact voltage is swept. This is reminiscent of the behaviour depicted in Fig. 4.1. This trend continues in Fig. 4.7 (c) through (e), as the point contact is progressively more open, the steps become correspondingly more sloped, and the modulations of the electrometer signal progressively less distinct. Finally, at a value of the point contact conductance of $G = G_Q$, the structure in the electrometer has vanished entirely and the dot's charge varies continuously as the ohmic contact voltage is varied. This progression of plots reproduces the basic structure shown in Fig. 4.1.

Theoretical treatments of this system have been made for both metal particles

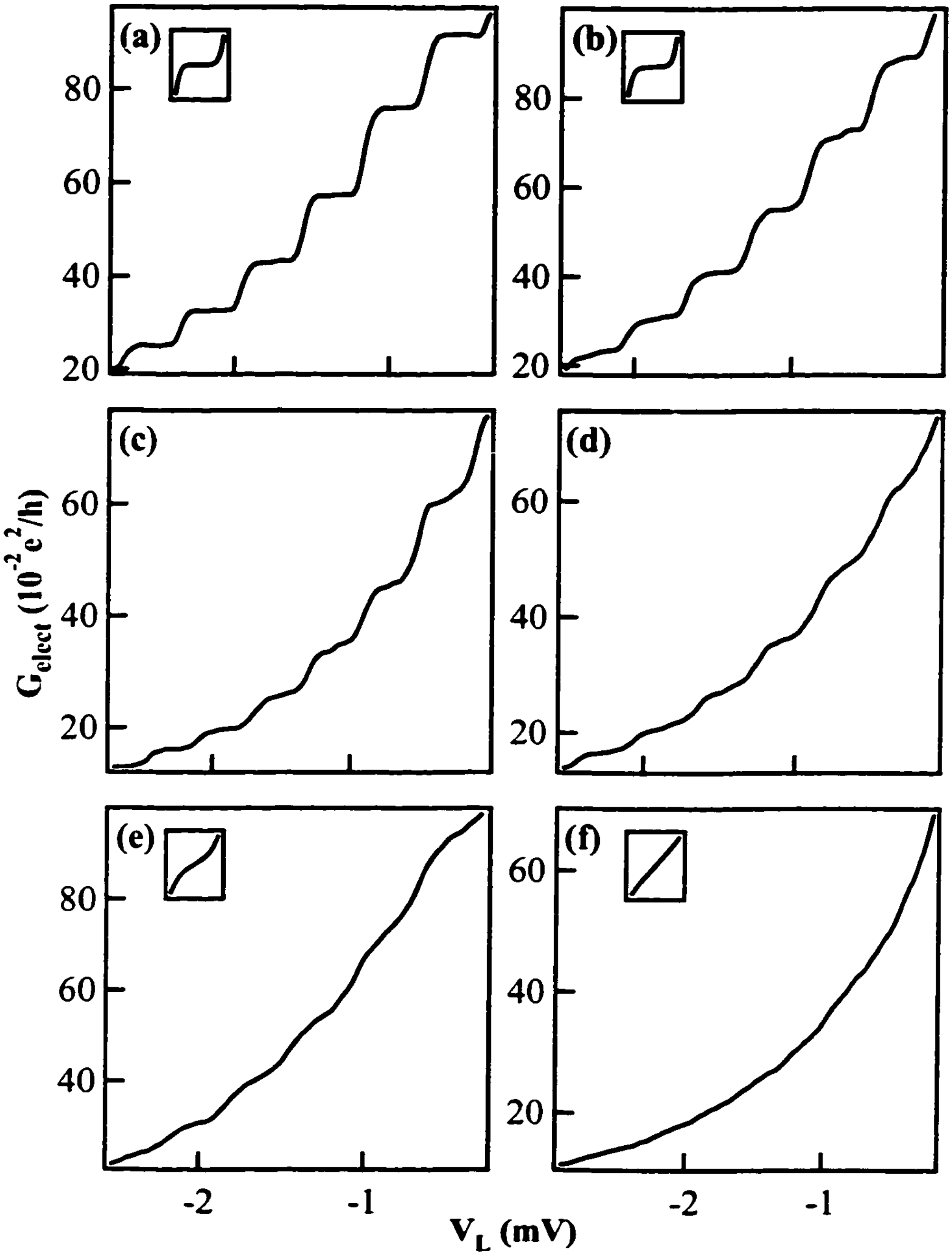

Figure 4.7 Electrometer conductance G_{elect} vs. voltage V_L applied to the upper lead of the box. (a) The single electron steps are nearly horizontal for a weakly tunnel-coupled box with $G = 0.08G_Q$; the steps are progressively smeared in (b) to (e) at conductance values (b) $G = 0.27G_Q$; (c) $G = 0.45G_Q$; (d) $G = 0.66G_Q$; (e) $G = 0.85G_Q$: in (f) the steps are entirely absent at a conductance value of $G = 1.04G_Q$ (where $G_Q = 2e^2/h$). Insets are theoretical calculations for single steps: in (a) for $G = 0$ and (b) for $G = 0.25G_Q$, at $T = 100$ mK; in (e) for $G = 0.85G_Q$ and (f) for $G = G_Q$ at $T = 0$ K.

coupled to leads by tunnel junctions with many weakly transmitting channels [Hu *et al.*, 1994; Hu and O'Connell, 1995; Zwerger, 1994; Grabert, 1994; Hofstetter and Zwerger, 1997; Wang, 1997; Falci *et al.*, 1994; Glazman and Matveev, 1991; Matveev, 1991] and for semiconductor quantum dots coupled to leads by quantum point contacts with a single transmitting channel [Furusaki and Matveev, 1995; Matveev, 1995]. For metal systems in the weak tunneling limit, Matveev [1991] calculated the gate voltage V_g dependence of the box charge using the Hamiltonian:

$$H = H_0 + H_T$$

$$H_0 = \sum_k \varepsilon_k a_k^+ a_k + \sum_p \varepsilon_p a_p^+ a_p + \frac{\hat{Q}^2}{2C_\Sigma} + \alpha V_g \hat{Q}$$

$$H_T = \sum_{k,p}\left(t_{kp} a_k^+ a_p + t_{kp} a_p^+ a_k\right)$$

The terms ε_k are the energy levels in the box, the ε_p are the energy levels in the leads, the $a_{k/p}{}^+/a_{k/p}$ are the creation/annihilation operators for electrons in the dot/leads, and C_Σ is the total dot capacitance. Q is the box charge operator given by:

$$\hat{Q} = e\sum_p a_p^+ a_p$$

The term H_T is the tunneling Hamiltonian which accounts for tunneling from the box to the lead. In this case, H_T is treated as a perturbation and is used to calculate the second order correction to the charge on the metal island due to quantum fluctuations. This correction is given by:

$$Q = Q_0 + eg\ln\left(\frac{e/2C - \alpha V_g}{e/2C + \alpha V_g}\right)$$

where $\alpha \equiv C_g/C$ and g is the dot-to-lead coupling in units of G_Q. Equation 4.1 was calculated for zero temperature: this expression is applicable in the weak tunneling limit where quantum fluctuations of the dot charge dominate the behavior. However, it is only valid for regions of V_g where the box is in the Coulomb blockade regime, i.e. away from the charge degeneracy points where the box charge can fluctuate without energy cost from N to N + 1 electrons. In fact, the strong Coulomb blockade regime is the only region of interest for our purposes, as we are investigating the effects of quantum fluctuations of the box charge. At the charge degeneracy points, the effects of thermal fluctuations are strongest and mask the effects of quantum fluctuations. Thus, in our analysis, we will focus on the strong Coulomb blockade regions, i.e. the values of V_g corresponding to the centers of the single electron steps in Fig. 4.7. The above equation was used to plot the insets to Figs. 4.7 (a) and (b).

Matveev [1995] has also considered this situation theoretically by computing the Coulomb interaction energy of a quantum box connected to an electron reservoir by a quantum point contact in the tunneling regime. This energy is shown to evolve continuously from its capacitive value in the weak tunneling limit $G << G_Q$ to precisely zero at $G = G_Q$ where charge quantization and the Coulomb blockade are completely destroyed. In this theory, as G increases from 0 to G_Q, the charge steps are rounded and the slopes of the horizontal plateaus increase; this is evident in the data in Fig. 4.7. In this approach, the backscattering at the point contact is treated as a perturbation to calculate the correction to the box charge in the regime of strong tunneling. The resulting expression for the charge on the box in this limit is:

$$Q = eN - \frac{\gamma}{\pi} e|r| \sin 2\pi N$$

where the induced number of electrons $N \equiv C_g V_g / e$, $r = 1\text{-}g$ is the reflection coefficient of the tunnel barrier, and $\gamma = e^C$, where $C \approx 0.5772$ is Euler's constant. This expression was used to plot the insets to Figs. 4.7 (e) and (f).

The data of Fig. 4.7 can be compared with theory by considering how the shapes of the single electron steps evolve with G, in particular the slopes of these steps at the midpoints. As mentioned above, at the center of each horizontal plateau the influence of tunneling is most directly seen, whereas at the vertical sides of the charge steps, where the Coulomb blockade goes to zero, the effect of thermal fluctuations is greatest. Thus we can characterize the strength of quantum fluctuations by the slope $S = dQ_{box}/dQ_{ind}$ of the plateau at its center, where Q_{box} is the actual box charge including the effects of quantization, and Q_{ind} is the charge capacitively induced by V_L. For perfect charge quantization $S = 0$; when quantization is completely destroyed, $S = 1$ as for a classical capacitor.

Figure 4.8 utilizes this quantity S to compare the destruction of charge quantization by quantum mechanical tunneling for a large data set similar to Fig. 4.7 with theory. In the weak tunneling limit $G << G_Q$ theory predicts that charge is precisely quantized; the charge steps are horizontal and the slope $S = 0$. This is evident in the data in Fig. 4.8: the slope starts at $S \approx 0$ and rises continuously with G as the charge steps begin to smooth out. In the weak tunneling limit the data rise somewhat more rapidly than perturbation theory calculations [Matveev, 1991; Grabert, 1994; Falci *et al.*, 1994], although the theoretical prediction falls within the error bars. This discrepancy was also observed by David Berman at MIT [Berman *et al.*, 1999] and is not yet understood. In the strong tunneling limit $G_Q - G << G_Q$ charge fluctuation theory [Matveev, 1995] predicts that charge quantization in a single electron box connected to a reservoir by a one-dimensional channel is completely destroyed at precisely $G = G_Q$. The theoretical slope S vs. G in the strong tunneling limit is shown by the solid curve in Fig. 4.8 which rises sharply with G then saturates for $G \geq G_Q$. This predicted behavior is confirmed by our charge measurements: the most dramatic feature of the data in Fig. 4.8 is a sharp increase of the slope S with tunnel conductance just below $G = G_Q$ followed by an abrupt saturation at $S \approx 1$ for $G > G_Q$. Single electron steps are completely absent in the data above $G = G_Q$, as for Fig. 4.7 (f). These measurement are the first which expore the breakdown of charge quantization in a single-electron box over this full range of dot-to-lead conductance values.

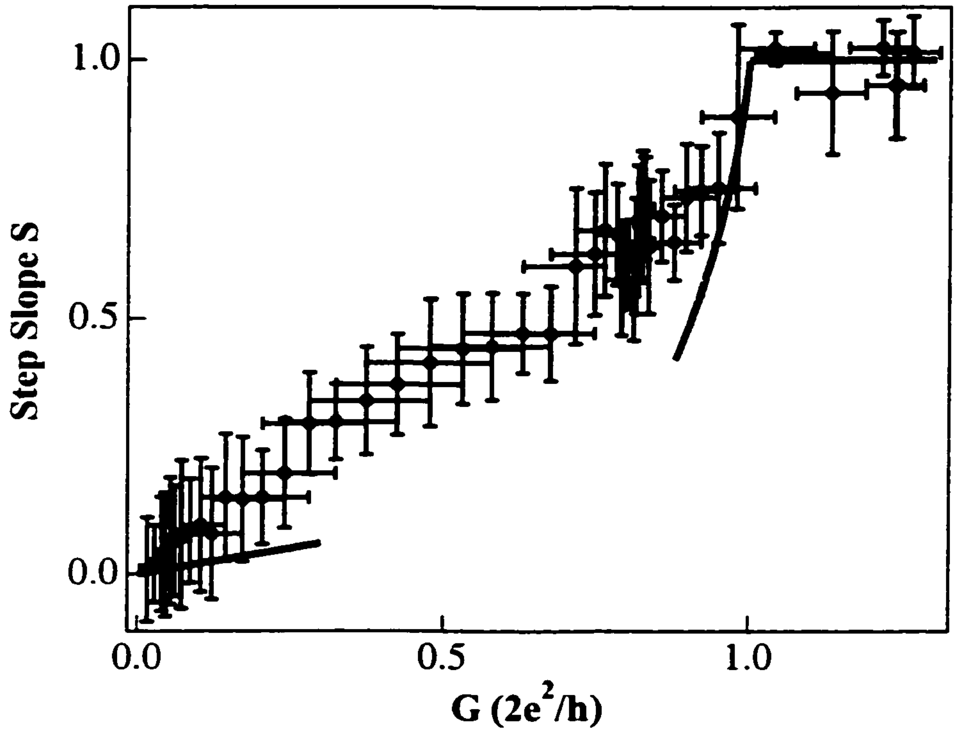

Figure 4.8 Average slope $S = dQ_{box}/dQ_{ind}$ (Q_{box} and Q_{ind} are the actual and induced box charge respectively) of single electron steps at the midpoint of the plateaus vs. tunnel-conductance G of the box to the lead. Each data point in Fig. 4 is derived from the average of many sweeps of G_{elect} vs. lead voltage V_L. The slope S was found using the vertical spacing of single electron steps to calibrate changes in Q_{box} from G_{elect} and the horizontal step spacing to calibrate changes in Q_{ind} from V_L. The conductance G of the upper box point contact was calibrated vs. gate voltage V_{q1} by measuring G vs. V_{q1} with the lower point contact open for several values of V_{q2}, followed by an extrapolation to the case where the lower point contact is completely pinched off. The error bars are estimates of the total statistical and systematic error. Solid gray curves are the theoretical predictions in the weak tunneling limit (3-dimensional theory is applicable in this limit) and in the strong tunneling limit for values of G near G_Q. The slope $S \sim 0$ for $G << G_Q$ and rises sharply just below $G = G_Q$, saturating at $S = 1$ for $G > G_Q$ as predicted by theory.

4.5 Conclusion

In this chapter, I have presented experiments on the direct measurement of the destruction of charge quantization in a single-electron box. We studied the evolution of single electron charging in a box using a sensitive single-electron transistor electrometer as a function of box-to-lead conductance over the full range of conductance values from $G = 0$ to $G = G_Q$, the first such measurement. We have found that the quantization of charge in the box is destroyed at a value of $G = G_Q$ in agreement with theory.

Chapter 5

Spin Effects in a Small Quantum Dot

5.1 Introduction

This chapter describes a set of experiments on small quantum dots in which the effects of electron spin on dot energy spectra are investigated. The initial motivation behind this work was some intriguing data taken by David Goldhaber-Gordon at MIT and described in his Ph.D. thesis [Goldhaber-Gordon, 1999]. In his investigations of the Kondo effect in single-electron transistors, he observed patterns in Coulomb blockade peak measurements that appeared to be evidence for electrons filling spin-degenerate energy states as they were added to the dot. In particular, pairs of Coulomb blockade peaks were found to be similar in height over a range of eight peaks, from which an assignment of even vs. odd number of electrons in the dot could be made. Furthermore, the spacings between these peaks were observed to alternate in a parallel magnetic field in a manner consistent with the electron number assignment, and to evolve in a changing magnetic field in a manner suggesting a Zeeman contribution to the dot ground state energy. However, switching noise in the sample prevented further investigation of these effects. Thus, we fabricated additional devices at Harvard to search for and study more extensively spin effects in quantum dots.

The role of the electron spin in the energy spectra of nanostructures has been the subject of much recent experimental and theoretical interest in the mesoscopic physics community. This is due to the intrinsic interest of the subject as well as the importance of spin for potential applications ranging from spin-based electronics to quantum computing [Bukard *et al.*, 1999]. In semiconductor quantum dots, electron spin is generally only indirectly manifested, although extensive measurements have been made attempting to observe effects of electron spin directly. In asymmetric dots, the statistics of Coulomb blockade peak spacings were studied in search of a bimodal spacing distribution signifying spin-degenerate filling of energy levels. However, no such distribution was observed [Patel *et al.*, 1998]. Other experiments have examined the statistics of Coulomb blockade peak heights, but found no evidence of the peak pairing that might point to spin-degeneracy in quantum dots [Folk *et al.*, 1996; Chang *et al.*, 1996; Sivan *et al.*, 1996]. Similarly, measurements of the correlations between ground and excited state spectra in an asymmetric dot have supported a single particle picture of state filling, but without spin degeneracy [Stewart *et al.*, 1997]. On the other hand, shell structure has been observed in a cylindrically symmetric dot, in agreement with a spin-degenerate single-particle picture modified according to Hund's rules [Tarucha *et al.*, 1996]. Spin effects, including Zeeman splitting of energy levels and spin-orbit interactions, have also been observed in metallic nanoparticles [Ralph *et al.*, 1995; Black *et al.*, 1996; Ralph *et al.*, 1997; Davidovic and Tinkham, 1999a; Davidovic and Tinkham, 1999b] and carbon nanotubes [Cobden *et al.*, 1998; Tans *et al.*, 1998]. Recent theoretical work on metallic particles has demonstrated a significant probability of finding a nonzero net spin in the ground state due to exchange effects [Brouwer *et al.*, 1999]. However, other recent work has described a competing mechanism - fluctuations in the off-diagonal interaction matrix elements - that favors a minimum-spin ground state [Jacquod and Stone, 1999].

In this chapter, Coulomb blockade spectroscopy measurements on a small, asymmetric GaAs/AlGaAs quantum dot in a magnetic field oriented parallel to the plane of the sample are described. By noting the shift of successive Coulomb blockade peaks upon application of a parallel field, we are able to observe behavior consistent with spin effects while minimizing the influence of the magnetic field on electrons' spatial states. We analyze our data in terms of spin, while recognizing that orbital effects may also be important, particularly at higher magnetic fields. For example, the peak motion, corresponding to the evolution of the ground state energy with magnetic field, can be understood in terms of Zeeman coupling. Following this interpretation, we are able to determine how the total ground state spin changes as each successive electron is added, and we note that these changes do not occur in a strictly alternating spin up/spin down manner. We also observe features in our data that are not adequately described in terms of spin, and we discuss orbital effects as the possible cause. In addition, results on nonlinear conductance measurements in parallel magnetic field are presented.

5.2 Device and Device Characterization

Figure 5.1 shows (a) a scanning electron micrograph and (b) a schematic diagram of the device, a quantum dot defined inside a GaAs/AlGaAs heterostructure by electrostatic gates in the manner described in Chapter 2. The heterostructure contains a two-dimensional electron gas (2DEG) with mobility 5×10^5 cm^2/Vs and sheet density 3.5×10^{11} cm^{-2} located 47 nm below the surface. Metal gates were fabricated using our usual electron beam lithography and Cr/Au metallization procedure. As shown in Fig. 5.1(b), two quantum point contacts connect the dot to the 2DEG outside, and gate voltages V_{g1} and V_{g2} can be varied to induce electrons to enter or exit the dot. The lithographic size of the dot was 200×250 nm^2, and the size of the electron pool was $\cong 100 \times 150$ nm^2. This disparity between lithographic and actual dimensions of the dot results from the depletion length of the metal gates: the electrostatic barriers defining the dot boundaries extend beyond the gates themselves. A typical *ansatz* for this length is the depth of the gas; thus, we arrive at an estimate of 100×150 nm^2, and a quantum dot which contains ~ 30 electrons. A very small dot was fabricated on the theory that spin effects in semiconductor quantum dots might be more prominent in small dot [Goldhaber-Gordon, 1999]. Most investigations of spin effects in semiconductor dots examined dots with linear dimensions ~ 1 micron; our quantum dot is considerably smaller.

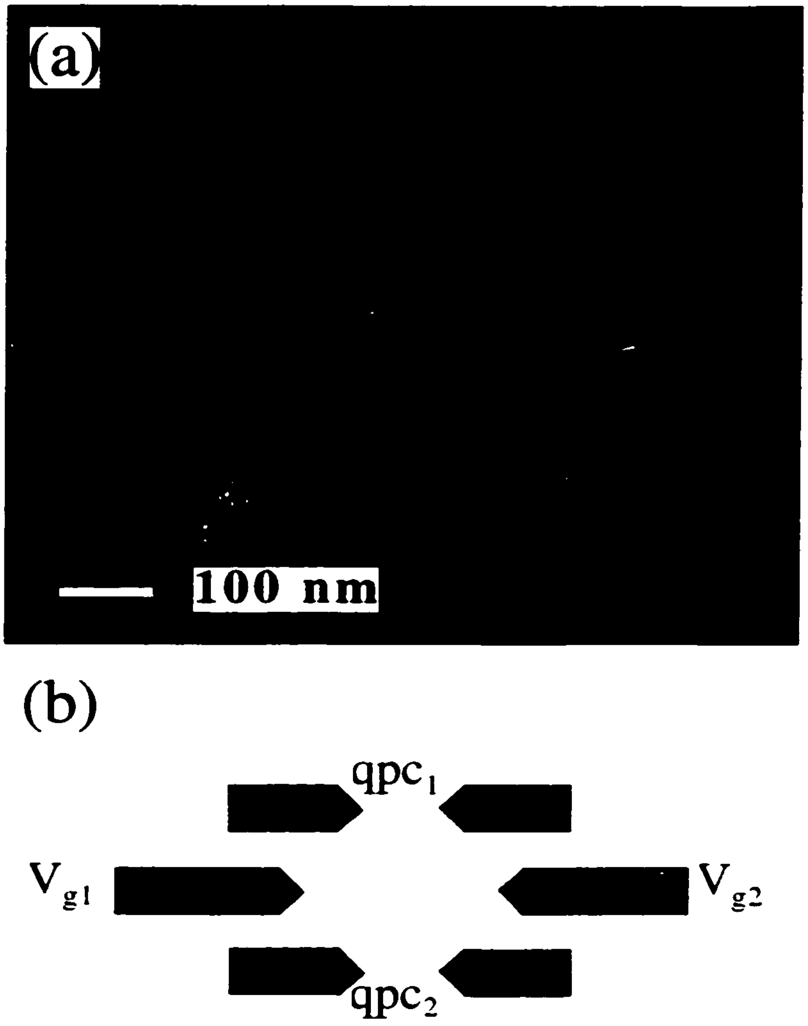

Figure 5.1 (a) Scanning electron microscope photograph of the device, a single quantum dot defined electrostatically in a GaAs/AlGaAs heterostructure containing a 2-dimensional electron gas. The lithographic dimensions of the dot are 200 x 250 nm^2; the actual dot dimensions are approximately 100 x 150 nm^2. The dot contains ~ 30 electrons. The light regions in the photograph are the metal gates which, when energized, define the contours of the dot. (b) Schematic wiring diagram of the device. Electrons can tunnel on and off the dot via the two quantum point contacts qpc1 and qpc2; electrons can be induced to do so by varying the voltages on the capacitively coupled sidegates V_{g1} and V_{g2}.

Several measurements were made to tune the dot in the Coulomb blockade regime and to characterize it. The sample was cooled in a dilution refrigerator to a base temperature of 12 mK, and measurements of dot conductance were made using the ac lockin techniques described in Chapter 3. Figures 5.2 (a) and (b) depict zero-bias differential conductance measurements of the two dot quantum point contacts. Both traces show clear conductance plateaus which are integer multiples of $2e^2/h$, as expected. However, the specific features of each point contact trace differ, illustrating the degree of variation it is possible to observe in nominally identical point contacts. Such variation is due to differences in the impurity potential in the vicinity of the point contacts as well as small lithographic variations from one point contact to another, which affect the interference patterns of electron waves traveling through the point contact.

Conductance measurements were then made with the quantum point contacts tuned such that the dot was in the Coulomb blockade regime with weak tunneling ($G << 2e^2/h$). A typical resulting trace is shown in figure 5.2 (c), which depicts the familiar Coulomb blockade peaks in the conductance. The distance between peaks corresponds to the energy needed to add one additional electron to the dot. Thus, this type of measurement can be used to do spectroscopy on the addition spectrum of the quantum dot. By observing the shifts in peak spacings as other parameters, such as parallel magnetic field, are varied, the evolution of the addition spectrum can be studied.

To further characterize the dot, nonlinear conductance measurements on the quantum dot were made. The measurement setup for this was also described in Chapter 3. The differential conductance through the dot was measured as a function of the sidegate voltage V_{g1} and the drain-source bias V_{ds}. Figure 5.3 depicts the results of these measurements, a grey-scale plot of the differential conductance. The light regions indicate high conductance, the dark regions low. Much information can be obtained from this plot. As described in Chapter 2, the slopes of the edges of the "Coulomb diamonds" yield information on several capacitance values: the total capacitance of the dot $C_\Sigma = 115$

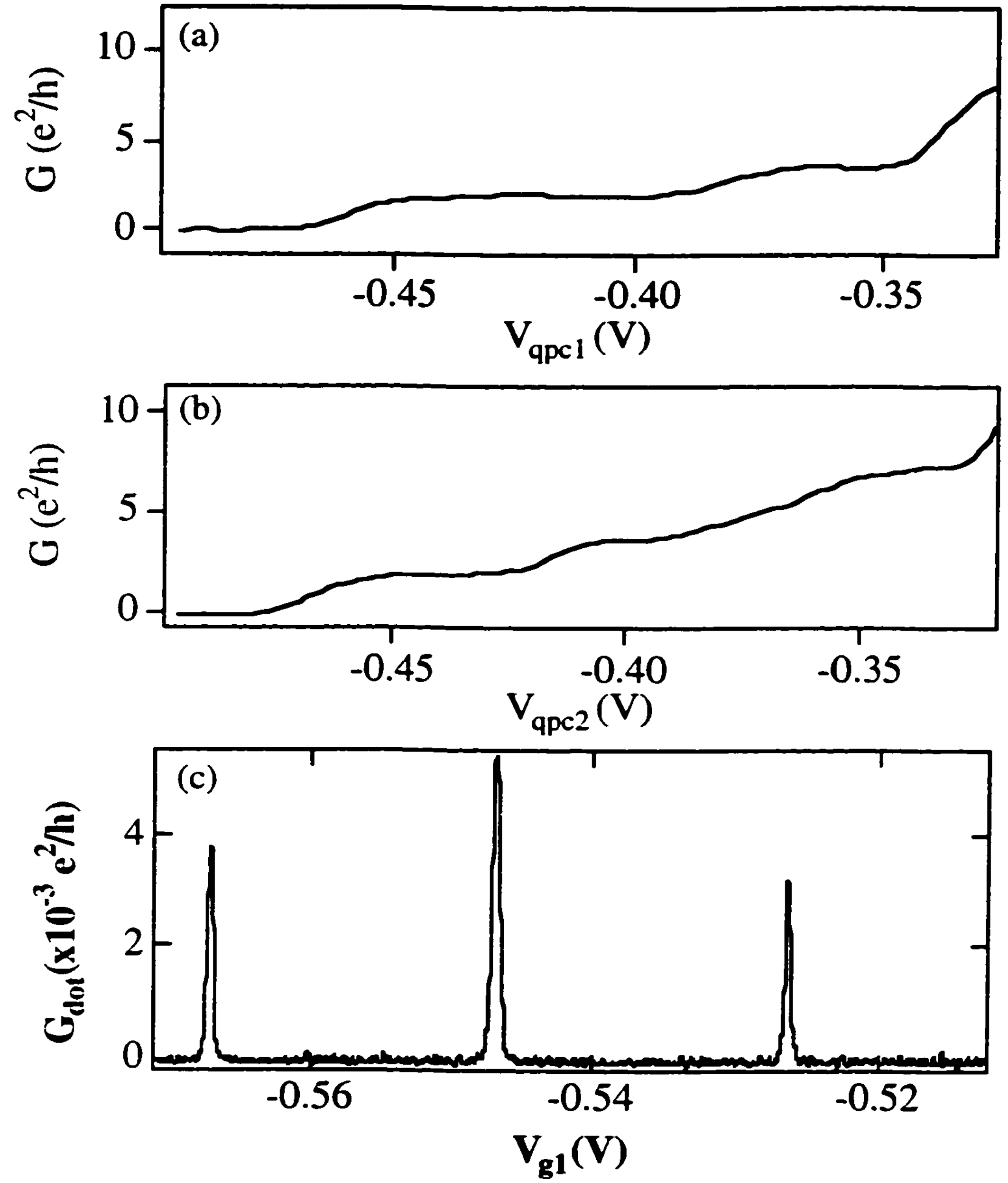

Figure 5.2 (a) Measured differential conductance through quantum point contact 1 as a function of the voltage V_{qpc1} applied to the quantum point contact gate. A more negative voltage on V_{qpc1} results in a narrower point contact channel; conductance decreased in quantized steps of G_Q. (b) Similar measurement for quantum point contact 2. Variations in the fine structure of the two point contact conductance traces are due to small variations in lithography as well as variations of the impurity potential in the vicinity of the two point contacts. (c) Differential conductance through the quantum dot with point contacts tuned in the weak tunneling regime. Coulomb blockade peaks in the conductance occur as a function of V_{g1}. The distance between peaks corresponds to the energy to add one additional electron to the dot, enabling spectroscopy of the addition spectrum of the quantum dot.

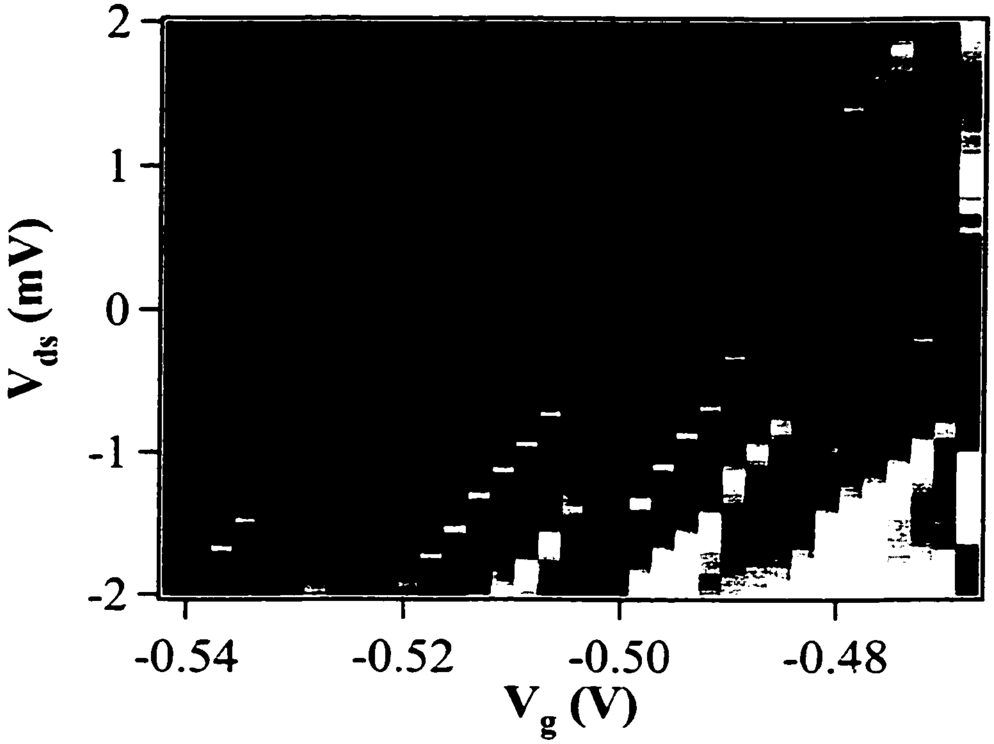

Figure 5.3 Measured differential conductance through the quantum dot as a function of sidegate voltage V_g and drain-source bias V_{ds}. Light regions correspond to high conductance, dark regions to low. The diamond shaped regions are regions of Coulomb blockade where an integer number of electrons is stable. Excited states are accessed as V_{ds} is swept, and are visible as stripes parallel to downward sloping edges of the diamonds.

aF, the capacitance of the dot to the lead $C_L = 19$ aF, and the capacitance of the dot to the sidegate $C_g = 8.3$ aF. From these values, the charging energy $e^2/C_\Sigma \cong 1.4$ meV and the capacitance ratio $\alpha \equiv C_g/C_\Sigma = 0.072$ were determined.

Also evident in figure 5.3 are many excited state levels which are accessed as V_{ds} is swept. Cuts through the data of figure 5.3 are depicted in Figs. 5.4 (a) through (c) corresponding to three different fixed values of the voltage V_g. In Figs. 5.4 (a), (b), and (c) the number of electrons in the dot in the ground state are N - 1, N, and N + 1, respectively. Excited states are manifested as peaks in the conductance which occur after the Coulomb blockade has been overcome by V_{ds}. It is evident that different excited states are accessed at different values of ground state electron number. However, the typical spacing between excited state peaks gives a measure of the average spacing between energy levels. For our dots, this value is $\Delta\varepsilon \cong 150$ µeV. Because $\Delta\varepsilon >> kT = 10$ µeV, our dots are in the "quantum Coulomb blockade" or resonant tunneling regime, in which transport occurs primarily by resonant tunneling through individual quantum states in the dot. In Fig. 5.4 (c), a negative differential conductance peak appears at $V_{ds} \approx -1.2$ mV. It has been suggested that such peaks are due to accessed levels which are very weakly coupled to the leads (Stewart, 1999).

5.3 Magnetic field data and analysis

Figure 5.5 shows the principal data: how the Coulomb blockade peaks in dot conductance G_{dot} vs. gate voltage V_{g1} shift with in plane magnetic field B; light regions correspond to high conductance, dark regions to low. As discussed above, the position of each peak is determined by the energy necessary to add one additional electron to the dot. This energy is the sum of a capacitive component and a component which is the energy of an additional electron on the dot when the charge induced by V_{g1} is zero. From Fig. 5.5 it is clear that the addition energy is altered by magnetic field: as the magnetic field is swept from 0 T to 8.5 T, all peak positions are observed to curve. This peak

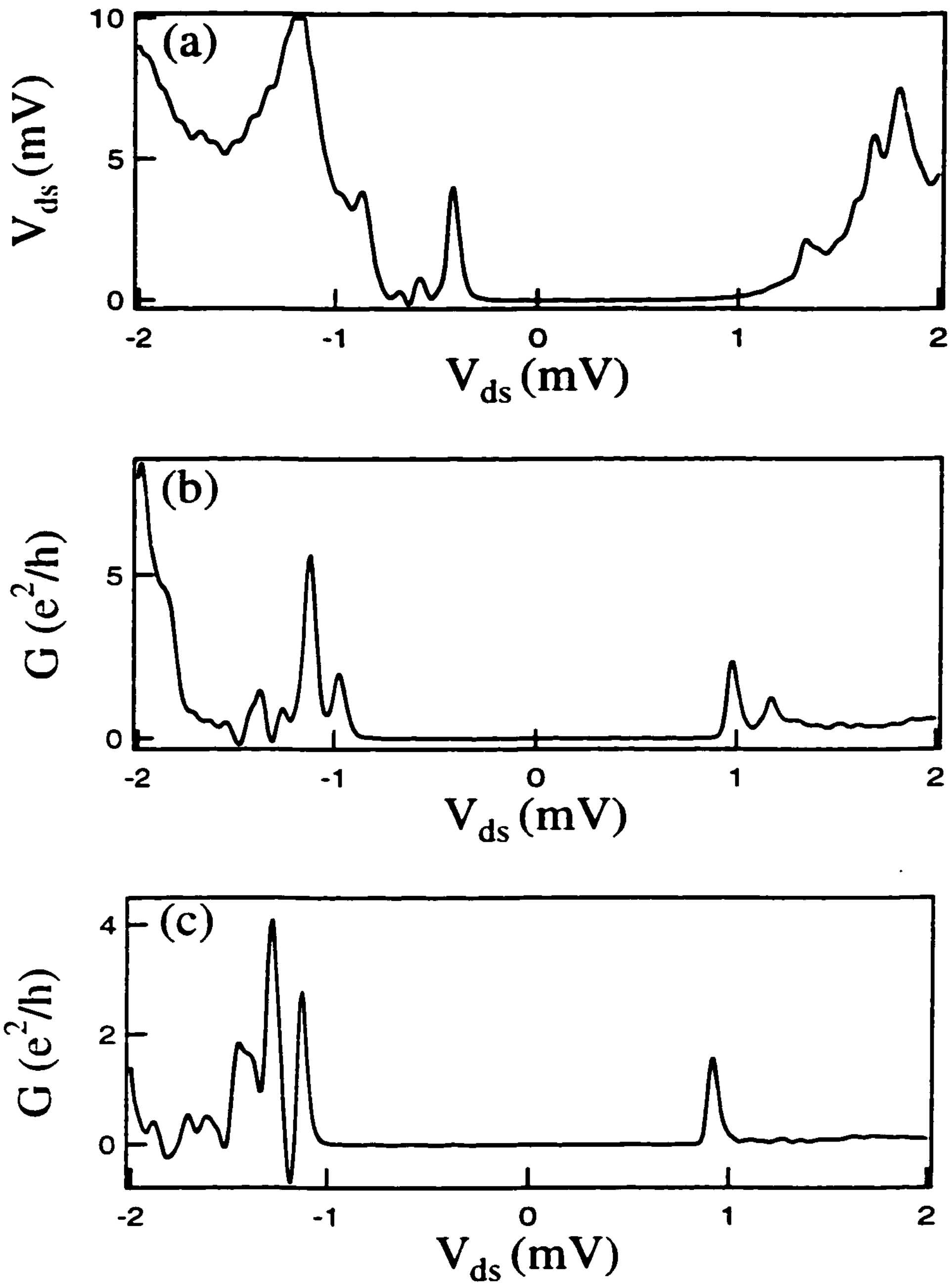

Figure 5.4 Vertical cuts through the Coulomb diamond pattern of Fig. 5.3 for (a) N - 1, (b) N, and (c) N + 1 electrons in the dot. The zero conductance, flat region, most evident in (b) between V_{ds} = -0.9 mV and V_{ds} = +0.9 mV is due to the Coulomb blockade of tunneling; the width of this zero-conductance plateau corresponds to the charging energy that must be overcome to add one electron to the dot. Sharp peaks to the sides of the Coulomb blockade region are excited states which become accessible as the magnitude of V_{ds} is raised. In (c), a negative differential conductance spike is evident at V_{ds} = -1.2 mV.

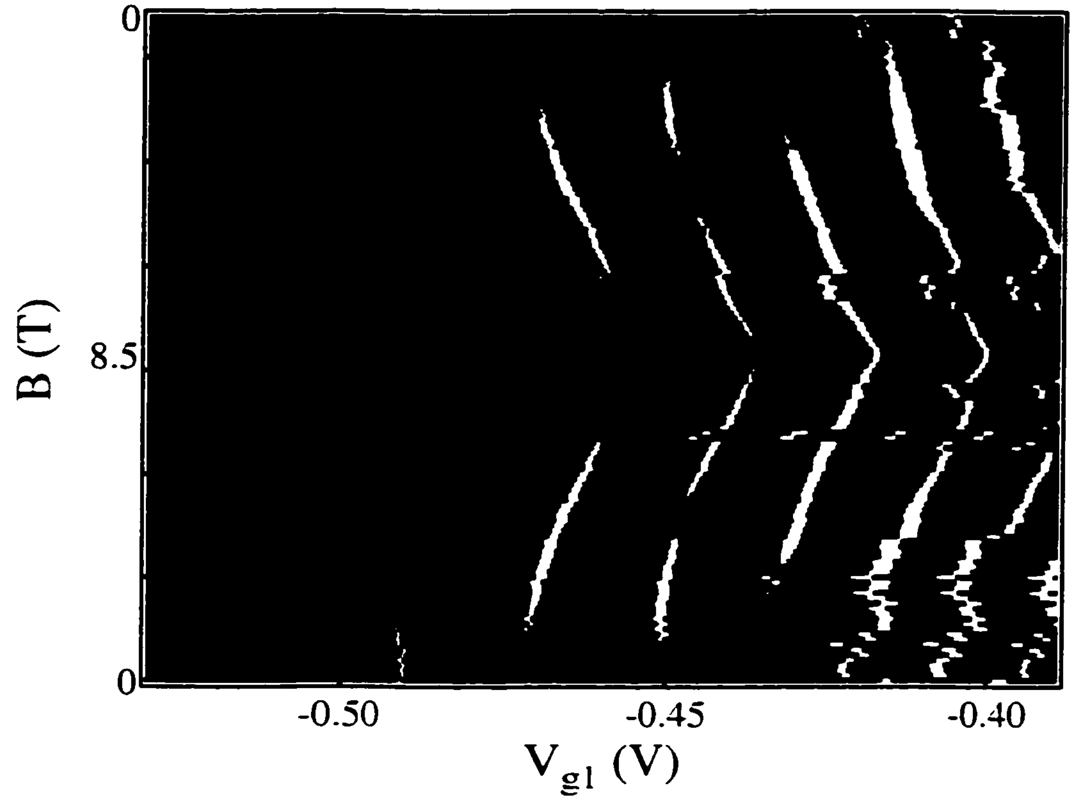

Figure 5.5 Measured differential conductance through the dot as a function of sidegate voltage V_{g1} and parallel magnetic field B. Light regions are high conductance, dark regions are low. Coulomb blockade peak positions curve as the field is raised, providing information on the interplay of electron spin and orbital effects in the addition spectrum of the quantum dot. Large, common peak motion is due to coupling of the field to the transverse component of the electron wavefunctions. Small, relative peak motion can be interpreted as due to the Zeeman contribution to the dot ground state energy. Abrupt shifts in peak positions are caused by switching noise.

motion will be analyzed further to understand the way in which electron spin and orbital effects combine to determine the ground state energy of a quantum dot.

The motion of each peak in Fig. 5.5 can be separated into two principal components: a large shift common to all peaks, and smaller, independent peak shifts which require more careful analysis. The common shift has been observed previously [Weis *et al.*, 1993; Weis *et al.*, 1994] and is caused by coupling between the magnetic field and the transverse component of the electron wavefunctions [Stern, 1968]. This larger peak motion may also vary slightly for each peak due to the unevenness of the GaAs/AlGaAs 2DEG interface and the changing size of the dot as electrons are added. The independent, smaller peak motion we interpret as due to a Zeeman contribution to the dot ground state energy, a consequence of the electron spin. The Zeeman contribution to the peak position is negative when the electron added has spin up, and positive when the electron added has spin down. However, it should be noted that orbital effects may also contribute to the smaller, relative peak motion. The parallel field could cause fluctuations in the dot ground state energy which depends on the particular spatial distributions of the electron wavefunctions, which vary from level to level. Differentiating between which peak motion is due to spin and which is due to orbital effects is a subtle problem. Another possible cause of peak motion may be a small perpendicular component of the magnetic field, shown by Shubnikov-de Haas measurements to be $\approx 3°$ out of plane. This component is not likely to be significant, at least at low fields, as it corresponds to only one flux quantum penetrating the dot at 8.5 T, the highest field used in our measurements. Abrupt shifts in the locations of individual peaks are caused by switching noise.

Figures 5.6 (a) and (b) depict an interesting contrast between the low and high field behaviour of our dot. Figures 5.6 (a) and (b) are horizontal cuts through the data set of figure 5.5, corresponding to single sweeps of V_{g1}. Figure 5.6 (a) is for B = 0 T, and (b) is for 8.5 T. The peaks labeled 1 to 5 are observable in both sweeps. Comparing successive peak spacings in the two sweeps reveals a striking contrast: at B = 0 T, the spacings

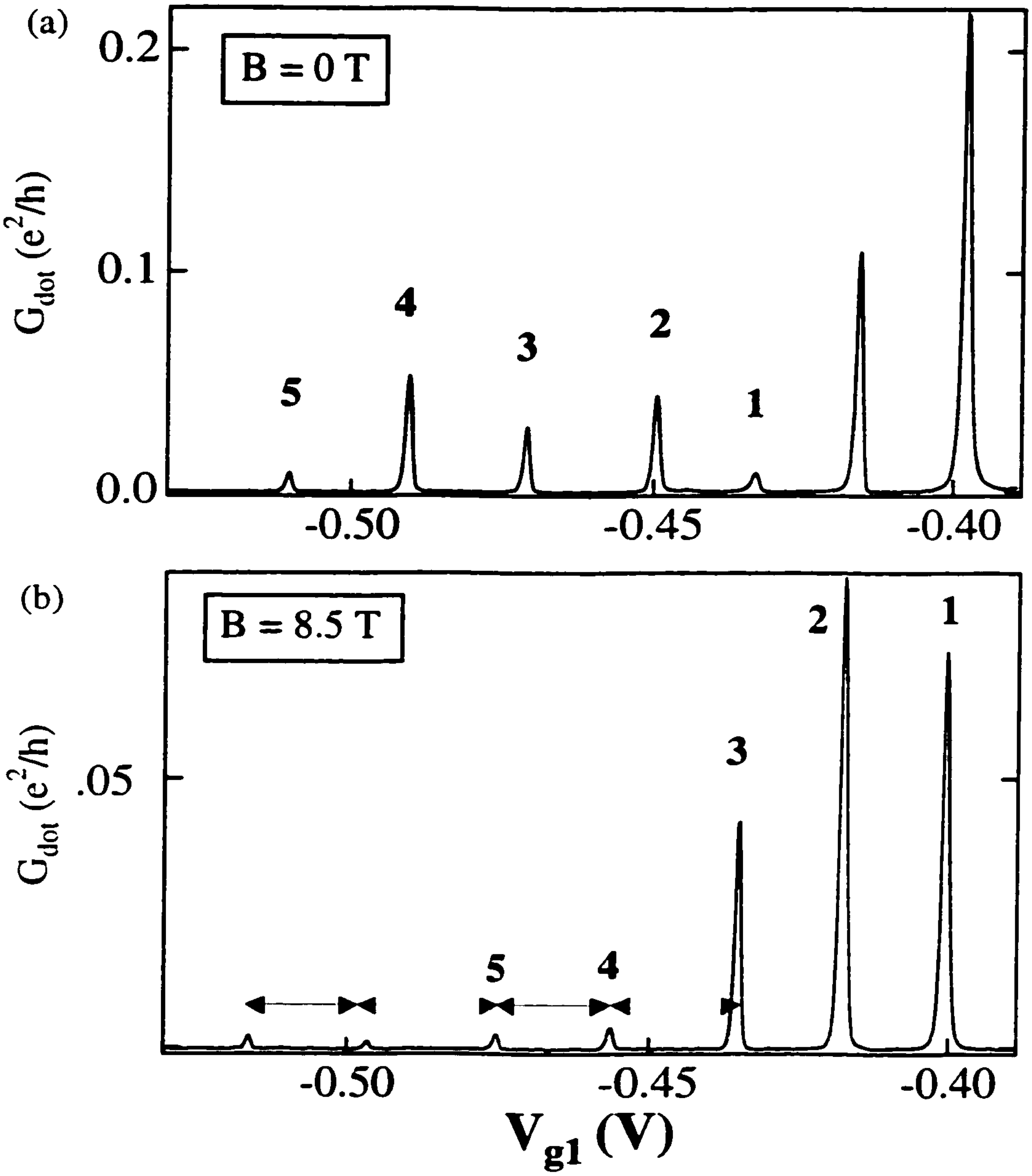

Figure 5.6 Measured differential conductance through the quantum dot as a function of sidegate voltage V_{gl} at (a) B = 0 T and (b) B = 8.5 T. Both traces show a series of Coulomb blockade peaks; the peaks numbered 1 to 5 are the same in each trace. The same set of peaks is not measured at all field values because ramping the field shifts some peaks out of the measurement window. At B = 0 T the spacings between peaks are approximately equal; at B = 8.5 T the spacings follow an alternating small/large pattern. Alternating peak heights are also observed at B = 0. Both of these patterns suggest pairing of electrons in spin-degenerate levels.

are approximately equal, and variations in spacing follow no discernible pattern, although we do observe alternating peak heights. At B = 8.5 T, the peak spacings follow an alternating small/large pattern. This phenomenon of alternating peak spacings at high field was observed in three distinct sets of Coulomb blockade peaks in our dot and is reminiscent of data taken by David Goldhaber-Gordon [1999], in which he observed a similar alternation of peak spacings at high magnetic field. Such alternating patterns are suggestive of pairing of electrons in spin-degenerate energy levels as the electrons are added to the dot.

Figures 5.7 (a) and (b) are the result of analysis done on the dataset of Fig. 5.5, and present the key results of our experiment, providing evidence for our view that we observe manifestations of electron spin in the addition energy for electrons in our dot. Figure 5.7 (a) shows peak positions vs. gate voltage V_{g1} and magnetic field B: in this case, we only show the peak positions. To obtain Fig. 5.7 (a), each Coulomb blockade peak was fitted to the functional form for thermally-broadened resonant tunneling through a single quantum state, described in Chapter 2. This enabled the more precise determination of peak position, relevant for the analysis of Fig. 5.7 (b).

Figure 5.7 (b) shows the evolution with magnetic field of the spacings between successive peaks in Fig. 5.7 (a). We chose to examine the spacings between successive peaks in order to isolate the relative peak motion from the common peak motion, and to minimize the effects of switching noise. Each of the curves of Fig. 5.7 (b) corresponds to the spacing between two consecutive peaks, labeled A to E in Fig. 5.7 (a). The evolution of these spacings with magnetic field gives information about the changes in spin of successive ground states as electrons are added to the dot. For example, spacing A in Fig. 5.7 (b) increases with magnetic field. This means that the two electrons added on the Coulomb blockade peaks bracketing A change the spin of the ground state by +1/2 and −1/2, respectively. Spacing A increases with magnetic field, because the energy to add the first, spin up, electron is lowered by the Zeeman energy, and the energy to add the

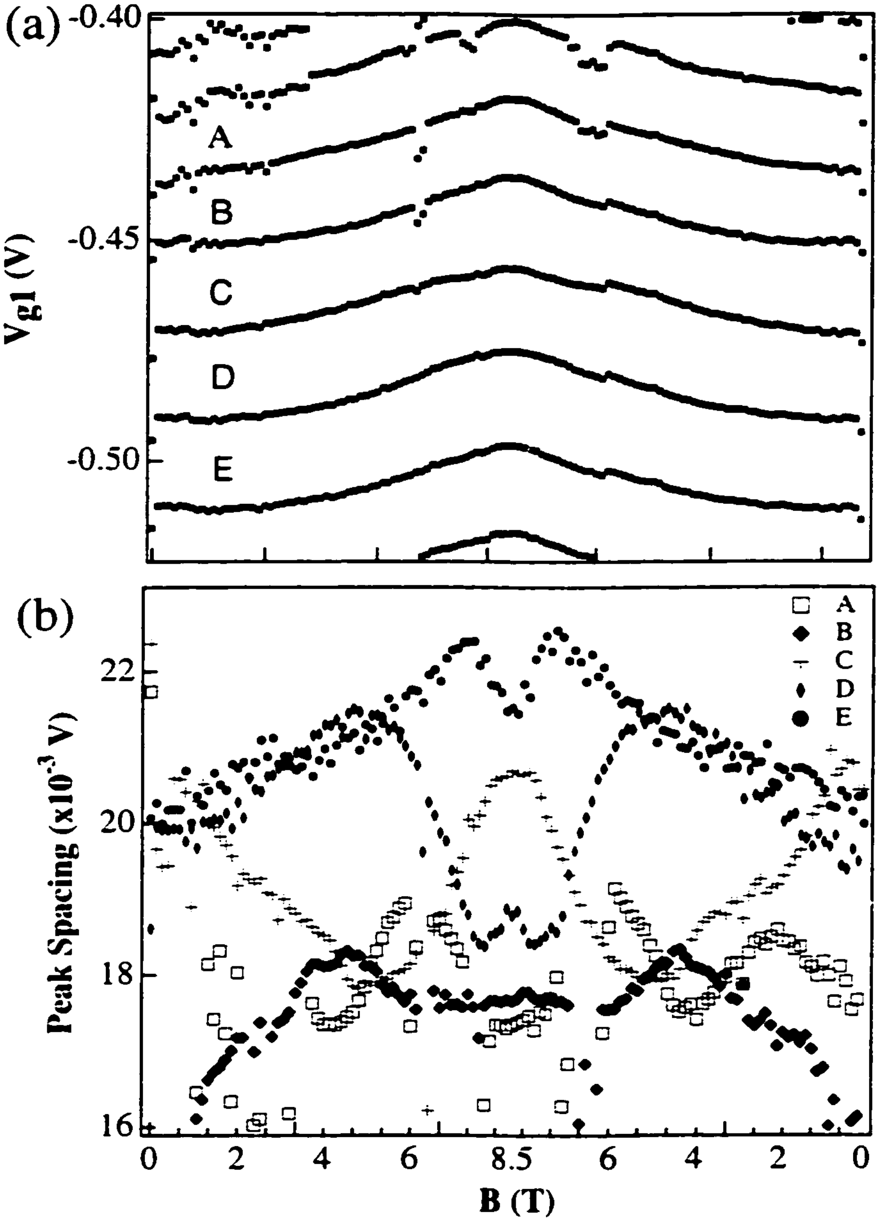

Figure 5.7 (a) Coulomb blockade peak positions vs. sidegate voltage V_{gl} and parallel magnetic field B. Data is the same as in Fig. 5.4, but each peak was fitted to the functional form for resonant tunneling through a single quantum state in a quantum dot in order to more precisely determine peak positions. Spacings between consecutive peaks are labeled A to E. (b) Spacings between consecutive Coulomb blockade peaks vs. parallel magnetic field B. The slopes of the spacings vs. B provide information on the changes in spin of successive ground states as electrons are added to the dot. The g-factors of these electrons can be measured and range in magnitude at low field from 0.43 to 0.57, comparable to the magnitude of the g-factor for bulk GaAs of $g = 0.44$.

second, spin down, electron is raised by the Zeeman energy. Conversely, a spacing that decreases with field must occur between two Coulomb blockade peaks at which electrons are added spin down and spin up, respectively, and a constant spacing implies that two successive electrons of the same spin are added. (By spin up we mean the spin state whose energy decreases with increasing field. For the negative g-factor in GaAs this state is oriented parallel to the direction of the applied field). The g-factors of added electrons can be obtained from the slope of spacings with magnetic field $g\mu_B m/\alpha$, where $\alpha \equiv C_g/C = 0.072$ for our dot, μ_B is the Bohr magneton, and m is the spin. At low field, the absolute values of all slopes are roughly equal, with g-factor magnitudes of 0.43 to 0.57, comparable to the g-factor in bulk GaAs $|g| = 0.44$ shown for the inset in Fig. 3(b). The fact that these measured g-factors are comparable to the bulk value for GaAs lends support to our interpretation that the peak motion is at least partially due to the electron spin.

Figure 5.8 is a schematic illustrating the changes in the spin of successive ground states as electrons are added to the dot. The leftmost vertical column shows the B = 0 T series of spin changes, showing that these changes to not occur in an alternating spin up/ spin down manner. We observed cases where two successive electrons are added with the same spin, for example spacing D which is constant at low field.

Fig. 5.8 also highlights interesting features at higher magnetic field. The peak spacings in Fig. 5.7 (b) tend to change with magnetic field in a series of connected segments. For example, spacing B changes from downward sloping to flat at ~ 6 T. Similar breaks in slope occurred for cylindrically symmetric dots [Tarucha *et al.*, 1996], and some evidence of similar breaks was seen by Stewart *et al.* [1997]. If spin were the principal cause, breaks in slope of Coulomb blockade peak spacings could occur when the spin of the ground state changes with magnetic field. Added spins which change sign with field are highlighted in gray in Fig. 5.8. Variations in the common motion of Coulomb blockade peaks with magnetic field, due to small changes in dot size and shape as electrons are

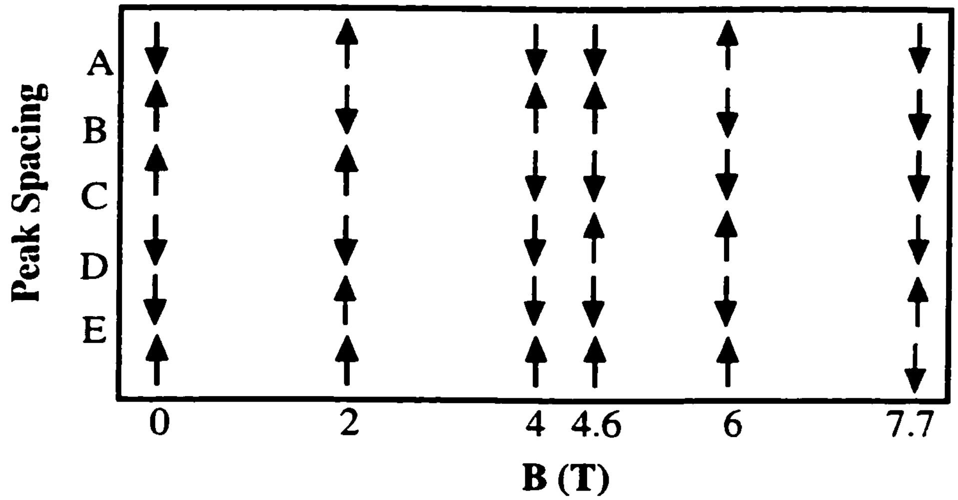

Figure 5.8 Schematic illustrating the changes in the total spin of successive ground states as a function of magnetic field and electrons added to the dot. This schematic corresponds to the data of Fig. 5.7 (b). Spin changes flip where a kink in the Coulomb blockade peak spacings of Fig. 5.7 (b) is observed; such flips are depicted in gray in Fig. 5.8. Changes in the spin of successive ground states do not occur in a strictly alternating up/down manner as electrons are added to the dot. Most spin flips are observed to occur at intervals of ~ 2 T.

added, may also contribute to this structure. Recent theory has proposed that statistics of such breaks in peak slope could be used to estimate the exchange energy of electrons in a quantum dot [Baranger *et al.*, 1999], though the present data are not sufficient for such an analysis. Some slopes are significantly larger at higher magnetic fields. For example the slope of spacing D between 5.6 T and 7.4 T corresponds to a g-factor of 0.98. This may be due to the increased importance of orbital effects at higher magnetic fields.

After studying the effects of electron spin on the ground state energy spectra, we looked for manifestations of electron spin in excited state spectra. In particular, we looked for evidence of Zeeman splitting of excited state levels. To investigate this, we tuned the quantum dot to the Coulomb blockade regime, and set the sidegate voltage V_{g1} such that the dot was tuned in the middle of the Coulomb blockade range, i.e. halfway between two Coulomb blockade peaks. We then repeatedly swept the drain-source voltage V_{ds} while measuring the differential conductance G. Between each sweep of V_{ds} the parallel magnetic field was incremented, and the evolution of the excited states observed. The result is shown in Fig. 5.9. As for the Coulomb blockade peaks, the most obvious manifestation of the magnetic field is an overall curvature of the excited state peak positions, again due to the coupling of the field to the spatial states.

Also apparent in Fig. 5.9 are several ranges of magnetic field where excited states diverge as the field is ramped. One clear instance of such a divergence occurs over the field range of B ~ 3 T to B = 0 T; the relative motion of these two peaks corresponds to a g-factor magnitude of 0.57. Similarly, figure 5.10 shows a clear example from another data set, taken in the manner of Fig. 5.9, but for a different range of V_{g1}; thus, these excited states correspond to a different ground state from that of Fig. 5.9. As the field is ramped down from a value of B = 6.8 T to B = 4.5 T, we observe the divergence of two excited state levels. This relative motion corresponds to a g-factor magnitude of ~ 0.61.

The data shown above on Coulomb blockade spectroscopy in a parallel magnetic field strongly suggest the electron spin affects the addition spectrum of a quantum dot.

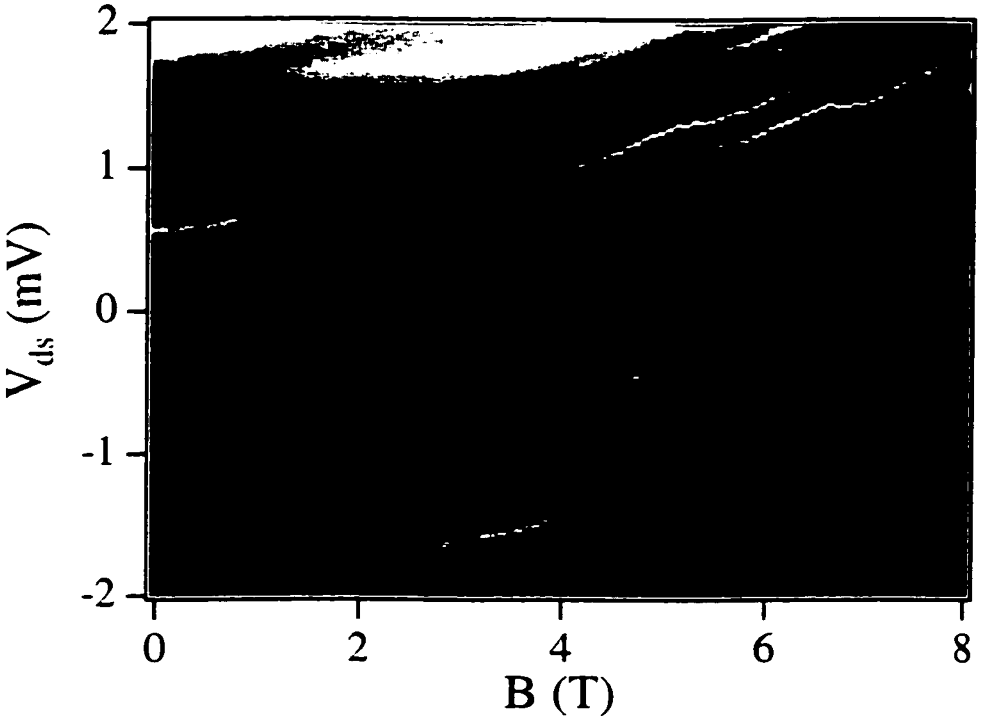

Figure 5.9 Measured differential conductance through the quantum dot as a function of parallel magnetic field B and drain-source voltage V_{ds}. Light regions are high conductance, dark regions low. At B = 0 T, a series of peaks in the conductance corresponding to excited states of the quantum dot are observed. The positions of these peaks curve with magnetic field due to the coupling of the field to the transverse components of the electron wavefunctions, as was the case for the zero-bias conductance measurements. Some excited states are observed to diverge as the parallel field is ramped.

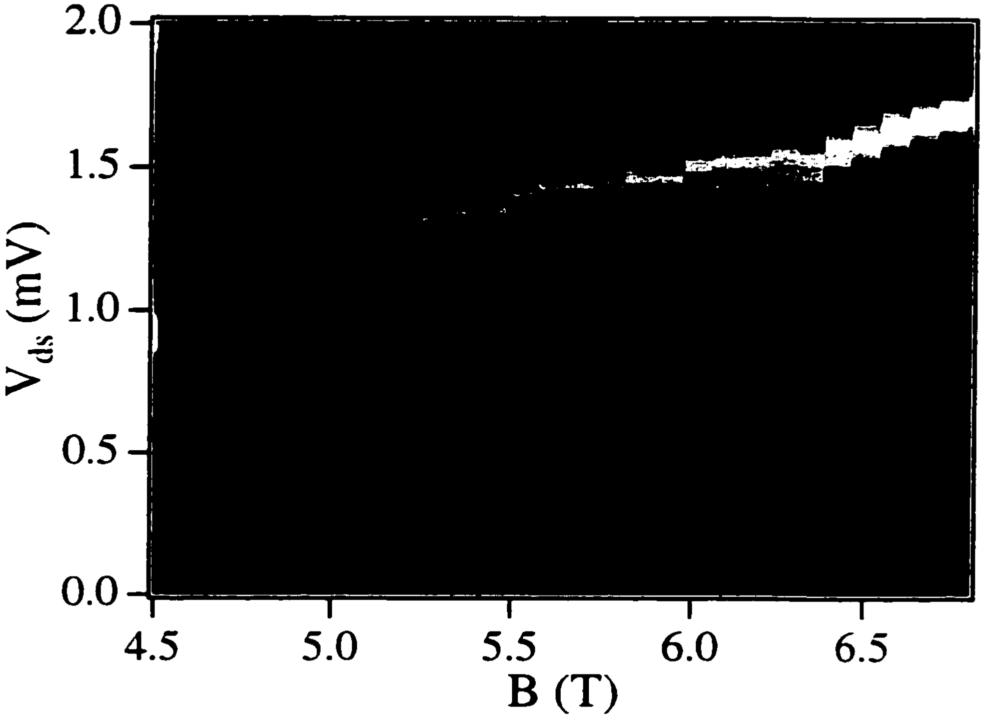

Figure 5.10 Differential conductance through the quantum dot vs. parallel magnetic field B and drain-source voltage V_{ds}. Two excited states are observed to diverge as the field is lowered from B ~ 6.8 T to B ~ 4.5 T. The relative motion corresponds to a measured g-factor magnitude of 0.61.

Figure 5.11 provides one more suggestive piece of evidence. This figure is from a previous set of experiments, the aim of which was not to investigate spin effects. The dot measured was one of a series double dot similar to the device described in Chapter 6. The lithographic dimensions were 500 x 500 nm^2, the sheet density of the heterostructure was 3 x $10^{11}/cm^{-2}$, and the data were taken at a dilution refrigerator temperature of 25 mK. The data show a series of 14 Coulomb blockade peaks. Strikingly, there is a strict alternation in Coulomb blockade peak heights over the full range of peaks. This behaviour is similar to the alternation of Coulomb blockade peak heights seen in Fig. 5.6 (a) in the small quantum dot, and again strongly suggests electrons are pairing in spin-degenerate energy levels as they are added to the dot.

5.4 Conclusion

In this chapter, we have described Coulomb blockade spectroscopy measurements on a small quantum dot in a magnetic field applied parallel to the plane of the 2DEG. We have observed the evolution of the addition spectrum with magnetic field, and have analyzed our data in terms of the interaction of the electron spin with the magnetic field. Following this interpretation, we observe that the changes in the spin of successive ground states of the quantum dot do not occur in an alternating up/down pattern. However, we have also emphasized the limitations of this interpretation, and pointed out that it is difficult to differentiate between spin and orbital effects caused by the parallel field. It is most likely the interplay of these two that determines the magnetic field dependence of the addition spectrum. Further experiments are needed to clearly differentiate between the two: some suggestions are made in the conclusion to this thesis.

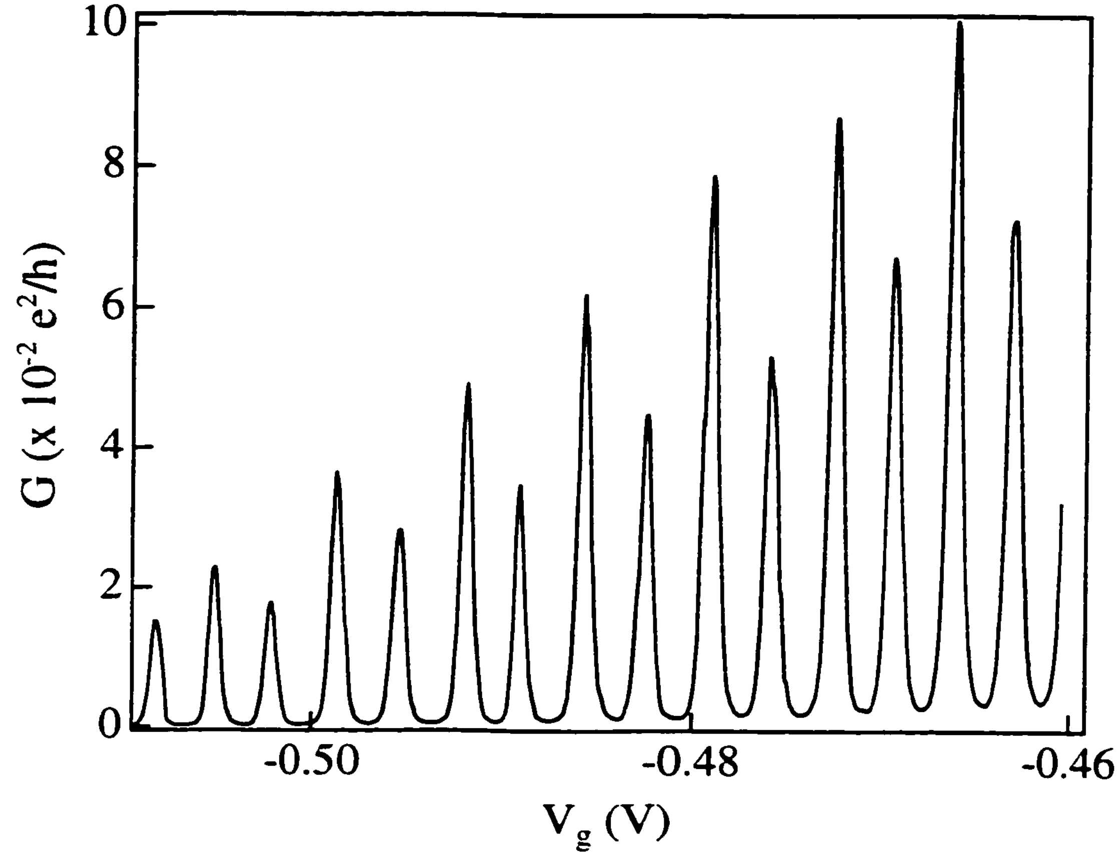

Figure 5.11 Measured differential conductance through a quantum dot vs. voltage applied on the dot sidegate. Data were taken at a dilution refrigerator base temperature of 25 mK. Coulomb blockade peaks show a strict alternation in height, indicating electron pairing and strongly suggesting that electrons are filling spin-degenerate energy levels as they enter the dot.

Chapter 6

Interactions in Coupled Quantum Dots

6.1 Introduction

In previous chapters I described experiments on single quantum dots, which have been shown to behave in many respects as "artificial atoms." In this chapter, I describe measurements on a device consisting of two coupled quantum dots, known as an "artificial molecule." In particular, Coulomb blockade spectroscopy measurements in a magnetic field are used to study the interactions between two dots. The double dot provides the simplest system for studying quantum dot interactions, which are both of intrinsic physical interest and important for proposed applications. Multiple quantum dot devices have been proposed as the building blocks of single-electron device circuits [Grabert and Devoret, 1992] as well as for the elements of a quantum computer [Bukard *et al.*, 1999; Loss and DiVincenzo, 1999; Loss and Sukhorukov, 2000]. Single-electron device circuits typically involve several quantum dots coupled by tunnel junctions through which single electrons can be controllably passed. The circuit operation depends critically on the interplay between interdot coupling and charge quantization on the constituent dots, phenomena that are readily studied in the double dot system. One quantum computer qubit proposal is based on coupling electron spins in two interacting quantum dots; a magnetic field is used to carry out logic operations [Bukard *et al.*, 1999]. Although the field of experimental quantum computing is just beginning, understanding quantum dot interactions and their magnetic field dependence could provide an important basis for future quantum computing efforts.

In recent years, several research groups, including the Westervelt group, have studied multiple dot systems. In the most commonly studied device, two single dots share one quantum point contact which serves as an adjustable tunnel barrier between them. The strength of this barrier can be tuned to vary the strength of the coupling, or "bonding," between the atoms of the artificial molecule. This device was used in several experiments using Coulomb blockade spectroscopy to study the transition from weakly coupled to strongly interacting dots [Waugh, 1994; Waugh *et al.*, 1995; Waugh *et al.*, 1996; van der Vaart, 1995a; Crouch, 1996; Crouch *et al.*, 1997; Livermore *et al.*, 1996; Livermore, 1997]. Other experiments have used linear and nonlinear conductance measurements to investigate charging effects and the role of discrete levels in the dots [van der Vaart, 1995a; van der Vaart *et al.*, 1995b; Blick *et al.*, 1996; Dixon, *et al.*, 1996a,b; Dixon, 1998]. Illumination of a double dot device by radiation has been used to study manifestations of photon-assisted tunneling [Oosterkamp *et al.*, 1998a; Blick *et al.*, 1995; Blick *et al.*, 1998], and magnetic field measurements have investigated the magnetization [Oosterkamp *et al.*, 1998b] and quantum Hall regime behaviour [Livermore *et al.*, 1999a,b] of a series double dot. Other coupled quantum dot configurations have been studied, including parallel dot systems [Molenkamp, 1995; Adourian *et al.*, 1996a, 1999; Adourian, 1996b; Dixon, 1998] and configurations for single-electron capacitance spectroscopy [Brodsky *et al.*, 2000].

In this chapter, I present Coulomb blockade spectroscopy measurements in a magnetic field on two coupled quantum dots in series. Previous work has examined the strong field, quantum Hall regime behavior of quantum dot interactions where transport occurs via edge states in the dots [Livermore *et al.*, 1999a,b]. In contrast, these experiments study interactions in the complementary regime where the relatively weak magnetic field, ranging from $B = 0$ T to $B = 400$ mT (filling factors $\nu \geq 31$), can be treated as a perturbation which induces mesoscopic fluctuations in the interdot interactions and double dot ground state energy. Such fluctuations are ubiquitous in mesoscopic systems but have not previously been studied in a double quantum dot. Thus the magnetic field dependence of interdot interactions provides a means of characterizing the importance of mesoscopic fluctuations for coupled dot applications. The double dot device is first described. Then the theory of double dots is discussed and its key features illustrated with data from my device, in particular the manner in which the strength of the interdot interactions can be accessed experimentally. Data illustrating how interactions are affected by a magnetic field are then presented. The magnetic field dependence of the interactions is studied over the full range of interdot conductance G_{int} values from $G_{int} \approx 0$ to $G_{int} = 2e^2/h = G_Q$, the conductance quantum. The data are explained by considering the effects of the magnetic field on the double dot wavefunctions.

6.2 Double Dot Device

Figure 6.1 (a) shows a scanning electron microscope photograph of the device, consisting of two quantum dots in series defined electrostatically by metal gates using the methods described in Chapter 3. The wafer used for this device contains a 2DEG located 57 nm beneath the surface with a mobility of 450,000 cm^2/Vs. The two quantum dots are lithographically identical, with dimensions of 500 x 500 nm^2. The actual dot dimensions are estimated to be 300 x 300 nm^2 taking into account the depletion boundary of the confining gates. The sheet density is 3 x $10^{11}/cm^2$, corresponding to a Fermi energy ≈ 11 meV. Each dot contains ≈ 270 electrons and the level spacing in each dot $\Delta\varepsilon \approx 80$ µeV, corresponding to a temperature of 1 K. Figure 6.1 (b) is a schematic of the gates. Each dot consists of two quantum point contacts and two confining sidegates; the dots share the central point contact. The point contact conductances can be individually tuned; the conductance of the central point contact determines the interdot coupling. Four sidegates define the sides of the quantum dots. The voltages V_{g1} and V_{g2} on the sidegates are varied to induce charge on the corresponding dot.

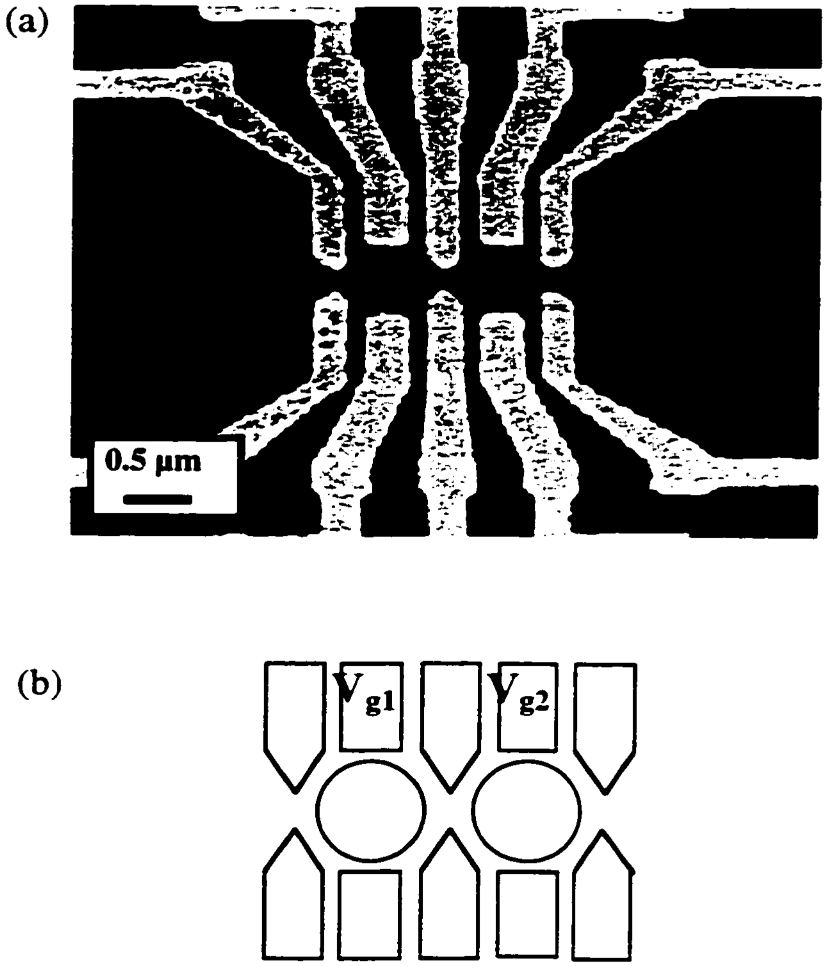

Figure 6.1 (a) SEM photograph and (b) schematic of the device. consisting of two quantum dots in series coupled together via a quantum point contact. The conductance through the center quantum point contact can be varied to determine the interdot coupling. Charge can be separately induced on each dot by varying the voltages V_{g1} and V_{g2} on the capacitively coupled sidegates.

6.3 Theory of Tunnel-Coupled Quantum Dots

Theoretical explanations have been developed for various aspects of coupled quantum dot behavior [Ruzin *et al.*, 1992; Klimeck *et al.*, 1994; Stafford and Das Sarma, 1994; Matveev *et al.*, 1996a,b; Golden and Halperin, 1996a,b; Golden and Halperin, 1997; Kaminski and Glazman, 1999]. A useful starting point for understanding the double quantum dot system is to extend the capacitive charging model for a single dot, described in Chapter 2 of this thesis, to two dots. This model is clearly too simple because it ignores interdot tunneling, but it successfully describes many features of the double dot when the interdot coupling is weak and capacitive interactions govern the device behaviour. In the opposite limit, when the two dots are strongly coupled, the system behaves as one large dot: the capacitive charging model for a single dot can be used for describing the system in this regime. After describing this model, I will discuss extensions which include interdot tunneling and describe the intermediate regimes of interdot conductance.

Figure 6.2 (a) shows the equivalent circuit diagram for the double dot system. Dots 1 and 2 are coupled to their corresponding sidegates via capacitances C_{g1} and C_{g2}, respectively. The voltages on $g_1$and g_2 are V_{g1} and V_{g2}. The remainder of the dot capacitances to the outside world are lumped into capacitances C_{o1} and C_{o2}. The only coupling between the dots is through the interdot capacitance C_{int}. The number of electrons on the two dots are N_1 and N_2, and the total number of electrons on the double dot is $N_{tot} = N_1 + N_2$. The hatched boxes in the picture represent tunnel junctions, which are quantum point contacts in our semiconductor 2DEG systems. The voltage across the series double dot, labeled V_{ds}, is taken to be zero, as all of the measurements in this chapter were taken with a very small 10 μV ac voltage across the double dot.

The procedure for applying the capacitive charging model to the double dot system is identical to that used for a single dot described in Chapter two. First, the

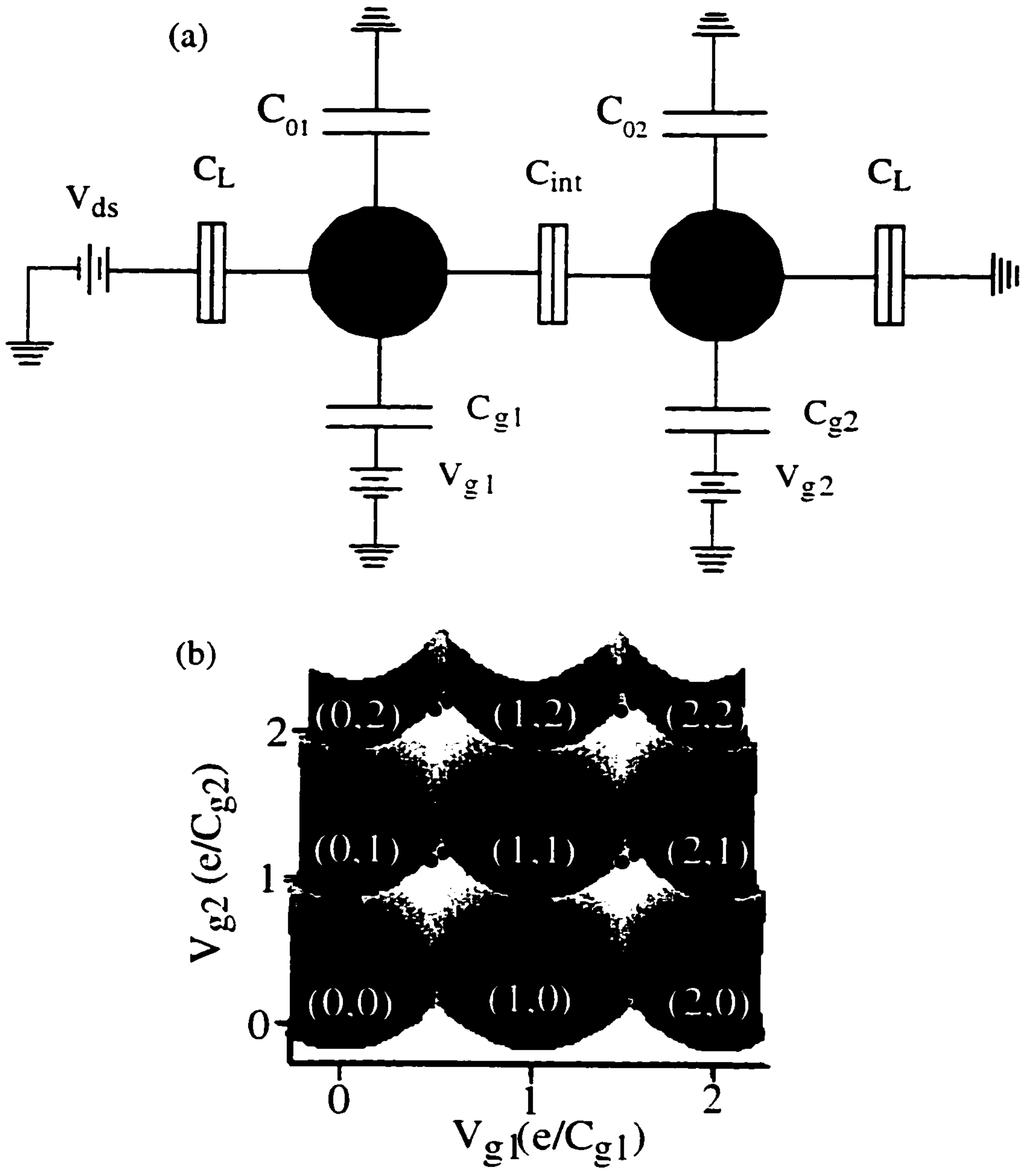

Figure 6.2 (a) Circuit model for the double quantum dot device. The dots are modeled as metal islands capacitively coupled to voltage sources. They are coupled to each other via an interdot capacitance C_{int}. (b) Electrostatic energy surface of the dot vs. the sidegate voltages V_{g1} and V_{g2}. Surface is a set of intersecting paraboloids; current can only flow through the dot at the intersection of three paraboloids, indicated by black dots in the schematic.

potentials of the two dots are calculated using electrostatics. As a consequence, the voltage drops across all capacitors are known, and the total energy E(V_{g1}, V_{g2}) is found as the sum of the energies in the capacitors minus the work done by the batteries to charge them. The energy is then minimized with respect to N_1 and N_2 to give the ground state configuration of charges (N_1, N_2) for any combination of sidegate voltages. This calculation is well described in previous theses [Waugh, 1994; Crouch, 1996; Livermore, 1997; van der Vaart, 1995a; Adourian, 1996b] so I will only summarize the principal results here and illustrate them with representative data from my measurements.

Following the above procedure, the total electrostatic energy E(V_{g1}, V_{g2}) can be shown to be:

$$E = \frac{1}{2C_\Sigma\left(1-\alpha^2\right)}\left[\left(C_{g1}V_{g1} - N_1 e\right)^2 + \left(C_{g2}V_{g2} - N_2 e\right)^2 + 2\alpha\left(C_{g1}V_{g1} - N_1 e\right)\left(C_{g2}V_{g2} - N_2 e\right)\right]$$

where $\alpha = C_{int}/C_\Sigma$, and terms independent of N_1 and N_2 have been dropped [Livermore, 1997]. Figure 6.2 (b) is a plot of the minimum energy surface of E(V_{g1}, V_{g2}) for different configurations of charges (N_1, N_2) and illustrates the concept of Coulomb blockade as manifested in the double dot system. In contrast to the minimum energy surface for a single quantum dot, which is described by a set of intesecting parabolas, the minimum energy surface for the double dot consists of a mosaic of intersecting paraboloids. The boundaries of each paraboloid define a region in which a configuration of charges (N_1,N_2) is stable. Current can only flow through the device when the Coulomb blockade is simultaneously lifted in both dots. This occurs at points on the surface where three paraboloids intersect, as indicated by the black dots in the figure. One such point is the intersection of the three paraboloids labeled (1,0), (1,1), and (0,1). If the system is initially in the configuration (1,0), an electron can tunnel on to the right dot (1,1) and off of the left dot (0,1) without energy cost, resulting in a net current of one electron through the double dot. Consequently, at configurations (V_{g1}, V_{g2}) corresponding to these points

Coulomb blockade peaks in the conductance are observed.

The regimes of double dot behaviour describable by the capacitive charging model are illustrated in Fig. 6.3 (a), which is data taken on the device of Fig. 6.1. The x-axis is the voltage V_{g1} applied to the dot 1 sidegate; the y-axis is the voltage V_{g2} applied to the dot 2 sidegate. The intensity is a gray-scale plot of the zero-bias differential conductance through the series double dot, in which light regions are high conductance, dark regions low. An array of conductance peaks is observed at values of gate voltage where the Coulomb blockade is lifted, as in Fig. 6.2 (b). Figure 6.3 (b) is the opposite limit of strongly tunnel-coupled dots. In this case, the system behaves as a single quantum dot on which the total charge $N_{tot} = N_1 + N_2$ is quantized. Each of the sidegates is coupled to the single large dot, and thus varying either V_{g1} or V_{g2} results in a series of Coulomb blockade peaks, as for a single dot. The resulting two-dimensional conductance landscape is a series of diagonal conductance stripes; between each stripe N_{tot} changes by one. Between these two regimes, physical values of C_{int} are too small to explain the observed conductance properties [Waugh, 1994; Waugh *et al.*, 1995; Waugh *et al.*, 1996; Livermore *et al.*, 1996; Livermore, 1997]. Thus, our model must be extended to include the effects of interdot tunneling.

Tunnel-coupling between the two dots complicates the above picture somewhat. Without tunneling, the energy E for the configuration (0,0) could be equal to that for the point of intersection of the paraboloids labeled (1,0), (1,1), and (0,1). Tunneling lifts this degeneracy, and thus two closely spaced Coulomb blockade peaks occur in the two-dimensional conductance diagram: one at the point of intersection of (1,0), (1,1), and (0,1), as described above, and one at the intersection of (1,0), (0,0), and (0,1). This peak splitting is indicated by the pairs of black dots in Fig. 6.2 (b). This splitting can be understood by examining Fig. 6.4, which shows the energy E as a function of $V_g = V_{g1} = V_{g2}$, i.e. for equal induced charge on both dots. This one-dimensional slice

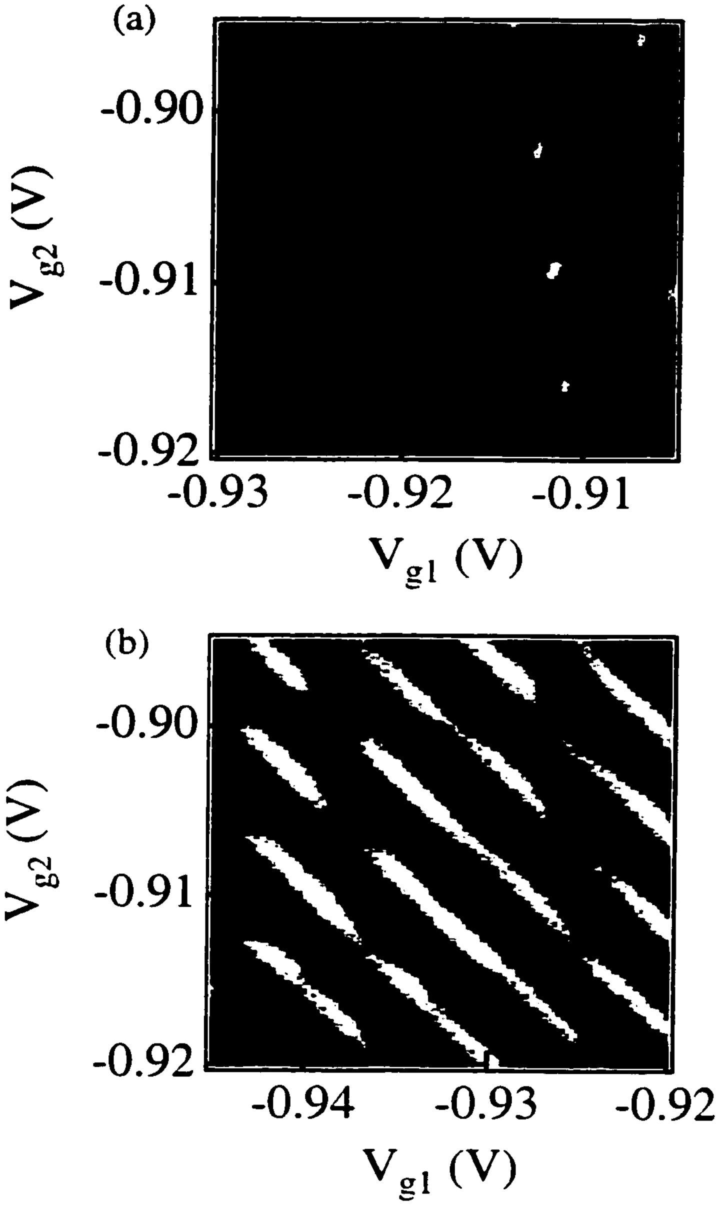

Figure 6.3 Measured differential conductance through the series double dot vs. gate voltages V_{g1} and V_{g2}. (a) In the weak interdot tunneling limit, the Coulomb blockade is lifted at an array of points in the V_{g1}-V_{g2} plane. (b) In the strong interdot tunneling limit, the two dots have become one large dot and we observe a series of single dot Coulomb blockade peaks as we ramp either V_{g1} or V_{g2}.

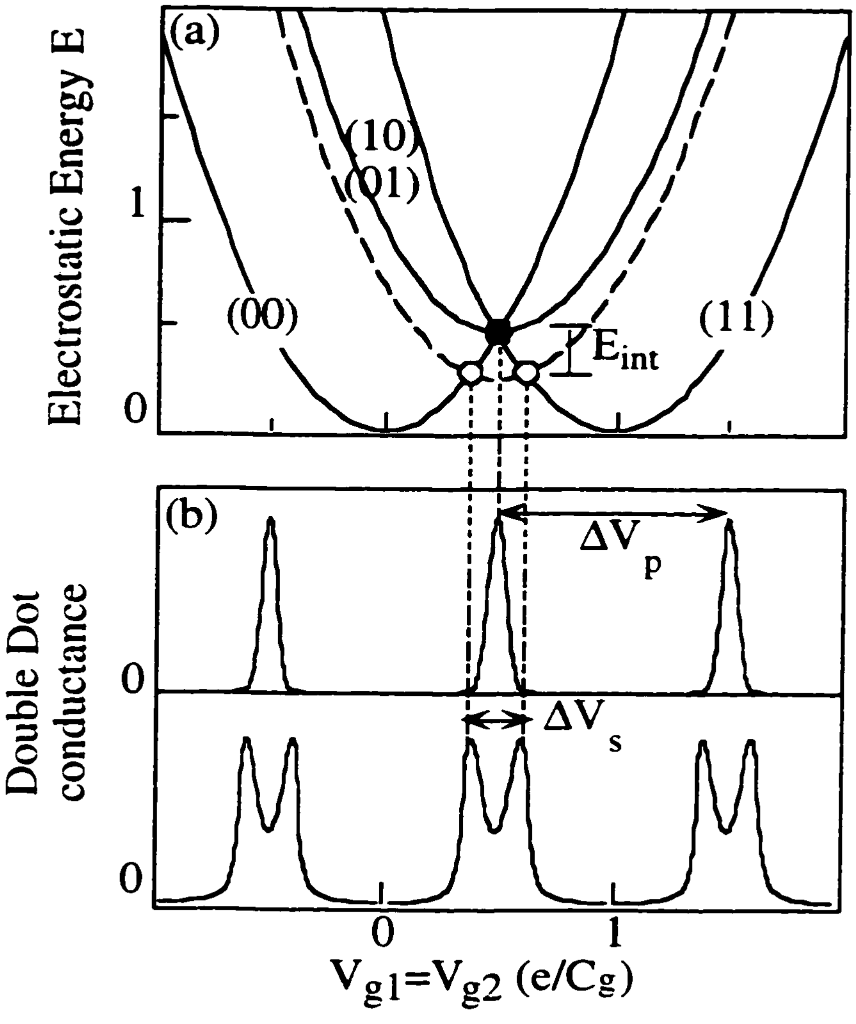

Figure 6.4 Schematic illustrating peak splitting. (a) Energy and (b) conductance are plotted vs. the voltage V_g applied to both V_{g1} and V_{g2}. For weak interdot coupling ($C_{int} \approx 0$ and $G_{int} \approx 0$), the stable total number of electrons on the dot N_{tot} is always even, due to the energy cost associated with polarized (odd) charge configurations. Current flows through the system at points where even electron number parabolas intersect, as in (b). Increasing the interdot coupling lowers the energy of odd electron number states, causing the conductance peaks to split, as in (c). Figure adapted from Waugh [1994].

through the two-dimensional energy landscape shows a set of intersecting parabolas. The lowest energy parabolas occur for an even number N_{tot} of electrons on the double dot; two such states are labeled in Fig. 6.4 (a) as (0,0) and (1,1). For an odd number of electrons, the energy minimum is higher, because such configurations correspond to polarized states of the double dot; this is shown as the parabola labeled (1,0) and (0,1) in Fig 6.4 (a). Thus, if tunneling is very weak, current only flows where two even electron number parabolas intersect. This is shown in Fig. 6.4 (b). If tunneling is increased, the energy of polarized charge configurations is lowered by the sharing of electrons between dots; the odd N_{tot} configurations are lowered in energy by the interaction energy E_{int}. Each of the single peaks splits, as depicted in Fig. 6.4 (c). Thus, the strength of interdot interactions can be characterized by the magnitude of the peak splitting along the line $V_{g1} = V_{g2}$ in the two-dimensional conductance landscape, providing a means of measuring the artificial molecule binding energy.

To account for tunneling interactions, a more complete model of the double dot is needed which incorporates the discrete energy spectra of the individual dots. In developing such a model, theorists were aided by a close analogy between single and double quantum dots. As discussed above, when interdot tunneling is increased, charge quantization on the individual dots is attenuated as electrons are shared by both dots, lowering the ground state energy. This problem is formally equivalent to the breakdown of charge quantization on a single dot as the coupling to its lead is increased. The latter problem was treated theoretically by Matveev [1995; Matveev *et al.*, 1996a,b] and is the subject of Chapter 4 of this thesis. Building on Matveev's work, Golden and Halperin [1996a,b] calculated the double dot conductance peak splitting due to interdot tunneling by mapping the system onto a single quantum dot coupled to a lead with variable tunnel conductance. In the latter work, the peak splitting is quantified by defining the fractional peak splitting F as:

$$F \equiv \frac{2\Delta V_s}{\Delta V_p}$$

where ΔV_s is the spacing in gate voltage between the two peaks in a split peak, and ΔV_p is the spacing between adjacent split peaks. F depends on the interdot tunnel conductance. A principal result of Golden and Halperin [1996a] is that F rises from a minimum value determined by capacitive interactions to a saturation value of one at an interdot tunnel conductance of $G_{int} = G_Q = 2e^2/h$. This prediction was experimentally confirmed by Livermore *et al.* [1996]. Peak splitting in a double dot is directly analogous to the breakdown of charge quantization on a single quantum dot at a dot-to-lead tunnel conductance value of G_Q, demonstrated in Chapter 4. However, it should be noted that the calculation of Golden and Halperin [1996a] is for zero applied magnetic field. As will be shown below, the situation is more complicated for a double dot in finite magnetic field.

The relationship between the peak splitting and the interdot conductance is illustrated in Fig. 6.5. The x and y-axes are again V_{g1} and V_{g2}, and the graph is a gray-scale plot of the differential conductance through the double dot. However, in Fig. 6.5 (a), the interdot conductance has been increased to a value of $G_{int} = 0.4G_Q$ by changing the voltage V_{qpcc}. Thus, instead of an array of single conductance peaks, an array of split conductance peaks is observed due to the increased interdot interaction. In addition, adjacent pairs of split peaks are joined by faint lines of conductance which are due to electrons tunneling through states in which the electron charge is shared by both dots. In Fig. 6.5 (b), the interdot conductance has been increased still further to a value of $G_{int} = 0.65G_Q$, and the peak splitting and intensity of the connecting conductance lines have correspondingly increased. Similar measurements were made by Livermore *et al.* [1996; Livermore, 1997] for the full range of G_{int} from $G_{int} \approx 0$ to $G_{int} = G_Q$; the transition from two coupled dots to one large dot was shown to be complete at $G_{int} = G_Q$, as predicted by theory.

In addition to the effects predicted by Golden and Halperin [1996a], we should

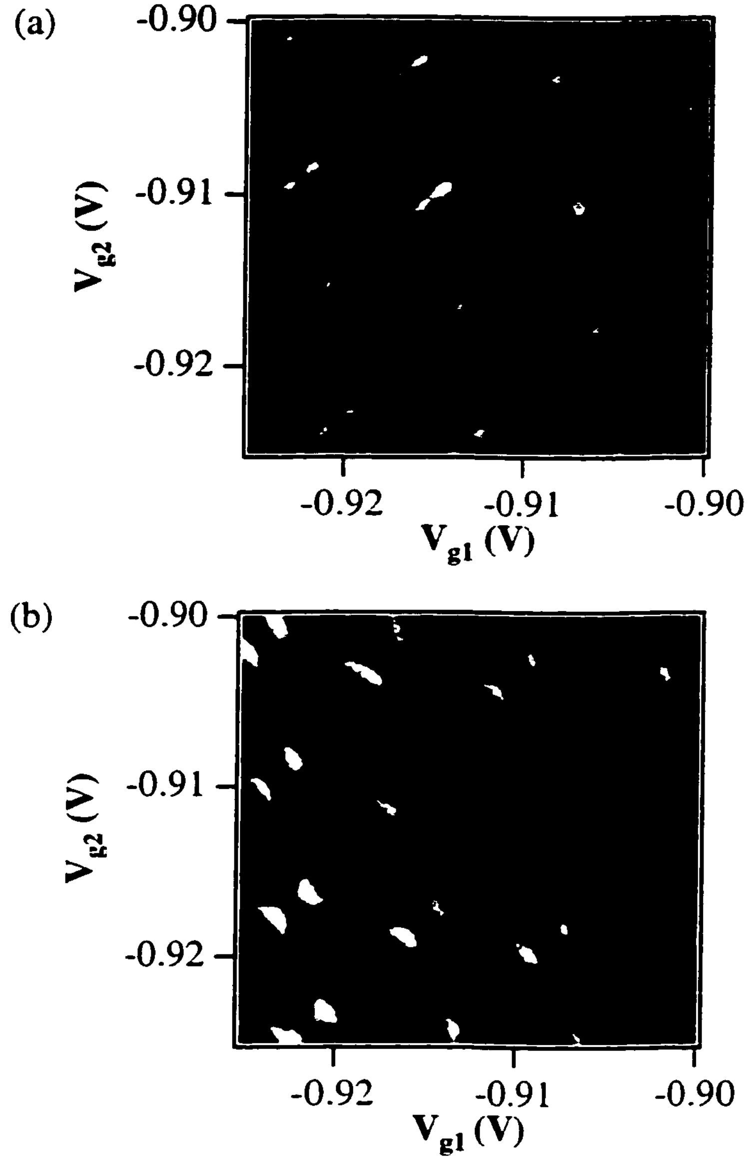

Figure 6.5 Data illustrating peak splitting as a measure of tunnel-coupling. (a) For interdot conductance $G_{int} = 0.4G_Q$ we observe pairs of peaks split due to finite interdot tunneling. (b) The interdot conductance has been raised to a value of $G_{int} = 0.65G_Q$, and the splitting within a pair of peaks has correspondingly increased. We use the peak splitting to measure the binding energy of electrons in tunnel-coupled quantum dots.

expect random fluctuations in double dot properties which depend on the interdot tunneling, for example the conductance peak heights, peak splitting, and double dot ground state energy [Kaminski and Glazman, 1999]. This is because the matrix elements t_{kp} describing tunneling between the states in the two dots are proportional to the overlap of the corresponding electron wavefunctions ψ on the two dots in the vicinity of the point contact. If the center of the point contact is located at r, k indexes levels in the left dot, and p indexes levels in the right dot, we have:

$$t_{kp} \propto \psi_k^*(r)\psi_p(r)$$

In Golden and Halperin [1996a] these matrix elements were assumed to be constant for the range of levels of interest. In reality, these matrix elements have a statistical distribution [Kaminski and Glazman, 1999] and are the cause random fluctuations in the double dot properties. These "mesoscopic fluctuations" were studied theoretically by Kaminski and Glazman [1999] by assuming a spatial distribution of electron wave functions derived from random matrix theory. The term "mesoscopic fluctuations" refers to a broad range of phenomena caused by quantum interference of phase coherent electrons in mesoscopic systems. These phenomena are typically manifested as reproducible fluctuations in various transport and thermodynamic properties as external parameters are varied, and have been studied in single quantum dots in both open [Marcus *et al.*, 1992; Chan *et al.*, 1995; Berry *et al.*, 1994a; Berry *et al.*, 1994b] and closed [Patel *et al.*, 1997; Patel *et al.*, 1998; Folk *et al.*, 1996; Huibers *et al.*, 1998; Cronenwett *et al.*, 1997, 1998; Maurer *et al.*, 1999] configurations. However, mesoscopic fluctuations have not been explicitly studied in double quantum devices, perhaps due to the difficulty of obtaining statistics in the double dot measurement setups. Such fluctuations are clearly seen in the magnetic field data to be presented next, although the data are not sufficient in quantity to make quantitative comparison with the statistical distributions predicted by theory.

6.4 Double Dot Interactions in Magnetic Field

In this section, Coulomb blockade spectroscopy measurements of the double dot in a perpendicular magnetic field are described. As discussed in the introduction, we study the double dot interactions in a magnetic field regime which is weak relative to previous experiments [Livermore *et al.*, 1999a,b]. The regime we study is from B = 0 T to B = 400 mT, corresponding to filling factors $\nu \geq 31$, where $\nu = 31$ corresponds to the sheet density of 3 x $10^{11}/\text{cm}^2$ and B = 400 mT. Thus, for much of this range the field can be thought of as a perturbation which causes random but reproducible shifts in the energy levels and corresponding wavefunctions of the individual dots. At the higher field values, electrons tunnel in to edge states in the dot and transport is in the quantum Hall regime. These low field measurements demonstrate the importance of mesoscopic fluctuations in the interactions between quantum dots. They also illustrate the magnetic field behavior of quantum dot interactions in a previously unstudied regime.

Figure 6.6 shows data illustrating phenomena probed by the introduction of a magnetic field perpendicular to the plane of the 2DEG. Fig. 6.6 (a) through (f) are plots similar to those shown in Fig. 6.4 and Fig. 6.5. The x and y-axes are the voltages V_{g1} and V_{g2} on the two sidegates and the gray scale intensity is the differential conductance through the dot. The interdot conductance is set at a value of $G_{int} = 0.8G_Q$ for these measurements, where $G_Q = 2e^2/h$, and so in each graph we observe an array of split conductance peaks corresponding to the sharing of electrons between dots. Each of the six graphs was taken at a different value of magnetic field. which are (a) 0 mT. (b) 40 mT, (c) 80 mT, (d) 130 mT, (e) 170 mT, and (f) 200 mT. These six graphs are excerpts from a longer data set, taken in the same manner but with the magnetic field raised in 10 mT increments from 0 to 200 mT. It is clear from a close examination of the data that varying the magnetic field causes variations in both the peak heights and in the peak splitting. These variations are not monotonic increasing or decreasing, but rather can fluctuate in both directions as the magnetic field is increased. This can be seen by following the

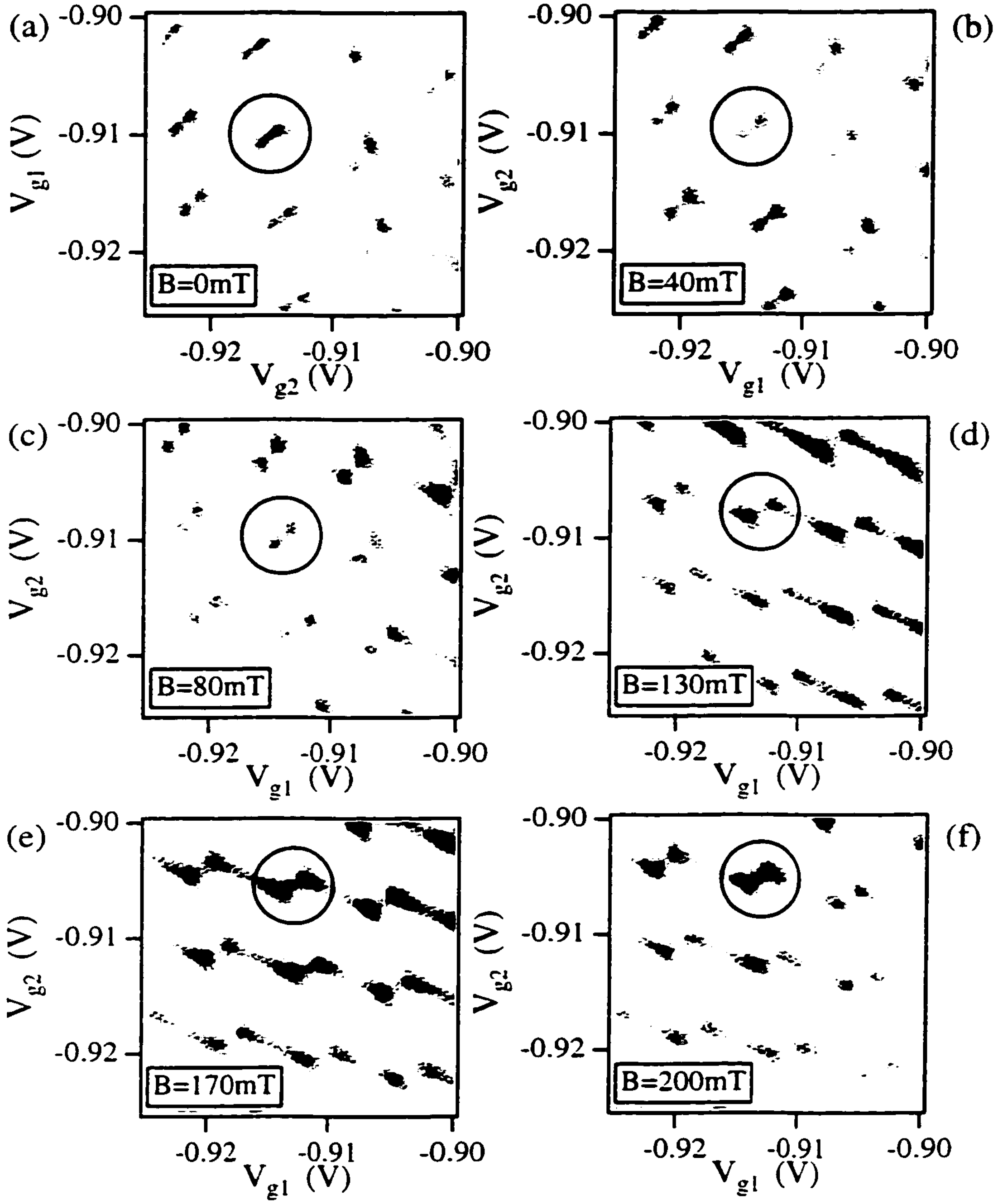

Figure 6.6 Data illustrating mesoscopic fluctuations in quantum dot interactions. Each graph is the differential conductance through the double dot vs. gate voltages V_{g1} and V_{g2} in a perpendicular magnetic field value of (a) 0 mT, (b) 40 mT, (c) 80 mT, (d) 130 mT, (e) 170 mT, and (f) 200 mT. Varying the magnetic field causes variations in both the peak heights and the peak splitting.

evolution of a single split peak throughout the series; one such peak is circled. Not all of the peak doublets shown fluctuate in exactly the same manner, though there is some correlation in the behavior of neighboring peak doublets. These variations are exactly reproducible as the field is ramped up and down.

Figure 6.6 is useful for getting an overall picture of what is happening, but the behavior can be illustrated more dramatically by focusing in on a few peak doublets and making a slightly different measurement. Figure 6.7 depicts a more focused way of looking at the same effects. The data in Fig. 6.7 (b) was taken by connecting gates 1 and 2 and ramping them together, making a diagonal cut through the two-dimensional gate voltage landscape, as indicated by the dashed line in Fig. 6.7 (a). The y-axis is $V_{g1} = V_{g2}$: the x-axis is magnetic field, which was varied from –400 mT to +400 mT. Before measuring this data, the dots were tuned such that varying $V_{g1} = V_{g2}$ would cut precisely through the center of a series of conductance peak doublets, as the white dashed line does in Fig. 6.7 (a). At zero magnetic field, a series of split conductance peaks are observed in Fig. 6.7 (b). As the magnetic field is increased, changes in both peak heights and peak splitting are observed. These changes are not monotonic: the splitting increases, then saturates, and then decreases. The peak heights also increase at first, but drop dramatically at several points. The variations are almost perfectly symmetric about B = 0 T, as expected in a 2-probe measurement. The deviations from perfect symmetry are a result of switching noise: observing this symmetry about B = 0 T provides a confirmation that the fluctuations are primarily due to the magnetic field and not caused by switching noise. The evolution of three consecutive split peaks is observed in this diagram, and it is interesting to note that neighboring split peaks evolve in a similar fashion with magnetic field.

The data of Fig. 6.7 (b) can be explained qualitatively by considering the interplay of a number of effects the magnetic field has on the double dot system. Firstly, changing the magnetic field changes the electron trajectories within the dots, which therefore

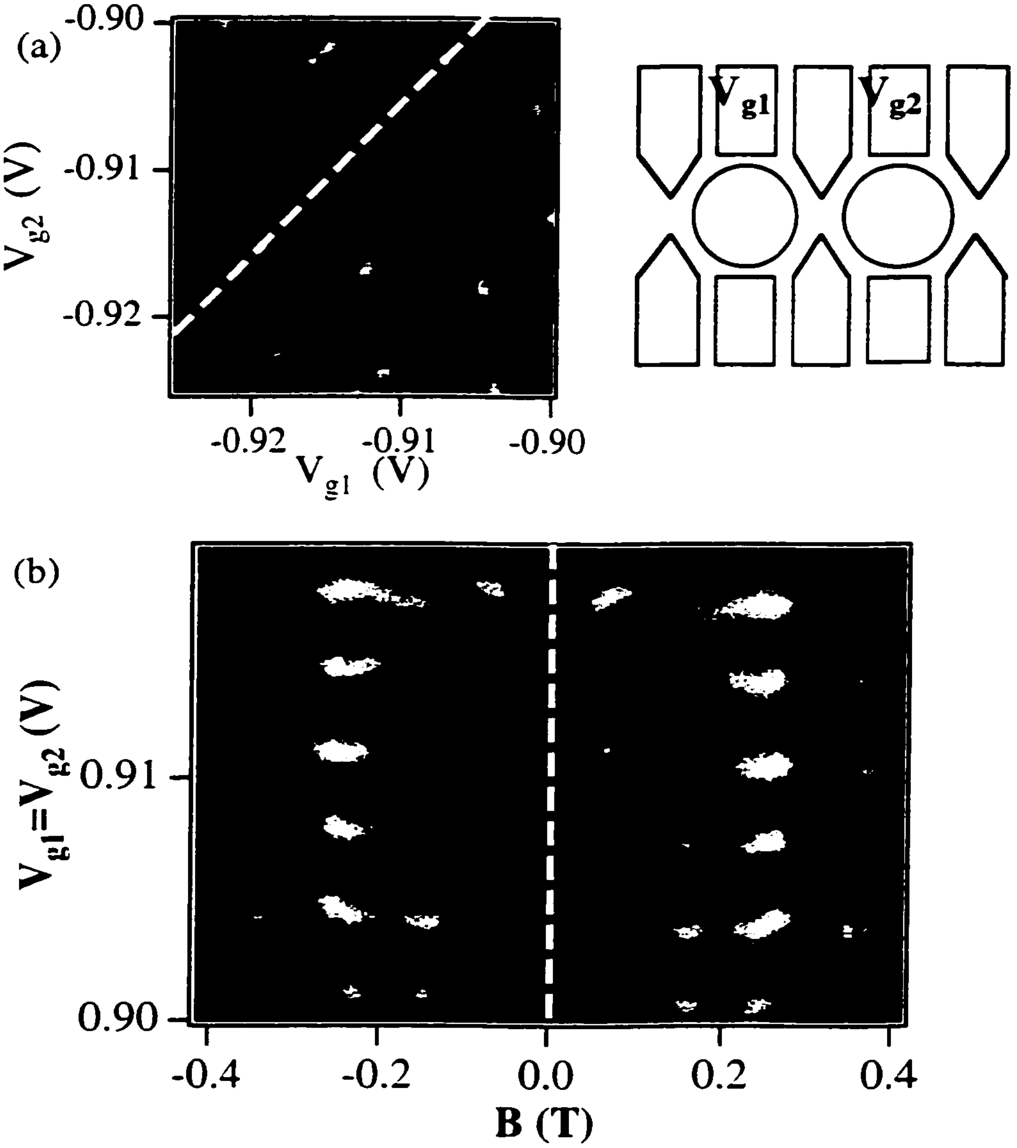

Figure 6.7 Measured fluctuations in the peak splitting. In (a) we observe an array of split peaks; dashed line indicates a diagonal cut through the data at $V_{g1} = V_{g2}$. (b) Differential conductance through the double dot vs. $V_{g1} = V_{g2}$ and magnetic field B. Dashed line at B = 0 T corresponds to the diagonal dashed line in (a). Strong fluctuations in the peak splitting and in the peak heights measured along $V_{g1} = V_{g2}$ are observed vs. magnetic field. Variations are symmetric about B = 0 T.

changes the spatial distributions of the electron wavefunctions. The peak heights depend on the degree of overlap of the electron wavefunctions in the dots and the wavefunctions in the leads; as the magnetic field is varied the overlaps change and consequently the heights of the conductance peaks vary. Secondly, changing the spatial distribution of the electron wavefunctions also changes the overlap of the wavefunctions on different dots, i.e. the interdot tunneling matrix elements. As a result, the interdot coupling and ground state energy change, and hence the peak splitting. Finally, changing the magnetic field causes shifts in the discrete energy spectra in the individual dots, which will be manifested as shifts in the positions of the peak doublets in the two-dimensional conductance landscape. This may explain the most dramatic fluctuations in the data shown in Fig. 6.7 (b). At these points, the shifts in peak doublet position are sufficient to cause the diagonal line $V_{g1} = V_{g2}$ along which the measurement is made to cut through the 2D gate voltage landscape off the side of the peak doublet, resulting in a dramatic decrease in the measured peak heights. It is interesting to note, however, that the ranges of B over which this occurs are very short.

To measure the dependence of these fluctuations on the interdot conductance G_{int}, we carried out similar measurements for a range of interdot conductance values. Figure 6.8 shows the results of these measurements. The x-axes of each of Fig. 6.8 (a) through (g) are again the magnetic field, the y-axes are the voltage $V_{g1} = V_{g2}$, and the intensity is the differential conductance through the double dot. Each of the seven graphs was taken at a different value of G_{int}, which were (a) 0.25 G_Q, (b) 0.43 G_Q, (c) 0.55 G_Q, (d) 0.75 G_Q, (e) 0.9 G_Q, (f) 0.99 G_Q, and (g) 1.15 G_Q. In (a), the interdot conductance is weak and no peak splitting is observable. However, the magnetic field still causes large variations in the peak heights, and the regions in which the peak heights drop dramatically extend over longer ranges of B than in Fig. 6.7. This is further evidence that shifts in the discrete energy levels cause these large fluctuations: at lower values of G_{int}, the widths of the peak doublets are narrower, and thus small shifts in their positions cause

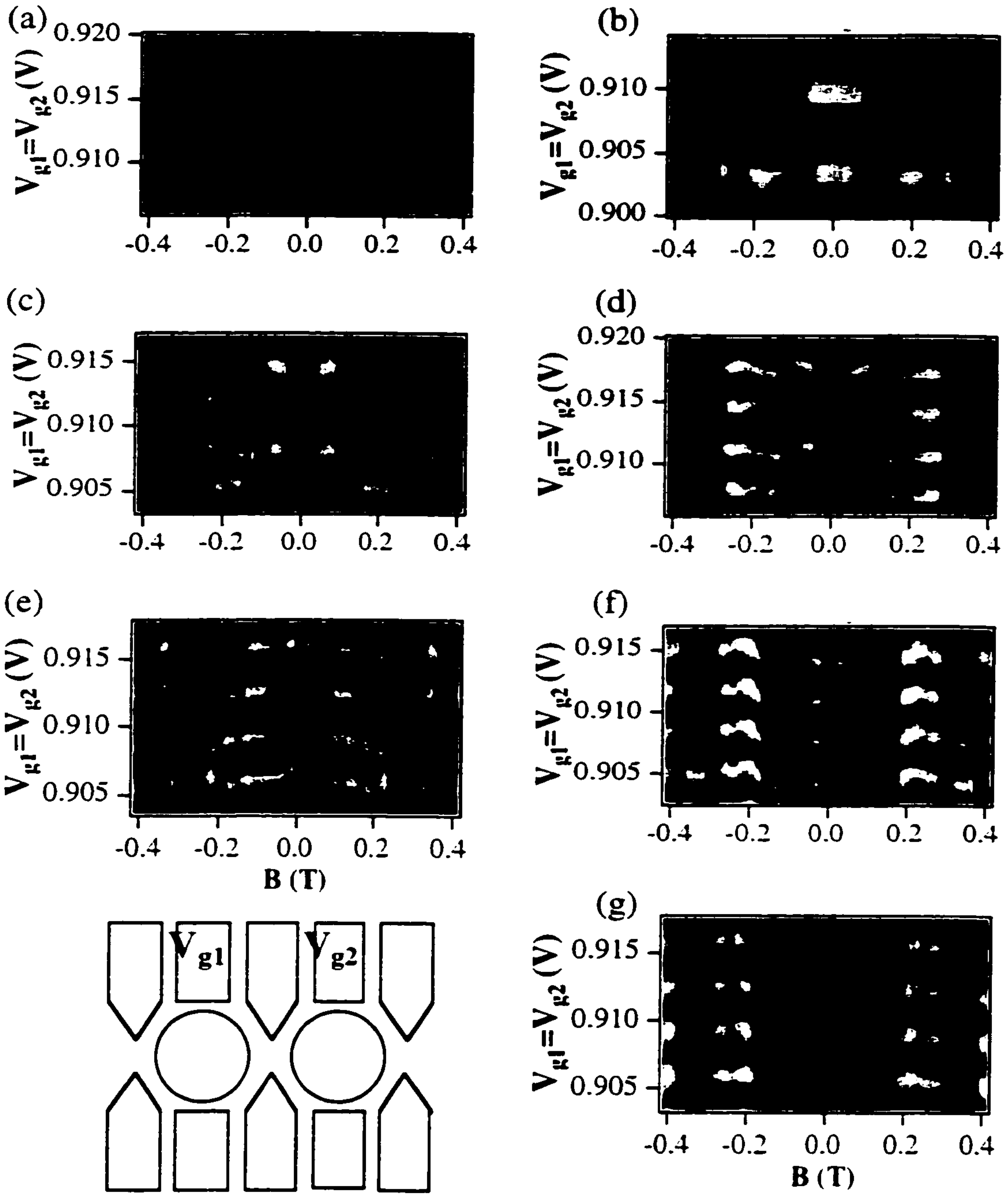

Figure 6.8 Fluctuations in interdot interactions vs. magnetic field B and interdot conductance G_{int}. Each graph shows the variation of peak height and peak splitting for $V_{g1} = V_{g2}$, for interdot conductance values of (a) 0.25 G_Q, (b) 0.43 G_Q, (c) 0.55 G_Q, (d) 0.75 G_Q, (e) 0.9 G_Q, (f) 0.99 G_Q, and (g) 1.15 G_Q. As the interdot coupling is increased the peaks split from single peaks in (a) to double peaks with half the period in (f), as predicted by theory for the case where $G_{int} = G_Q$.

fects. As the interdot coupling is increased in (b), the peak widths appear to broaden in the vertical direction; this is due to an increase in peak splitting that is still too small to resolve. As the interdot coupling is increased in (c) through (e), the split peaks become resolvable and the fluctuations in position become more striking. Finally at a value of $G_{int} = G_Q$, in Fig. 6.8 (f), the period of the peaks in the vertical direction has doubled, indicating the two dots have merged into one large dot with twice the area. This behavior is maintained as the interdot coupling is increased further in Fig. 6.8 (g), as predicted by theory. This is similar to the case for zero magnetic field, but is in distinct contrast to the case for a double quantum dot in a strong magnetic field, where the transition to a single dot occurs at an interdot tunnel-coupling of e^2/h.

The data of Fig. 6.8 illustrate other aspects of mesoscopic fluctuations in the coupled dot system as well. If the effects of split peak motion can be ignored, i.e. if we are in fact measuring the true peak splitting for the double dot as a function of magnetic field and G_{int}, then Fig. 6.8 depicts the direct measure of mesoscopic fluctuations in the ground state energy of a double quantum dot. Equivalently, these data depict mesoscopic fluctuations in the binding energy of the artificial molecule. Figs. 6.8 (c) and (d) illustrate this most strikingly, as the peak splitting is visible throughout the entire range of magnetic field. In reality, as discussed above, the motion of split peaks may be a factor in explaining the data, but it is not possible to determine the extent of its influence from this data.

6.5 Conclusion

In this chapter, measurements on a double quantum dot device in a perpendicular magnetic field have been described. These measurements are the first to systematically investigate quantum dot interactions in the weak to moderate magnetic field regime. The strength of the interdot interactions have been determined via measurements of the double dot conductance peak splitting. The interactions between the two dots, and hence the double dot ground state energy, have been shown to fluctuate dramatically as the magnetic field is varied. These mesoscopic fluctuations are explained by the effect of the magnetic field on the discrete energy levels and corresponding wavefunctions in the individual dots. The dependence of these fluctuations on the interdot tunnel barrier height has also been studied. These measurements provide insight into the dependence of quantum dot interactions on the purely mesoscopic effect of quantum interference of coherent electron waves, and hence illustrate the need to consider such effects when designing applications for multiple quantum dots.

Chapter 7

Magnetoconductance of an Open Electron Resonator

7.1 Introduction

In this chapter, I describe experiments on a different type of semiconductor nanostructure: an electron resonator. This is a small 2DEG cavity into which electrons can be injected via a quantum point contact. In contrast to the studies of quantum dots described previously, the resonator is an "open" structure, meaning it is coupled to the surrounding 2DEG regions by relatively wide conducting channels in which electron transport is also two-dimensional. Thus, whereas in quantum dots the effects of charge quantization and a discrete energy spectrum dominate the device behavior, in the resonator it is the interference of electron waves that is paramount. Transport through the resonator can be characterized by a semiclassical picture which assumes electrons carry phase while moving along classical trajectories, analogous to light rays in geometrical optics. For this reason, the resonator structure falls under the rubric of "electron optics" devices [Spector *et al.*, 1990a,b,c; Spector *et al.*, 1992]. The resonator is small enough that transport through it occurs fully in the ballistic regime, i.e. the device dimensions are much less than the mean free path for elastic scattering. Thus, the geometry of the resonator is the principal determinant of its transport properties.

Electron resonators were first studied in the Westervelt group by Jordan Katine [Katine, 1996; Katine *et al.*, 1997]. In this work, a resonator cavity was created by fabricating a quantum point contact adjacent to a reflecting gate in the shape of an arc;

the arc's focal point is the point contact center. Both the reflector and the point contact were formed by energizing metal gates on the surface of a 2DEG heterostructure. Because the reflector is dynamically defined in this way, its distance from the point contact, and hence the size of the resonator cavity, can be changed by varying the reflector gate voltage. The principal measurement done was of the conductance through the quantum point contact vs. the reflector gate position, which displayed a striking series of periodic peaks as the reflector was moved closer to the point contact. Each conductance peak occurred when the reflector gate had moved a distance of $\lambda_f/2$, where λ_f was the Fermi wavelength of electrons in the 2DEG. This behaviour could be explained by a simple picture in which electron waves interfere constructively at the point contact position each time the pathlength of their trajectories changed by a Fermi wavelength, similar to an optical Fabry-Perot interferometer. Theoretical work was able to explain these observations as well as make predictions on further fine structure that might be observed in the resonator conductance properties [Katine *et al.*, 1997; Edwards *et al.*, 1998].

In this chapter, I describe measurements on a similar electron resonator which extend this work to the study of the magnetic field properties of the resonator. The conductance peak behavior is reproduced and the dependence of the peaks on a perpendicular magnetic field is systematically studied. Many effects are observed in the resulting two-dimensional conductance landscape of resonator position and magnetic field, the most dramatic of which is a phase-shift in the positions of conductance peaks as the magnetic field is increased. This shift can be understood as a consequence of the combined effects of electron trajectory bending by the magnetic field and the Aharonov-Bohm phase shift. Indeed, the Aharonov-Bohm phase shift is shown to be an essential component in the explanation, and thus these measurements provide an unusual experimental demonstration of the Aharonov-Bohm phase shift in an open system. Other features in the data are also explained by this picture. In addition, I present data which illustrates the dependence of the conductance peaks on the number of transmitting modes in the point contact.

7.2 Device description and operation

Figure 7.1 shows a scanning electron microscope photograph of the device, which consists of a single quantum point contact and a reflecting gate formed on the surface of a GaAs/AlGaAs heterostructure using electron-beam lithography and Cr-Au metallization, as described in chapter 3. The heterostructure wafer used for these experiments contains a 2DEG 57 nm beneath the surface with a mobility of 450,000 cm^2/Vs. The sheet density is $3 \times 10^{11}/cm^2$, and the corresponding Fermi wavelength is 46 nm. The point contact forms one side of the resonator cavity, and the reflecting gate forms the other side. Lithographically, the radius of curvature of the resonator is 800 nm, and the point contact is located 850 nm from the resonator arc. This was chosen so that at depletion the center of the quantum point contact would lie at the focal point of the reflector arc, allowing for a 50 nm depletion length from the resonator. The arc is circular in order to reflect electron waves injected from the pont contact back at the point contact. Thus, injected electrons can undergo many reflections within the cavity before they eventually escape through the open sides of the resonator. Ohmic contacts to the 2DEG are located outside of the cavity on both sides of the point contact. A 10 μV ac bias was placed across the point contact and the lockin techniques described in Chapter 3 used to measured the conductance through the contact as the reflector gate voltage and magnetic field were varied. The measurements described in this chapter were done in a dilution refrigerator at temperatures ranging from a base temperature of 25 mK to 500 mK.

Figure 7.2 shows a characteristic measurement done on one of the resonators I studied. This graph is the differential conductance through the point contact vs. the voltage applied to the reflector gate. Figure 7.2 (a) was taken at a temperature of 500 mK, Fig. 7.2 (b) at a dilution refrigerator temperature of 25 mK. Both traces were taken on the same device. The point contact was tuned to be conducting in the tunneling

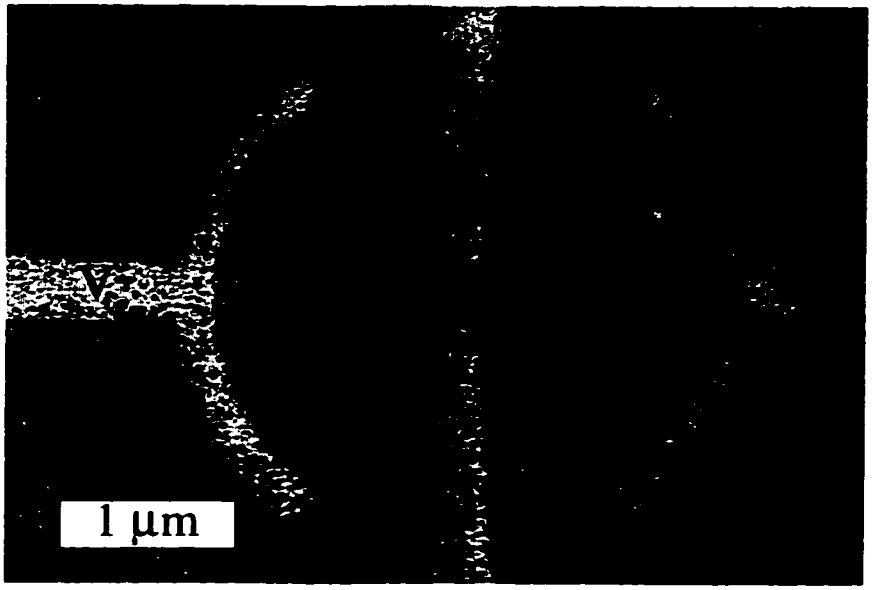

Figure 7.1 Scanning electron microscope photograph of the electron resonator device. The resonator consists of a single quantum point contact and a reflecting gate defined electrostatically in a 2DEG heterostructure. The voltage V_g on the resonator gate can be varied to change the size of the cavity and hence of the pathlengths of electron trajectories in the resonator.

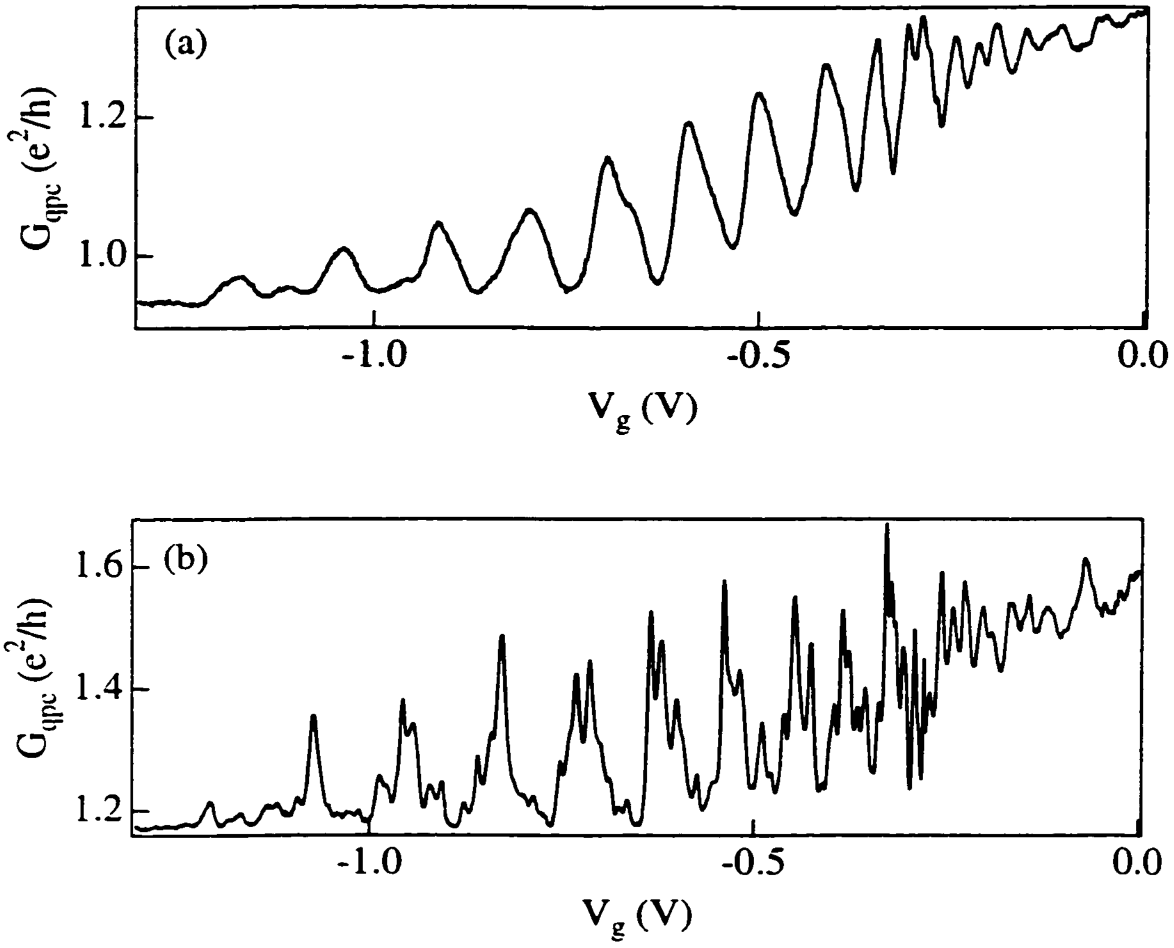

Figure 7.2 Measured differential conductance through the point contact as a function of reflector gate voltage V_g at (a) 500 mK and (b) 25 mK. In (a), after V_g is ramped to depletion, a series of periodic conductance peaks is observed due to constructive interference of electron waves at the point contact. The period of the peaks corresponds to a distance moved by the reflector gate of $\lambda_f/2$. (b) At 25 mK, a similar pattern is observed; however, fine structure on the primary peaks can be resolved which may be due to more complex modes in the resonator.

ductance value of $G_{qpc} = 1.35\ e^2/h$. In Fig. 7.2 (a), as the reflector gate voltage V_g is ramped down from zero, small modulations of the point contact conductance are observed until full depletion of the 2DEG beneath the reflector gate is achieved at a $V_g \sim -0.3V$. As V_g is ramped down further, large peaks in the the point contact conductance are observed at regular intervals. The spacing of the peaks increases as V_g becomes more negative. Despite this trend, the period is linear in reflector gate position. The discrepancy is due to the nonlinear mapping between V_g and the actual position of the reflector electrostatic boundary: as V_g becomes more negative, a progressively greater change in V_g is necessary to move the reflector electrostatic boundary a fixed distance in the 2DEG layer. In fact we see that the period is approximately constant over the reflector gate voltage range -0.4V to -1V. The distance between peaks must correspond to a reflector gate motion of $\lambda_f/2 = 23$ nm.

Comparing Fig. 7.2 (a) and (b), we observe a marked temperature dependence in the fine structure of the resonator condutance peaks. The primary period observed in Fig. 7.2 (a) is evident in Fig. 7.2 (b) as well. However, in (b) the primary conductance peaks are modulated by additional, smaller peaks with smaller spacings. Theory predicts the nature of the conductance peaks depends on the specific cavity modes accessed [Katine *et al.*, 1997]. The primary peaks are associated with the simplest electron trajectories emanating straight out from the point contact and reflecting straight back. The secondary conductance peaks may be associated with more complex electron trajectories and modes in the resonator that are predicted to have a smaller amplitude and period. Some identification of such secondary modes was made in Katine *et al.* [1997]. We do not attempt to make such an identification here, but merely note that the fine structure is completely reproducible and is also due to electron trajectories that interfere constructively at the quantum point contact. At higher temperatures, thermal smearing washes out the fine structure and only the primary peaks are resolvable.

The difficulty of mapping the secondary structure on to theoretically predicted cavity modes is illustrated in Fig. 7.3. Here I show two traces of the conductance through two distinct but lithographically identical devices taken at a dilution refrigerator temperature of 25 mK. Fig. 7.3 (a) is identical to Fig. 7.2 (b), whereas Fig. 7.3 (b) is from a different devivce. In both cases, the primary conductance peaks are clearly evident. However, the fine structure differs markedly in both devices. This variation is due to variations in the impurity potential of the resonator as well as small lithographic variations which bend electron trajectories in unique ways in each device. However, it should be noted that the primary conductance peaks are a very robust effect, and were observed in six different devices.

7.3 Magnetoconductance Measurements

Figure 7.4 through Fig. 7.6 show the principal result of this chapter, the magnetic field dependence of the resonator conductance peaks. Each of these data sets is the differential conductance through the point contact of an electron resonator, as a function of the reflector gate voltage V_g on the y-axis and a magnetic field B applied perpendicular to the plane of the 2DEG on the x-axis. Each data set was taken on a different resonator device at a dilution refrigerator temperature of 25 mK. Light regions correspond to high conductance, dark regions to low. At $B = 0$ T, we observe the familiar set of primary conductance peaks modulated by the finer secondary peaks. Again, the fine structure varies from one to device to the next, whereas the period of the primary peaks is the same in all devices. The most striking effect in all three cases is a downward curvature in the peak positions as the magnetic field is increased. The curvature is slight at first, but becomes more pronounced at higher magnetic fields. The radius of curvature varies at different field values, but is approximately the same for all peaks at any given field value.

To explain the curvature of the conductance peak positions in Figs. 7.4 through Fig. 7.6, we first consider bending of the electron trajectories by the magnetic field. The electron path we consider is the simple straight out and back path responsible for the

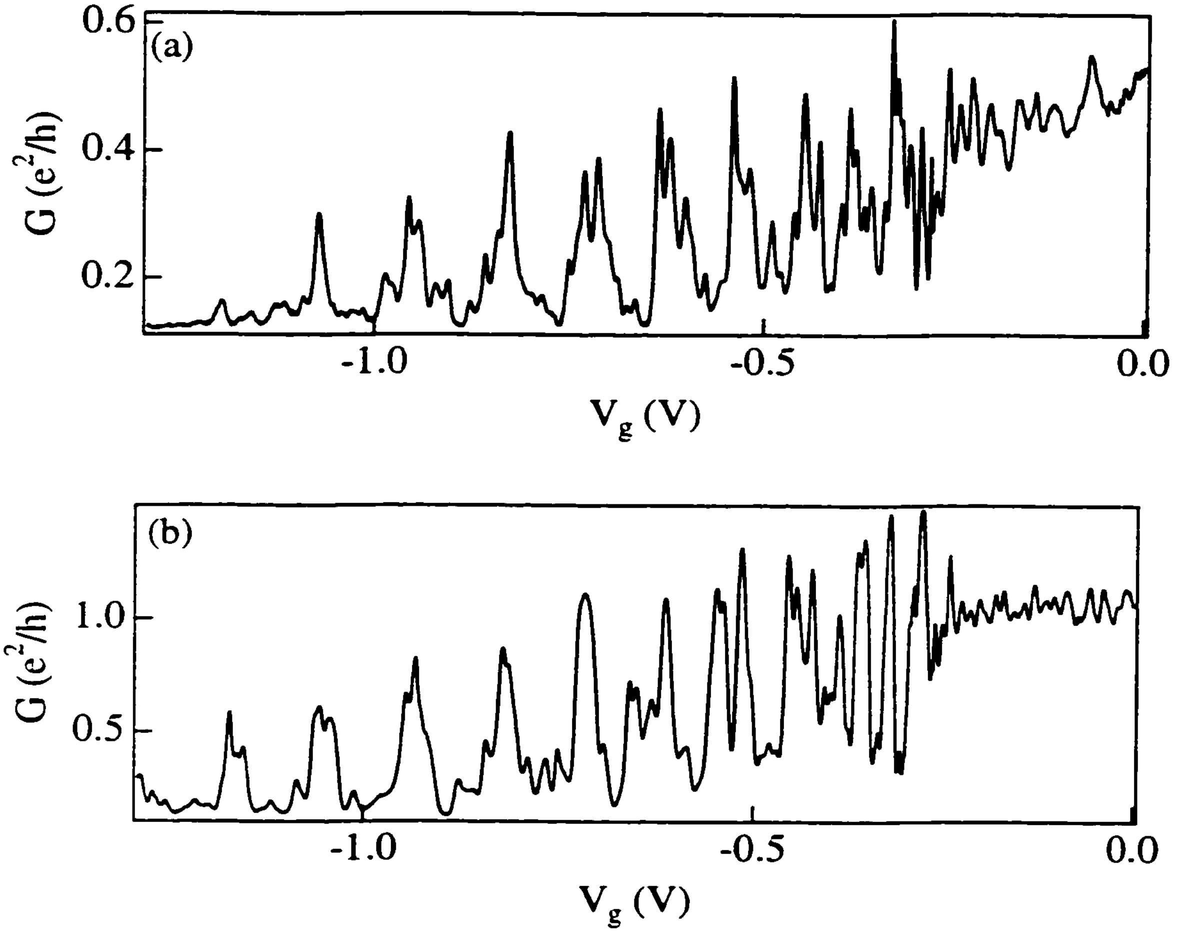

Figure 7.3 (a) and (b) Measured differential conductance through two different resonators. In both traces the primary conductance peaks are observed with the same period. However, the fine structure varies markedly from one device to the next.

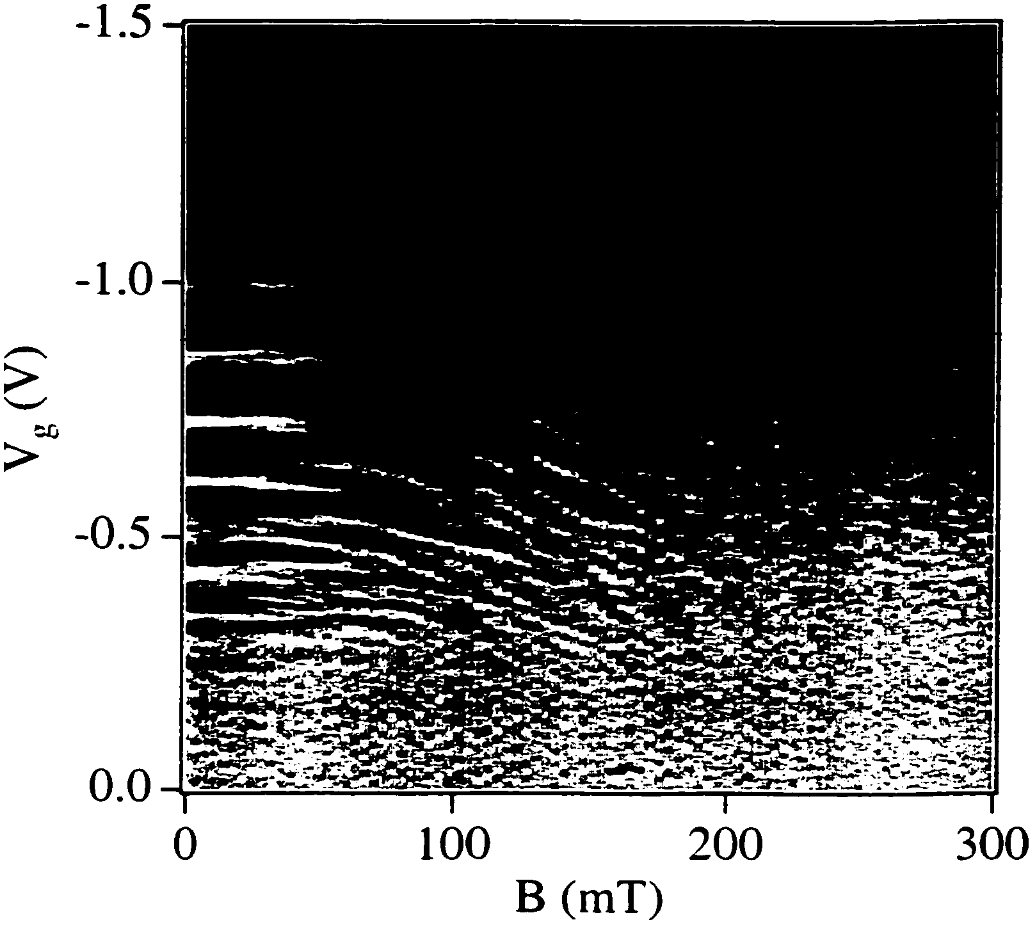

Figure 7.4 Measured differential conductance through the resonator as a function of reflector gate voltage V_g and magnetic field B. At B = 0 T, the familiar series of conductance peaks is observed. As B is raised, the peak positions curve.

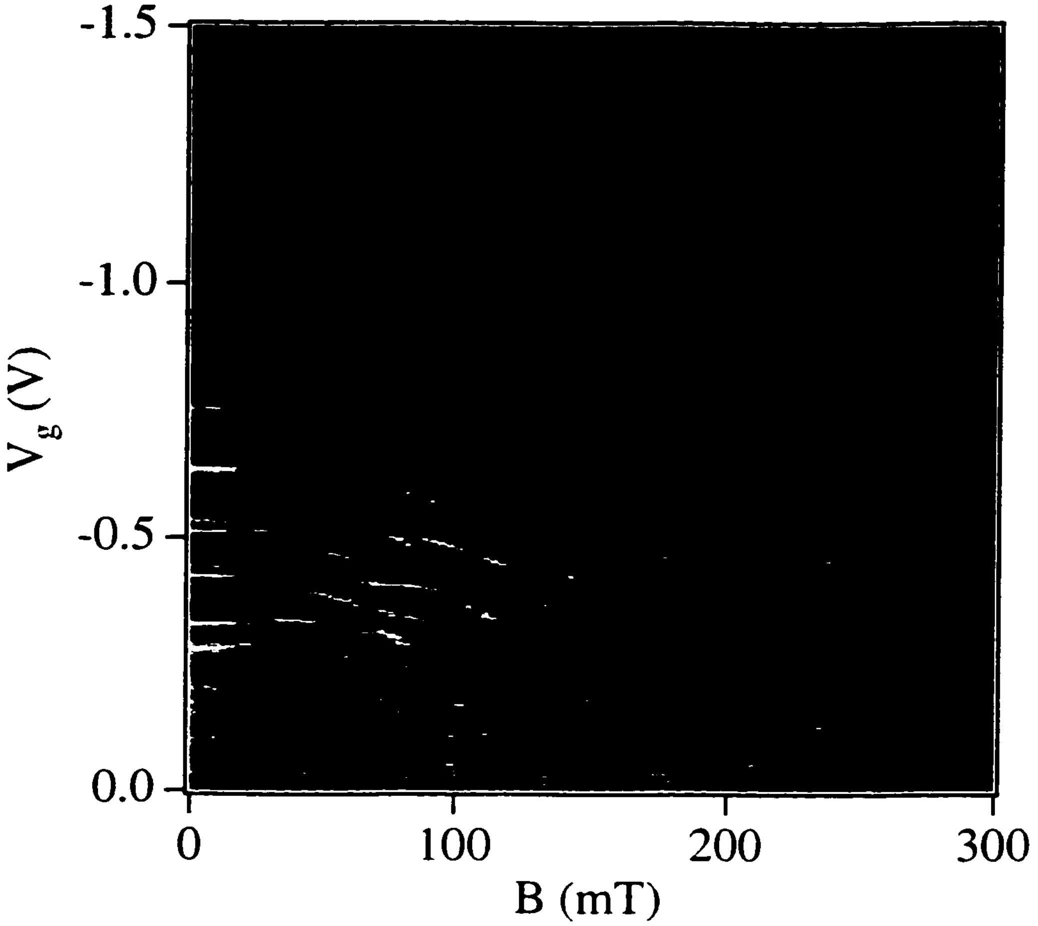

Figure 7.5 Same as Fig. 7.4, but for a different device. The motion of the primary peaks with magnetic field follows the same overall pattern as for Fig. 7.4, though the details of the secondary structure vary.

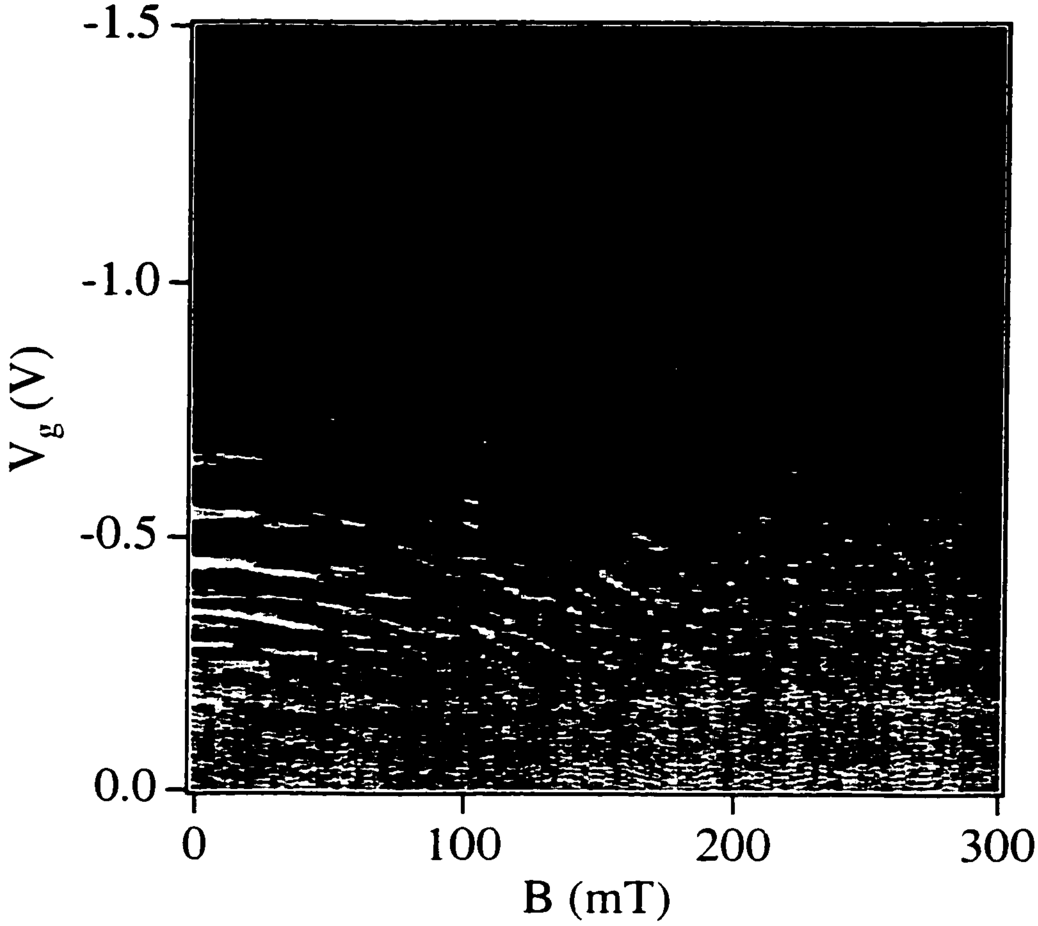

Figure 7.6 Same as Figs. 7.4 and 7.5 but for a third device. The motion of the primary peaks with magnetic field follows the same overall pattern as for Fig. 7.4, though the details of the secondary structure vary.

primary conductance peaks, which occur when backscattered electron trajectories interfere constructively at the quantum point contact. A magnetic field bends these linear segments into arcs with a radius of curvature given by the cyclotron radius r_c:

$$r_c = \frac{m^* v_f}{eB}$$

where $m^* = 0.067\ m_e$ is the effective mass of electrons in GaAs and $v_f = 2.5 \times 10^7$ cm/s is the Fermi velocity of electrons in this heterostructure. This bending changes the path length of the electron trajectories, and thus the combination of magnetic field and reflector gate position determines the overall path length. The change in path length for a reflector distance y is given by:

$$\Delta l = 4r_c \arcsin\left(\frac{y}{2r_c}\right) - 2y$$

In general, increasing the magnetic field increases path lengths, and so we would expect conductance peak positions to shift upward as we increase field in Fig. 7.4, as the reflector gate position is shifted closer to the quantum point contact to compensate for the effect of the magnetic field. In fact, this is the exact opposite of what we observe.

To explain our data, we must introduce the Aharonov-Bohm contribution to the phase in our calculation. As the linear trajectories are bent into arcs by the magnetic field, the electron path encloses an area A that increases with magnetic field. This area is given by:

$$A(r_c) = r_c^2\left(\theta - 2\cos\left(\frac{\theta}{2}\right)\sin\left(\frac{\theta}{2}\right)\right)$$

where:

$$\theta = 2\arcsin\left(\frac{y}{2r_c}\right)$$

The flux enclosed by this area is the product of A and the magnetic field; the number of flux quanta threading A determines the Aharonov-Bohm phase shift.

We can determine the effect of the net phase shift of the path length change due to trajectory bending and the Aharonov-Bohm shift by calculating the total phase accumulated in a roundtrip path. This is given by:

$$\phi_{total} = 2\pi\left(\frac{2r_c\theta}{\lambda_f} - \frac{A(r_c)B}{\Phi_0}\right)$$

Where $\Phi_0 = 4.14 \times 10^{-15}$ T m^2 is the flux quantum. In Fig. 7.7, we plot this expression (modulo 2π) for reflector gate distances ranging from 600 nm to 825 nm, and for magnetic field values ranging from 0 to 300 mT. Only lines of constant phase are plotted, which correspond to the conductance peak positions. The scaling of the x and y axes has been chosen to correspond to that of the data sets shown in Fig. 7.4 through Fig. 7.6. As can be seen by comparing the two figures, the simple expression above reproduces the overall peak motion in Fig. 7.4 remarkably well, especially in the regime of smaller reflector gate distances where the effect of the reflector gate voltage on the cavity length is approximately linear.

To illustrate the necessity of including the Aharonov-Bohm contribution to the phase shift, Fig. 7.8 plots the total phase accumulated solely due to the path length changes induced by the magnetic field trajectory bending, i.e. without Aharonov-Bohm. The same x and y-axes were used as for Fig. 7.7. In this case, the lines of constant phase (corresponding to the conductance peak positions in Fig. 7.4) evolve upward as the field is raised. This is in the opposite direction to that observed in the data, but in agreement with the qualitative argument given previously. Thus, we conclude that it is essential to include the Aharonov-Bohm contribution in our calculation. This is compelling evidence that we are observing the Aharonov-Bohm phase shift in an open system.

Several other features in the data of Figs. 7.4 through 7.6 are also of interest. As the field is raised from zero, the amplitudes of the primary peaks diminish, due to the bending of electron paths away from the reflector gate. Eventually, this trajectory bending will cause all electrons entering the cavity to be bent out of the resonator without reaching the reflector gate, and all conductance peaks should disappear. In Fig. 7.4, this

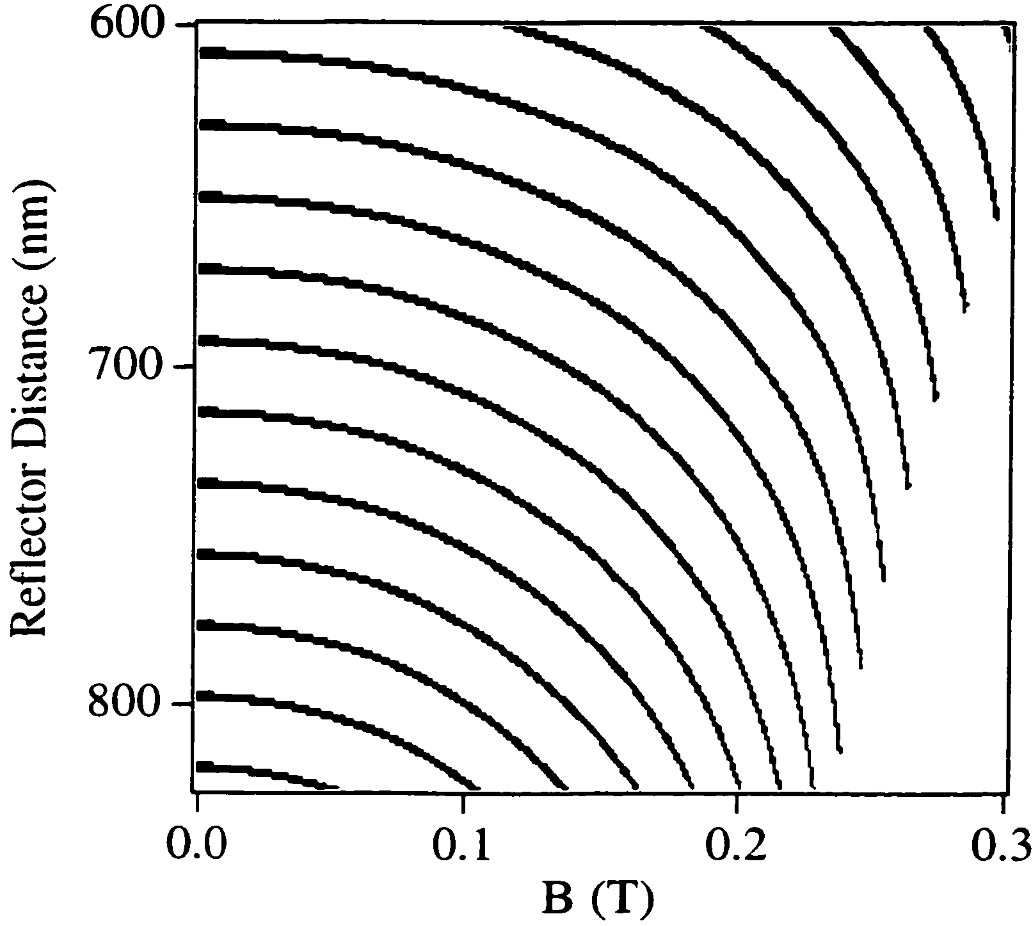

Figure 7.7 Calculated accumulated phase vs. reflector gate position and magnetic field B. Lines are lines of constant phase, corresponding to conductance peak positions. Total phase is the sum of the geometric contribution due to trajectory bending and the Aharonov-Bohm contribution. The evolution of these lines reproduces the peak motion observed in the data.

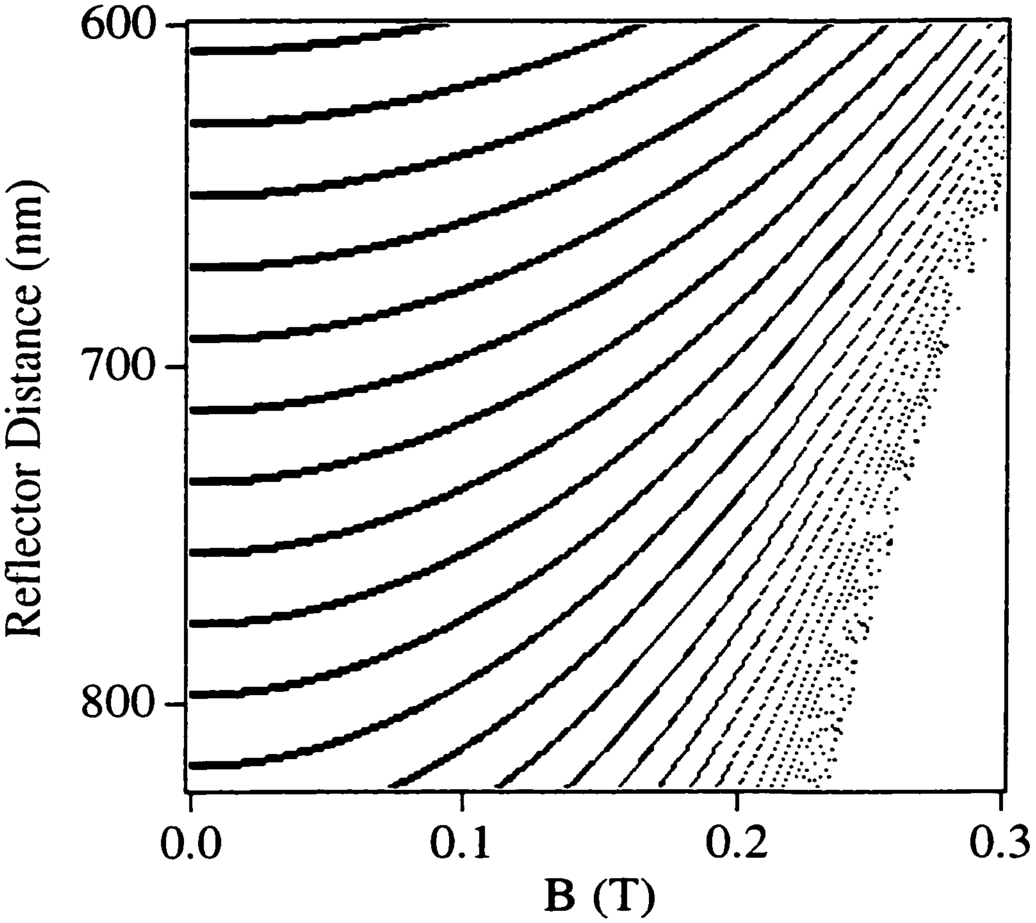

Figure 7.8 Calculated accumulated phase due only to the geometric contribution from trajectory bending. Lines are lines of constant phase, corresponding to conductance peak positions. These lines evolve in the direction opposite to that observed in the data, indicating the importance of the Aharonov-Bohm contribution.

occurs at B ≈ 150 mT. This field value corresponds to a cyclotron radius of 645 nm, which is sufficiently small for most electron trajectories to be bent entirely out of the cavity at low values of reflector gate voltage. We would expect for the necessary radius to decrease as the size of the cavity decreases, and thus for the peak structure to vanish at higher values of magnetic field for higher magnitude of reflector gate voltage. In fact, this is the trend for the devices of Fig. 7.5 and Fig. 7.6. It may also be the case for the device of Fig. 7.4, though concluding this is difficult due to the decreased amplitude of the conductance oscillations at higher values of $|V_g|$.

Several features are also striking in the secondary peak structure observed. Many of the secondary peaks also appear with a period of $\lambda_f/2$. For example, a close examination of the data of Fig. 7.4 reveals several prominent secondary peaks in the vicinity of a magnetic field value of 50 mT which are also periodic in V_g with a period of $\lambda_f/2$. This is additional evidence that all conductance peaks can be interpreted as due to simple interference of electron trajectories at the point contact. Also, many of the secondary peak amplitudes first increase as the magnetic field is raised, before fading out again at higher magnetic field values. This may enable the identification of these peaks as corresponding to electron trajectories which are at first oriented towards the outer edges of the reflector gate but are re-oriented towards the center of the reflector as the field is raised.

Fig. 7.9 illustrates a different type of measurement on the resonator. In this case, the x-axis is the voltage on the quantum point contact gate V_{qpc} rather than the magnetic field. The y-axis is again V_g, and the z-axis the differential conductance through the point contact. At high values of $|V_{qpc}|$, the point contact is completely pinched off and no conductance signal is measured. As the V_{qpc} is opened further, conductance resonances are observed as before. As the point contact is opened still further, additional structure in the conductance signal appears. All of the conductance peak positions slope upward as the point contact is opened. This is because the point contact gate forms one wall of the resonator, and the boundary of this wall also moves as V_{qpc} is varied, again changing the

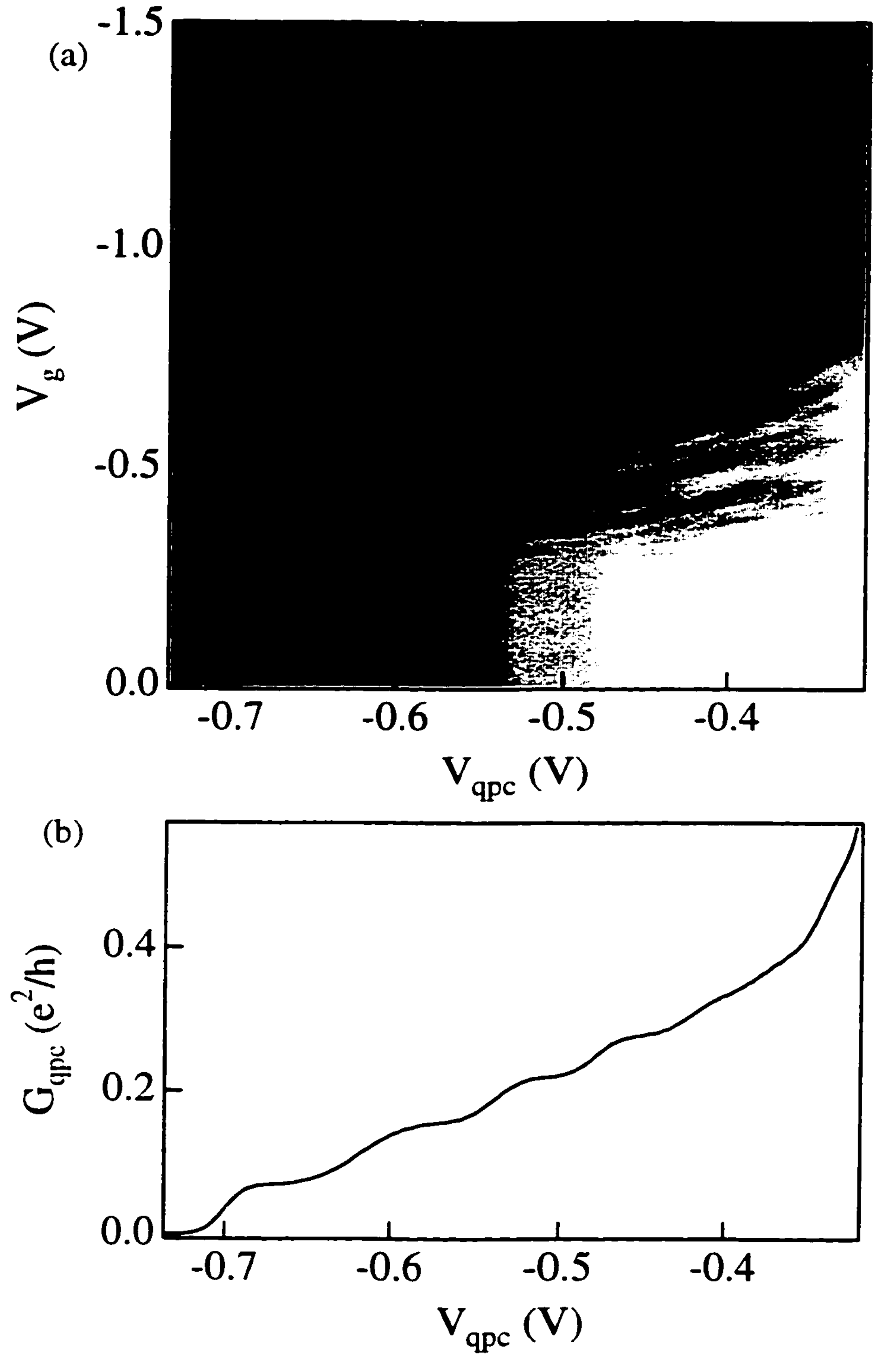

Figure 7.9 (a) Measured differential conductance through the resonator vs. reflector gate voltage V_g and point contact voltage V_{qpc}. For V_{qpc} biased such that the point contact conductance is in the weak tunneling regime, primary conductance peaks are observed as V_g is ramped. As the point contact is opened, additional structure appears. (b) Corresponding point contact conductance vs. V_{qpc}.

path lengths of closed electron trajectories.

7.4 Conclusion

In this chapter, I have described experiments which dramatically illustrate quantum interference of electron waves, an aspect of mesoscopic electron transport different from the emphasis of the experiments on quantum dots described in previous chapters. I have described measurements on electron resonators which show conductance peaks resulting from interference of backscattered electron waves, and the dependence of these peaks on magnetic field and point contact conductance has been studied. The magnetic field dependence is explained by phase shifts caused by trajectory bending and the Aharonov-Bohm contribution. The latter is shown to be essential to explain the observed data, and thus these measurements constitute a direct observation of the Aharanov-Bohm phase shift in an open structure.

Chapter 8

Conclusions and Future Directions

The preceding chapters have described a number of experiments which investigated various aspects of mesoscopic electron transport in quantum dot structures as well as interference phenomena in an electron resonator. The experiments in chapter IV demonstrated the breakdown of charge quantization in a single electron box due to quantum tunneling by directly measuring the charge in the box with a capacitively coupled SET electrometer. This work was the first such measurement to study charge quantization in a single electron box over the full range of box-to-lead conductance G values ranging from $G \sim 0$ to $G = G_Q$, the conductance quantum. The principal result was that charge quantization is completely destroyed at $G = G_Q$, in agreement with theory. This work also demonstrated that electrometer measurements are a more sensitive means of probing charge quantization in a quantum dot than transport measurements. Even more sensitive measurements could be made in the future by constructing an electrometer which is more strongly coupled to the quantum dot. Eventually increasing this coupling would result in a feedback effect which could be exploited to make a current switch, an experiment which is currently underway in the Westervelt group.

The effects of the electron spin in the energy spectra of quantum dots were also investigated in the work described in this thesis. In particular, the addition spectrum of a small quantum dot was studied as a function of a magnetic field applied parallel to the plane of the 2DEG. The addition spectrum was observed to evolve with field in a manner consistent with a Zeeman contribution to the dot ground state energy. However, orbital effects also clearly played a role in this evolution, and it is difficult in some cases to distinguish between orbital and spin effects. This suggests several possibilities for future experiments to resolve this ambiguity. Observing the evolution of Coulomb blockade peak positions with several different orientations of the parallel magnetic field could aid in distinguishing the effects of spin from orbital effects. A rotating sample stage could ensure that no perpendicular component of the magnetic field was influencing the evolution of the ground state spectrum. Because of a possible relationship between the size of quantum dots and manifestations of spin, it would be interesting to make similar measurements on dots of several different sizes.

Chapter VI presented measurements on a system of two coupled quantum dots, the artifical molecule. The coupling between the two dots could be controlled by changing the conductance of the interdot quantum point contact. The corresponding interdot interactions could be studied via measurements of the peak splitting in two-dimensional double dot conductance landscapes. The dependence of the double dot ground state energy on magnetic field was studied by measuring the evolution of the peak splitting with field for a range of values of interdot conductance. The conductance peak splitting and peak heights were observed to fluctuate with magnetic field due to shifts in dot level spectra and corresponding fluctuations in the interdot interactions. This type of behavior is relevant to any future applications which involve multiple quantum dot structures. Future experiments which build on this work could include statistical studies of double dot systems in order to quantify more precisely the effects of mesoscopic fluctuations in coupled quantum dot systems.

Finally, chapter VII presented magnetoconductance measurements of an open electron resonator. Peaks in the conductance of the device were observed as the size of the resonator cavity was varied. These peaks are due to the constructive interference of backscattered electron waves. A peak occurs each time the path length of the backscattered trajectory changes by a Fermi wavelength. The positions of the conductance peaks as a function of cavity size were observed to curve with magnetic field in a manner that can be explained by a combination of electron trajectory bending by the magnetic field and an Aharonov-Bohm contribution. This measurement constitutes an unusual observation of the Aharonov-Bohm phase shift in an open mesoscopic structure.

References

Adourian, A.S., C. Livermore, R.M. Westervelt, K.L. Campman, and A.C. Gossard (1996a). *Superlattices and Microstructures* **20**, 411.

Adourian, A.S. (1996b). "Single Electron Transport in Parallel Coupled Quantum Dot Nanostructures," Ph.D. Thesis, Harvard University.

Adourian, A.S., C. Livermore, R.M. Westervelt, K.L. Campman, and A.C. Gossard (1999). *Appl. Phys. Lett.* **75**, 424.

Averin, D.V. and K.K. Likharev (1990). *Quantum Effects in Small Disordered Systems*, eds. B. Altshuler, P.A. Lee, and R.A. Webb (Elsevier, Amsterdam).

Baranger, H.U., D. Ullmo, L. I. Glazman (1999). Cond-mat/9907151.

Baskey, J.H. (1994). "Transport and Capacitance Measurements of Electron Multilayers in Wide Parabolic Quantum Wells," Ph.D. Thesis, Harvard University.

Beenakker, C.W.J. (1991). *Phys. Rev. B* **44**, 1646.

Beenakker, C.W.J. (1997). *Rev. Mod. Phys.* **69**, 731.

Beenakker, C.W.J. and H. van Houten (1991). "Quantum transport in semiconductor nanostructures," in Solid State Physics **44**, H. Ehrenreich and D. Turnbull, eds., Academic press, San Diego.

Berman, D., N. B. Zhitenev, R. C. Ashoori, H. I. Smith, and M. R. Melloch (1997). *J. Vac. Sci. Tech. B* **15**, 2844.

Berman, D., N.B. Zhitenve, R.C. Ashoori, and M. Shayegan (1999). *Phys. Rev. Lett.* **82**, 161.

Berry, M.J., J.A. Katine, R.M. Westervelt, and A.C. Gossard (1994a). *Phys. Rev. B* **50**, 17721.

Berry, M.J., J.H. Baskey, R.M. Westervelt, and A.C. Gossard (1994b). *Phys. Rev. B* **50**, 8857.

Black, C.T., D.C. Ralph, and M. Tinkham (1996). *Phys. Rev. Lett.* **76**, 688.

Blick, R.H., R.J. Haug, K. Von Klitzing, and K. Eberl (1995). *Appl. Phys. Lett.* **67**, 3924.

Blick, R.H., R.J. Haug, J. Weis, D. Pfannkuche, K.V. von Klitzing, and K. Eberl (1996). *Phys. Rev. B* **53**, 7899

Blick, R.H., D.W. van der Weide, R.J. Haug, and K. Eberl (1998). *Phys. Rev. Lett.* **81**, 689.

Braslau, N. (1981). *J. Vac. Sci. Tech.* **19**, 803.

Brodsky, M., N.B. Zhitenev, R.C. Ashoori, L.N. Pfeiffer, and K.W. West (2000). *Cond-mat/0001455.*

Brouwer, P.W., Y. Oreg, and B. I. Halperin (1999). Cond-mat/9907148.

Bukard, G., D. Loss, and D. P. DiVincenzo (1999). *Phys. Rev. B* **59**, 2070.

Buttiker, M. (1986). *Phys. Rev. Lett.* **57**, 1761.

Buttiker, M. (1988). *IBM J. Res. Dev.* **32**, 63.

Chan, I.H., R.M. Clarke, C.M. Marcus, K. Campman, and A.C. Gossard (1995). *Phys. Rev. Lett.* **74**, 3876.

Chang, A.M., H.U. Baranger, L.H. Pfeiffer, K.W. West, and T.Y. Chang (1996). *Phys. Rev. Lett.* **76**, 1695.

Cleland, A. N., J. M. Schmidt, and J. Clarke (1992). "Influence of the environment on the Coulomb blockade in submicrometer normal-metal tunnel junctions," *Phys. Rev. B* **45**, 2950.

Cobden, D.H., Bockrath, M., P.L. McEuen, A.G. Rinzler, and R.E. Smalley (1998). *Phys. Rev. Lett.* **81**, 681.

Cronenwett, S.M., S.R. Patel, C.M. Marcus, K. Campman, and A.C. Gossard (1997). *Phys. Rev. Lett.* **79**, 2312.

Cronenwett, S.M., S.M. Maurer, S.R. Patel, C.M. Marcus, C.I. Duruoz, and J.S. Harris (1998). *Phys. Rev. Lett.* **81**, 5904.

Crouch, C.H. (1996). "Single Electron Transport and Charge Quantization in Coupled Quantum Dots," Ph.D. Thesis, Harvard University.

Crouch, C. H., C. Livermore, R. M. Westervelt, K. L. Campman, and A. C. Gossard (1997). *Appl. Phys. Lett.* **71**, 817.

Davidovic, D. and M. Tinkham (1998). *Appl. Phys. Lett.* **73**, 3959.

Davidovic, D. and M. Tinkham (1999). *Phys. Rev. Lett.* **83**, 1644.

Dekker, C., A.J. Scholten, F. Liefrink, R. Eppenga, H. van Houten, and C.T. Foxon (1991). *Phys. Rev. Lett.* **66**, 2148.

Devoret, M. H., D. Esteve, and C. Urbina (1992). *Nature* **360**, 547.

Dingle, R., H.L. Stormer, A.C. Gossard, and W. Wiegman (1978). *Appl. Phys. Lett.* **7**, 665.

DiVincenzo, D.P. and D. Loss (1999). *J. of Magnetism and Magnetic Materials* **200**, 202.

Dixon, D., L.P. Kouwenhoven, P.L. McEuen, Y. Nagamune, J. Motohisa, and H. Sakaki (1996a). *Surface Science* **361-362**, 636.

Dixon, D., L.P. Kouwenhoven, P.L. McEuen, Y. Nagamune, J. Motohisa, and H. Sakaki (1996b). *Phys. Rev. B* **53**, 12625.

Dixon, D. (1998). "Dots, Diodes, and DNP: Electronic and Nuclear Interactions in Two-Dimensional Electron Gases," Ph.D. Thesis, University of California, Berkeley.

Dresselhaus, L., L. Ji, S. Han, J. E. Lukens, , and K. K. Likharev (1994). *Phys. Rev. Lett.* **72**, 3226.

Edwards, J.D., M.R. Haggerty, and E.J. Heller (1998). "Diffractive Resonances in Open Mesoscopic Cavities," unpublished.

Falci, G., J. Heins, G. Schon, and G. T. Zimanyi (1994). *Physica B*, **203**, 409.

Folk, J.A., S.R. Patel, S.F. Godijn, A.G. Huibers, S.M. Cronenwett, C.M. Marcus, K. Campman, and A.C. Gossard (1996). *Phys. Rev. Lett.* **76**, 1699.

Furusaki, A., K. A. Matveev (1995). *Phys. Rev. Lett.* **75**, 709.

Geerligs, L. J., V. F. Anderegg, P. A. M. Holweg, and J. E. Mooij (1990). *Phys. Rev. Lett.* **64**, 2691.

Glazman, L.I. and R. I. Shekhter (1989). *J. Phys.: Condens. Matter* **1**, 5811.

Glazman, L.I., K. A. Matveev (1991). *Sov. Phys. JETP* **71**, 1031.

Golden, J.M. and B.I. Halperin (1996a). *Phys. Rev. B* **54**, 16757.

Golden, J.M. and B.I. Halperin (1996b). *Phys. Rev. B* **53**, 3893.

Golden, J.M. and B.I. Halperin (1997). *Phys. Rev. B* **56**, 4716.

Goldhaber-Gordon, D. (1999). "The Kondo Effect in a Single-Electron Transistor," Ph.D. Thesis, MIT.

Gossard, A.C. (1982). "Molecular beam epitaxy of superlattices in thin films" in *Treatise on Materials Science and Technology* **24**, eds. K.N. Tu and R. Rosenberg (Academic Press, New York) 13.

Grabert, H. and M.H. Devoret, eds. (1992). *Single Charge Tunneling*, NATO ASI Series B **294**, Plenum, New York.

Grabert, H. (1994). *Phys. Rev. B* **50**, 17364.

Herman, M.A. and H. Sitter (1989). *Molecular Beam Epitaxy: Fundamentals and Current Status*, Springer-Verlag, Berlin.

Hofstetter, W., and W. Zwerger (1997). *Phys. Rev. Lett.* **78**, 3737.

Hopkins, P.F. (1990). "Electron Transport in Wide Parabolic GaAs/AlGaAs Wells," Ph.D. Thesis, Harvard University.

Horowitz, P. and W. Hill (1989). *The Art of Electronics, 2nd Edition*, Cambridge Univ. Press, Cambridge, England.

Hu, G. Y., R. F. O'Connell, and J. Y. Ryu (1994). *Physica B* **194**, 1021.

Hu, G. Y., and R. F. O'Connell (1995). *Physica A* **219**, 88.

Huibers, A. (1998). Ph.D. Thesis, Stanford University.

Huibers, A.G., S.R. Patel, C.M. Marcus, P.W. Brouwer, C.I. Duruoz, and J.S. Harris 1998). *Phys. Rev. Lett.* **81**, 1917.

Imamoglu, A., D.D. Awschalom, G. Burkard, D.P. DiVincenzo, D. Loss, M. Sherwin, and A. Small (1999). *Phys. Rev. Lett.* **83**, 4204.

Jacquod, P. and A. D. Stone (1999). Cond-mat/9909067.

Kaminski, A., and L.I. Glazman (1999). *Phys. Rev. B* **59**, 9798.

Kastner, M.A. (1992). "The single-electron transistor," *Rev. Mod. Phys.* **64**, 849.

Kastner, M.A. (1993). *Physics Today* **46**, 24.

Katine, J.A. (1996). "Electron Quantum Interference in Ballistic Semiconductor Nanostructures," Ph.D. thesis, Harvard University.

Katine, J.A., J.A. Eriksson, A.S. Adourian, R.M. Westervelt, J.D. Edwards, A. Lupu-Sax, E.J. Heller, K.L. Campman, and A.C. Gossard (1997). *Phys. Rev. Lett.* **79**, 4806.

Klimeck, G., G. Chen, and S. Datta (1994). *Phys. Rev. B* **50**, 2316.

Kouwenhoven, L. P., N. C. van der Vaart, A. T. Johnson, W. Kool, C. J. P. M. Harmans, J. G. Williamson, A. A. M. Starling, and C. T. Foxon (1991a). *Zeit Phys. B* **85**, 367.

Kouwenhoven, L. P., A. T. Johnson, N. C. van der Vaart, A. van der Enden, C. J. P. M. Harmans, and C. T. Foxon (1991b). *Zeit. Phys. B* **85**, 381.

Kulik, I.O. and R.I. Shekhter (1975). *Zh. Eksp. Teor. Fiz.* **68**, 623.

Lafarge, P., H. Pothier, E. R. Williams, D. Esteve, C. Urbina, and M. H. Devoret (1991). *Zeit. Phys. B*85, 327.

Landauer, R. (1957). *IBM J. Res. Dev.* **1**, 223.

Likharev, K.K. and D.V. Averin (1992). "Possible Applications of the Single Charge Tunneling" in *Single Charge Tunneling*, NATO ASI Series B **294**, H. Grabert and M.H. Devoret, eds., Plenum, New York.

Livermore, C., C. H. Crouch, R. M. Westervelt, K. L. Campman, and A. C. Gossard (1996). *Science* **274**, 1332.

Livermore, C.L. (1998). "Coulomb Blockade Spectroscopy in Tunnel-Coupled Quantum Dots," Ph.D. Thesis, Harvard University.

Livermore, C., D.S. Duncan, R.M. Westervelt, K.D. Maranowski, and A.C. Gossard (1999a). *J. of Appl. Phys.* **86**, 4043.

Livermore, C., D.S. Duncan, R.M. Westervelt, K.D. Maranowski, and A.C. Gossard (1999b). *Phys. Rev. B* **59**, 10744.

Loss, D. and D.P. DiVincenzo (1998). *Phys. Rev. A* **57**, 120.

Loss, D. and D.P. DiVincenzo (1999). *Phys. Rev. A* **57**, 120.

Loss, D. and E.V. Sukhorukov (2000). *Phys. Rev. Lett.* **84**, 1035.

Lounasmaa, O.V. (1974). *Experimental Principles and Methods Below 1 K*, Academic Press, New York.

Lukens, J. E., P. D. Dresselhaus, S. Han, L. Ji, K. K. Likharev, and W. Zheng (1994). *Physica B* **203**, 354.

Mar, D.J. (1994). "Cryogenic Field-Effect Transistors for the Study of Semiconductor Nanostructures," Ph.D. Thesis, Harvard University.

Marcus, C.M., A.J. Rimberg, R.M. Westervelt, P.F. Hopkins, and A.C. Gossard (1992). *Phys. Rev. Lett.* **69**, 506.

Martinis, J. M. and M. Nahum (1993). *Phys. Rev. B* **48**, 18316.

Martinis, J. M. and M. Nahum (1994). *Phys. Rev. Lett.* **72**, 904.

Martinis, J., M. Devoret, and J. Clarke (1987). *Phys. Rev. B* **35**, 4682.

Matveev, K. A. (1991). *Sov. Phys. JETP* **72**, 892.

Matveev, K. A. (1995). *Phys. Rev. B* **51**, 1743.

Matveev, K.A., L.I. Glazman, and H.U. Baranger (1996a). *Phys. Rev. B* **54**, 5637.

Matveev, K.A., L.I. Glazman, and H.U. Baranger (1996b). *Surface Science* **361**, 623.

Maurer, S.M., S.R. Patel, C.M. Marcus, C.I. Duruoz, and J.S. Harris (1999). *Phys. Rev. Lett.*, **83**, 1403.

Meir, Y., N.S. Wingreen, and P.A. Lee (1991). *Phys. Rev. Lett.* **66**, 3048.

Molenkamp, L. W., K. Flensberg, and M. Kemerink (1995). *Phys. Rev. Lett.* **75**, 4282.

Oosterkamp, T.H., T. Fujisawa, W.G. Van Der Wiel, K. Ishibashi, R.V. Hijman, S. Tarucha, and L.P. Kouwenhoven (1998a). *Nature* **395**, 873.

Oosterkamp, T.H., S.F. Godijn, M.J. Vilenreef, Y.V. Nazarov, N.C. van der Vaart, and L.P. Kouwenhoven (1998b). *Phys. Rev. Lett.* **80**, 4951.

Patel, S.R., S.M. Cronenwett, A.G. Huibers, M. Switkes, J.A. Folk, c.M. Marcus, K. Campman, and A.C. Gossard (1997). *Superlattices and Microstructures* **21**, 43.

Patel, S.R., S.M. Cronenwett, D.R. Stewart, A.G. Huibers, C.M. Marcus, C.I. Duruoz, J.S. Harris, K. Campman, and A.C. Gossard (1998). *Phys. Rev. Lett.* **80**, 4522.

Pohlen, S.L. (1999). "The Superconducting Single Electron Transistor," Ph.D. Thesis, Harvard University.

Ralph, D.C., C. T. Black, and M. Tinkham (1995). *Phys. Rev. Lett.* **74**, 3241.

Ralph, D.C., C. T. Black, and M. Tinkham (1997). *Phys. Rev. Lett.* **78**, 4087.

Rimberg, A.J. (1992). "Magnetotransport in Uniform and Modulated Electron Gases in Wide Parabolic Quantum Wells," Ph.D. Thesis, Harvard University.

Ruzin, I.M., V. Chandrasekhar, E.I. Levin, and L.I. Glazman (1992). *Phys. Rev. B* **45**, 13469.

Sivan, U., R. Berkovits, Y. Aloni, O. Prus, A. Auerbach, and G. Ben-Yoseph (1996). *Phys. Rev. Lett.* **77**, 1123.

Sohn, L.L., L.P. Kouwenhoven, and Gerd Schon, eds. (1996). *Mesoscopic Electron Transport*, NATO ASI Series E **345**, Kluwer, Dordrecht.

Spector, J., H.L. Stormer, K.W. Baldwin, L.N. Pfeiffer, and K.W. West (1992). *Surface Science* **263**, 240.

Spector, J., H.L. Stormer, K.W. Baldwin, L.N. Pfeiffer, and K.W. West (1990a). *Appl. Phys. Lett.* **56**, 967.

Spector, J., H.L. Stormer, K.W. Baldwin, L.N. Pfeiffer, and K.W. West (1990b). *Appl. Phys. Lett.* **56**, 2433.

Spector, J., H.L. Stormer, K.W. Baldwin, L.N. Pfeiffer, and K.W. West (1990c). *Appl. Phys. Lett.* **56**, 1290.

Stafford, C.A.and S. Das Sarma (1994). *Phys. Rev. Lett.* **72**, 3590.

Stern, F. (1968). *Phys. Rev. Lett.* **21**, 1687.

Stewart, D., D. Sprinzak, C.M. Marcus, C.I. Duruoz, and J.S. Harris (1997). *Science* **278**, 1784.

Stewart, Duncan (1999). "Level Spectroscopy of a Quantum Dot," Ph.D. thesis, Stanford University.

Stormer, H.L., R. Dingle, A.C. Gossard, and W. Wiegman (1978). "Proc. 14th ICPS," ed. B.L.H. Wilson (Institute of Physics, London), 6.

Tans, S.J., M.H. Devoret, R.J.A. Groeneveld, and C. Dekker (1998). *Nature* **394**, 761.

Tarucha, S., D.G. Austing, T. Honda, R.J. van der Hage, and L.P. Kouwenhoven (1996). *Phys. Rev. Lett.* **77**, 3613.

Taylor, R.P., P.T. Coleridge, Y. Feng, M. Davies, J. McCaffrey, and P.A. Marshall (1994). *J. of Appl. Phys.* **76**, 7966.

Thornton, T.J., M. Pepper, H. Ahmed, D. Andrews, and G.J. Davies (1986). *Phys. Rev. Lett.* **56**, 1198.

Timp, G., R.E. Behringer, and J.E. Cunningham (1990). *Phys. Rev. B* **42**, 9259.

Tinkham, M. (1996). *Introduction to Superconductivity*, 2nd ed., McGraw-Hill, New York.

Tsui, D.C., H.L. Stormer, and A.C. Gossard (1982). *Phys. Rev. Lett.* **48**, 1559.

Van der Vaart, N.C. (1995a). "Single Electron Transport and Quantum Confinement in Semiconductor Nanostructures," Ph.D. Thesis, Delft Technical University.

Van der Vaart, N.C., S.F. Godijn, Y.V. Nazarov, C.J.P.M. Harmans, J.E. Mooij, L.W. Molenkamp, and C.T. Foxon (1995b). *Phys. Rev. Lett.* **74**, 4702.

Van Houten, H. and C.W.J. Beenakker (1989). *Phys. Rev. Lett.* **63**, 1893

Van Wees, B.J., H. van Houten, C.W.J. Beenakker, J.G. Williamson, L.P. Kouwenhoven, D. van der Marel, and C.T. Foxon (1988). *Phys. Rev. Lett.* **60**, 848.

Vion, D., P. F. Orfila, P. Joyez, D. Esteve, and M. H. Devoret (1995). "Miniature electrical filters for single electron devices," *J. Appl. Phys.*, **77**, 2519.

Von Klitzing, K., G. Dorda, and M. Pepper (1980). *Phys. Rev. Lett.* **45**, 494.

Wang, X. (1997). *Phys. Rev. B* **55**, 4073.

Waugh, F.R. (1994). "Novel architectures and devices for computing," Ph.D. thesis, Harvard University.

Waugh, F.R., M.J. Berry, D.J. Mar, R.M. Westervelt, K.L. Campman, and A.C. Gossard (1995). *Phys. Rev. Lett.* **75**, 705.

Waugh, F.R., M.J. Berry, C.H. Crouch, C. Livermore, D.J. Mar, R.M.Westervelt, K.L. Campman, and A.C. Gossard (1996). *Phys. Rev. B* **53**, 1413.

Weis, J., R. J. Haug, K. v. Klitzing, and K. Ploog (1993). *Phys. Rev. Lett.* **71**, 4019.

Weis, J., R. J. Haug, K. v. Klitzing, and K. Ploog (1994). *Surface Science* **305**, 664.

Wharam, D.A., T.J. Thornton, R. Newbury, M. Pepper, H.Ahmed, J.E.F. Frost, D.G. Hasko, D.C. Peakcock, D.A. Ritchie, and G.A.C. Jones (1988). *J. Phys. C* **21**, L209.

Zheng, H.Z., H.P. Wei, D.C. Tsui, and G. Weimann (1986). *Phys. Rev. B* **34**, 5635.

Zhitenev, N.B., M. Brodsky, R.C. Ashoori, L.N. Pfeiffer, and K.W. West (1999). *Science* **285**, 715.

Zorin, A. B. (1995). "The thermocoax cable as the microwave frequency filter for single electron circuits," *Rev. Sci. Instrum.* **66**, 4296.

Zwerger, W. (1994). *Zeit. Phys. B* **93**, 333.